Detection of Thermal Magnon via Nitrogen-Vacancy Centers in Diamond
(ダイヤモンド中のNV中心を用いた熱マグノンの計測)

Dwi Prananto

Japan Advanced Institute of Science and Technology

Doctoral Dissertation

Detection of Thermal Magnon via Nitrogen-Vacancy Centers in Diamond
(ダイヤモンド中のNV中心を用いた熱マグノンの計測)

Dwi Prananto

Supervisor:
Assoc. Prof. Toshu An

Graduate School of Advanced Science and Technology
Japan Advanced Institute of Science and Technology
Materials Science
June 2019

Abstract

Current of thermally induced magnon has recently been considered as a medium for transporting information with low energy dissipation. It has been demonstrated that thermal magnon can transmit information as far as 40 μm at room temperature and more than 100 μm at 23 K. In the past few years research has been focused on understanding the nature of thermal magnon transport and how it interacts with environment. Several researches have demonstrated that thermal magnon can transfer its angular momentum to other spin system, a phenomenon known as thermal spin transfer torque.

Recently, electron spins ($S = 1$) associated to nitrogen-vacancy (NV) defect center in diamond have attracted a great attention from spintronics research community due to its ability to sense the dynamics of spin system with exceptional sensitivity. NV center in diamond is well known to have excellent characteristics compared to other spin-based sensor, among them are ambient temperature working condition, long coherence time, and wide band (DC to GHz) magnetometry capability. It has been demonstrated recently that electron spins associated to diamond with NV center can be well coupled with magnetostatic spin waves due to the closeness of their energy, which is within several GHz regime. Detection of thermal magnon with the same technique possesses additional challenge as its energy, defined by k_BT, is far above the NV spin energy.

In this dissertation we explore an unprecedented technique in the detection of thermal magnon using electron spins in diamond with NV centers as quantum sensors. We employ a diamond beam ($2.5 \times 0.1 \times 0.1$ mm^3) with (110) crystal orientation hosting a layer of NV spin ensemble at the depth of about 30 nm beneath the surface of the diamond. As a material for the investigation of thermal magnon we use yttrium iron garnet (YIG) ($Y_5Fe_{12}O_3$) which is well known as an ideal test bed for studying magnon transport due to its electrically-insulating characteristic. Thermal magnon is generated by introducing non-equilibrium temperature condition in YIG. We make use of magnetostatic surface spin wave (MSSW), generated in YIG by a coherent microwave source, as a mediator for the detection of the thermal magnon.

A home-build scanning confocal microscope, equipped with a high-speed multichannel pulse generator, is employed to optically manipulate and detect the states of NV spins under the influence of thermal magnon and MSSW. We found that the dynamics of MSSW is modulated under the alteration of temperature gradient in YIG. This modulation is observed as a change in the contrast of the optically detected magnetic resonance (ODMR) spectrum of the NV spins as temperature gradient is applied to the YIG. Moreover, we found that the strength of oscillating magnetic field generated by the MSSW which drives the NV spins to their two-level transition ($m_s = 0 \leftrightarrow 1$), or Rabi oscillation, is enhanced or diminished with the variation of temperature gradient applied to the YIG. We interpret this as a generation of thermal magnon current that induces an additional magnetic damping torque that modify the magnetization dynamics of MSSW. We estimated the magnetic damping torque parameter from the thermal magnon to be $\sim 10^{-4}$, in a good agreement with the known value of damping parameter of YIG. We confirm our investigation with the conventional electrical spin wave resonance technique through the observation of spin wave resonance linewidth and found a modulation of resonance linewidth as a function of temperature gradient.

The technique discussed in this dissertation is expected to open new possibilities towards a better understanding of thermal magnon transport and its interplay with magnetostatic spin wave. Moreover, the technique can be extended to study thermal magnon transport locally at smaller scale in nanometer regime by employing NV center hosted in a nanometer-sized diamond.

Keywords: thermal magnon, nitrogen-vacancy (NV) center in diamond, magnetometry, magnetostatic surface spin wave, thermal spin transfer torque.

Acknowledgment

All praise goes to the Almighty God, *Allah*, because of His ceaseless compassion I have been able to complete this dissertation. I would like to dedicate this page to express my gratitude to the people around me for their countless support. First of all, I would like to give my sincere thanks to Prof. Toshu An for giving me a valuable opportunity to conduct research in his laboratory and exposing me to invaluable research and educational experiences through research collaborations and opportunities to attend and give a talk at conferences domestically and abroad. I am very indebted for his constant support and guidance in my research and education so that I am able to get a good experimental results and complete this dissertation. I also very grateful for his support beyond academic life that made my life at JAIST more exciting. I am very thankful to Prof. Hiroshi Mizuta, Prof. Mikio Koyano, Prof. Masashi Akabori, and Prof. Eisuke Abe (RIKEN) for their valuable evaluation and suggestion to this dissertation. I am very grateful for the support from Prof. Tatsuya Shimoda, before his retirement, and Prof. Yukiko Takamura as a second supervisor. During my study I have been very fortunate to have a valuable experience to stay for three months at the Meriles Group at the City College of New York; I am very thankful to Prof. Carlos A. Meriles for the opportunity and guidance, Dr. Pablo Zangara, Dr. Siddharth Dhomkar, and Dr. Jacob Henshaw for sharing their knowledge and skills on NV research. I am thankful to Dr. Abdelghani Laraoui (University of New Mexico) for teaching me how to build a nice confocal microscope that I use for this dissertation. I am also grateful to the opportunity given by Prof. Ken-ichi Uchida and Dr. Ryo Iguchi for using their experimental facilities at NIMS. Life at JAIST would not be the same without the member of An-laboratory: I would like to thank Dr. Daisuke Kikuchi for his support and guidance in research and also fruitful conversations about academia and beyond; Kanbara-san for the many helps as my tutor during my early days at JAIST; Hayashi-san for his indispensable support on control software for experiments; Eimoto-san, Iwata-san, and Moriyama-san for spending delightful time in the lab and outside; Kainuma-san for being a good partner for stimulating discussion on research; Nakashita-san, Ikeda-san, and Wang-san for their supportive time in the lab. I am very grateful for the financial support from JAIST through the Doctoral Research Fellowship (DRF) for my three-year study period, JAIST Research Grant for funding my research, and JAIST Grant for Off-Campus Research for supporting my three-month stay at the City College of New York. I am very grateful for the support from fellow of Indonesian students at JAIST and muslim students at JAIST Muslim Circle (JMC) which I cannot mention one by one. Lastly, I would like to thank for the constant support and prayer from my family, in particular my parents (Rizal Soeryobroto and Agustin Dwi Ratna), my brother Yudhanto Pratama and sister Paramitha Tri Ratna and their family.

Contents

List of Figures

List of Tables

Chapter 1

Introduction

1.1 Background and Motivation

The advancement of information and communication technology in the last five decades goes hand in hand with the scaling and number of transistors that can be packed into a single-chip of microprocessor. As manufacturing technology of transistor gets more advanced and economically feasible, more and more transistors can be integrated into a single-chip year by year and computational power gets boosted by it. The number of transistors in a microprocessor chip was predicted by Gordon Moore to be doubled every two years [1], up until now several billion of transistors can be packed into a hundreds of milimeter-sized microprocessor chip. This scaling power comes without no consequences, as the number of transistors increased the more energy is needed to power the chip and with denser transistors more heat is generated.

Efforts to mitigate the escalation of power consumption include limiting computational speed and redesigning chip circuitry so that it can incorporate more than one processor [2] and excessive heat generation may be mitigated by thermoelectric effect in solid state structure. However, further scaling may reach a point where redesigning chip and waste heat management can no longer overcome due to the quantum limit.

The use of spin angular momentum of electron for representing fundamental quantity of information or bit can be an alternative solution to surpass the limit of electronics technology. Spin electronics, or spintronics, is a field that deals with generation and manipulation of spin degree of freedom in solid state system [3]. Instead of using flow of charged particles as a means of information transport, manipulation, and storage, spintronics devices harnessed the flow of electron spins.

There are two well known approaches in spintronics in terms of what kind of spin current used for processing information. The first approach exploits spin polarized current created by non-equilibrium electron spin population in solids. Second approach utilizes collective excitation of electron spins in magnetically ordered solid, known as spin wave or magnon. The later approach, known as magnon spintronics [5], offers a possibility to fashion a novel form of computation with low energy dissipation due to the ability of spin wave to propagate without the involvement of charge-carrying particle movement [6].

Spin wave can be generated by several ways; along with conventional electrical excitation through induction of AC magnetic field by microwave antenna, temperature gradient can also induce spin wave in magnetic materials [7, 50–53] and will be the focus of this dissertation.

Study of the coupling between spin and heat, known as spin caloritronics [4], has attracted much attention from condensed matter physicists and engineers due to its potential application for the development of 'green' information and communication technology. Coupling between spin and heat allows us to exploit new possibilities and functionalities to convert superfluous heat into a more useful form of energy. Among the interesting functionalities are the possibility to transfer angular momentum from thermally excited magnon to other spin system, a phenomenon known as thermal spin-transfer torque (TST) [9]. This transfer of spin angular momentum can exert torque that leads to a modification of magnetization dynamics.

It was predicted that TST can exert modification of magnetization 60 times more efficient that spin transfer torque obtained by electrically induced spin current [10–12]. This may leads to a more efficient device for processing and storing information. With the demand of nanoscale device miniaturization and power optimization in device operation, study of spin dynamics and its interaction with heat becoming more relevant nowadays. Better understanding on the interplay between spin and heat will leads to the progress of more efficient information and communication technology. For this purpose a measurement system that capable of probing dynamics of magnetization with high sensitivity and resolution is highly demanding.

The use of quantum sensor [13], a sensor that work based on the utilization of quantum objects, for probing transport properties in condensed matter system has become emergent recently [14]. Nitrogen-vacancy (NV) center in diamond is well known as a quantum sensor that has excellent characteristic such as ambient temperature working condition, long coherence time, and multiple sensing capabilities including magnetic field (DC to GHz AC magnetic field) [15–17], temperature [18,19], pressure [20], and electric field sensing [21]. NV center in diamond is a proper sensor for studying condensed matter system that involve interaction between multiple parameters such as spin caloritronics.

This dissertation is aimed at exploring the capability of NV center in diamond as a quantum sensor for probing thermally induced magnon transport in a magnetic insulator material. The research is expected to reveal an unprecedented technique in the detection of thermal magnon with the prospect to broaden knowledge and gain a better insight into the understanding of magnon transport in magnetically ordered solids, in particular on how it interact with heat and other spin system.

1.2 Organization of Dissertation

This dissertation is organized into six chapters covering from fundamental concept to the main results of the dissertation;

Chapter 2 covers the fundamental concept of the nitrogen-vacancy center in diamond. Structural, optical and spin properties of nitrogen-vacancy center

in diamond are elaborated as well as the creation of NV centers in diamond. Techniques in optical spectroscopy with NV centers are introduced; covering the basics of optical and microwave spin manipulation as well as sensing technique in diamond with NV center.

Chapter 3 covers the fundamental concept of magnetization dynamics. Quantum and classical treatment of dynamics of spins in magnetically ordered media will be introduced. Concept of thermally excited spin waves will be given in this chapter.

Chapter 4 is focused on materials preparation and detailed experimental setup and techniques used in the measurement of thermal magnon.

Chapter 5 describes experimental demonstration of thermal magnon current detection with nitrogen-vacancy centers in diamond. Detail on measurement technique and experimental data will be given. Experimental results will be discussed in this chapter.

Chapter 6 summarizes the results described of the previous chapters and prospective for future development.

Chapter 2

Nitrogen-Vacancy Defect Centers in Diamond

The negatively charged nitrogen-vacancy (NV) center in diamond is a defect center in diamond which composed of a carbon vacancy and neighboring substitutional nitrogen atom (Fig. 2.1a). The configuration produces spin triplet ($S = 1$) in its ground state and excited state that can be addressed optically [23]. In the recent years, NV center in diamond has gained major concern among scientific communities due to its exceptional properties compared to other defect centers and color centers. Among the excellent properties are an extremely high photostability (no blinking or photobleaching) [24, 26], room temperature usability, and long coherence time up to several miliseconds even at room temperature [27]. These exceptional characteristics make NV center in diamond a potential candidate for broad range of applications from high sensitivity magnetometry to quantum computer [24, 25].

2.1 Optical and Spin Properties of Nitrogen-Vacancy Defect Center in Diamond

The electronic structure of diamond with NV center consist of spin triplet at the ground state and excited state which are separated by 1.945 eV (Fig. 2.1b). Once excited optically it will exhibit a broadband fluorescence emission with zero phonon line 637 nm (Fig. 2.3). At zero magnetic field, two out of the three spin sub-levels ($m_s = 0$ and $m_s = \pm 1$) of its ground state and excited state spin triplet are splitted by $D_{gs} = 2.87$ GHz and $D_{es} = 1.42$ GHz, respectively (Fig. 2.1b), due to spin-spin interaction [28].

The spin in diamond NV center can be easily polarized, with high degree of polarization of more than 80% [29], to its $m_s = 0$ through optical exitation by 532 nm laser. The spin sub-levels, $m_s = 0$ ($|0\rangle$)and $m_s = \pm 1$ ($|1\rangle$), of diamond NV have a distinct optical characteristic due to its preferential transition path back to their triplet ground state. This spin selective nature makes it possible to read the spin states optically by monitoring the number of fluorescence photons emitted by the corresponding spin states (Fig. 2.2). Such selectivity is originated from the fact that the spin sub-levels, $m_s = 0$ and $m_s = \pm 1$ state

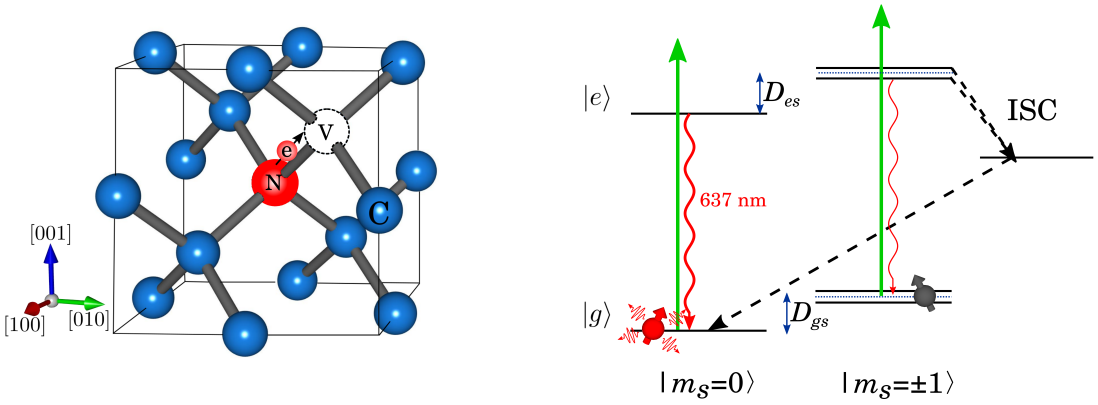

(a) (b)

Figure 2.1: (a) Crystal structure of nitrogen-vacancy center in diamond consist of atomic vacancy (denoted as V) paired with substitutional nitrogen atom (denoted as N) aligning on [111] crystal direction. (b) Energy level of NV center in diamond. Excitation of green laser (532 nm) brings the population at ground state $|g\rangle$ to excited state $|e\rangle$, the excited state $m_s = 0$ will decay back to the ground state $m_s = 0$ and radiate 637 nm light while the $m_s = \pm 1$ will preferentially decay through a non-radiative ISC path (dashed arrow), resulting in contrasting fluorescence. The degeneracy of $m_s = \pm 1$ can be lifted by external magnetic with magnitude defined by $2g_e\mu_B\mathbf{B}$.

undergoes a distinct preferential decay paths when excited from its ground state to excited state; the $m_s = 0$ decay through radiative spin-conserving path back to the ground state $m_s = 0$ while the $m_s = \pm 1$ preferentially undergoes a non-radiative non-conserving decay path through inter-system crossing (ISC) via a singlet state and flip to $m_s = 0$ gound state [29] (Fig.2.1). This distinct decay path results in contrasting number of fluorescence emitted between $m_s = 0$ and $m_s = \pm 1$ by about 30 %.

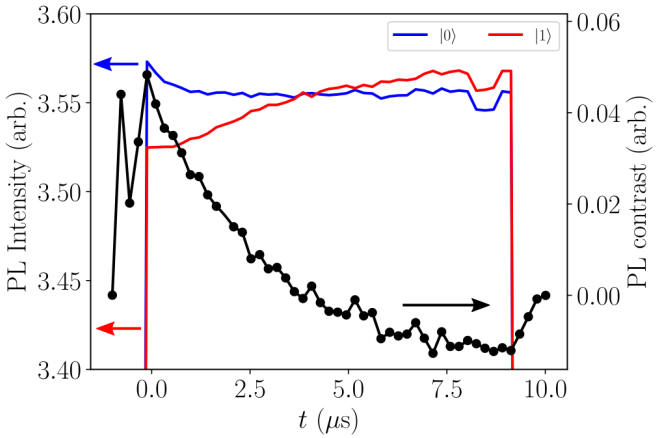

Figure 2.2: Time-resolved photoluminescence (PL) the two state of NV spin states during 10 μs laser illumination. The curves shows distinct PL between $|0\rangle$ and $|1\rangle$ and the contrast between them.

The relation between energy levels of the NV spin state and magnetic field is given by the Hamiltonian

$$H = hDS_z^2 + hE(S_x^2 - S_y^2) + \mathrm{g}_e\mu_B\mathbf{B}\cdot\mathbf{S}, \tag{2.1}$$

with D is on-axis zero-field splitting, E is off-axis zero-field splitting due to internal strain in diamond lattice which can range several hundreds kHz, g_e is Landé g factor, μ_B is Bohr magneton and S_x, S_y, and S_z are Pauli matrices. The ground state on-axis zero field of 2.87 GHz energy that separates the ground state $m_s = 0$ and $m_s = \pm 1$ makes it possible for microwave photon to manipulate the spin state among the three sublevels.

The degeneracy of the $m_s = \pm 1$ can be lifted by applying external magnetic field, thanks to the Zeeman effect. This degeneracy lift results in the shift in resonance frequency of $m_s = +1$ and $m_s = -1$ which splitted to opposite frequency direction (Fig. 2.1b). The resonance frequency shift from 2.87 GHz due to the external magnetic field perturbation contain a set of information about the vector magnetic field and forms the basis for magnetometry and spectroscopy application with spins in diamond NV center. The technique on utilizing optical and microwave excitation to manipulate and read the state of spins in diamond NV center to obtain information about magnetic field is known as the optically detected magnetic resonance (ODMR) [23].

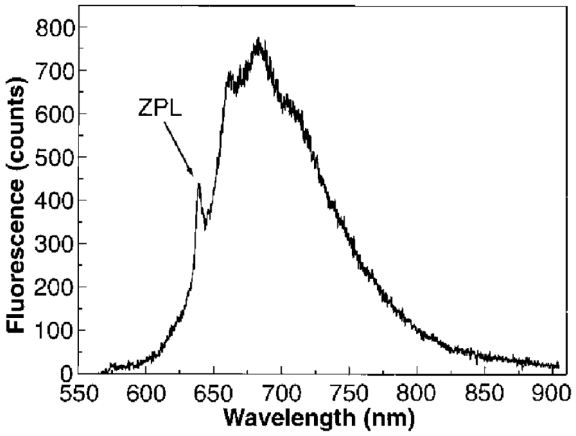

Figure 2.3: Fluorescence spectrum of diamond with nitrogen-vacancy center with sharp zero phonon line (ZPL) at 637 nm. After [23].

2.2 Optical Spectroscopy with Nitrogen-vacancy Center in Diamond

There are already several standard techniques in optical spectroscopy with diamond NV center that commonly used not only for probing strong external DC magnetic field but also very weak quasi-DC or ac magnetic field from electronic or nuclear spins.

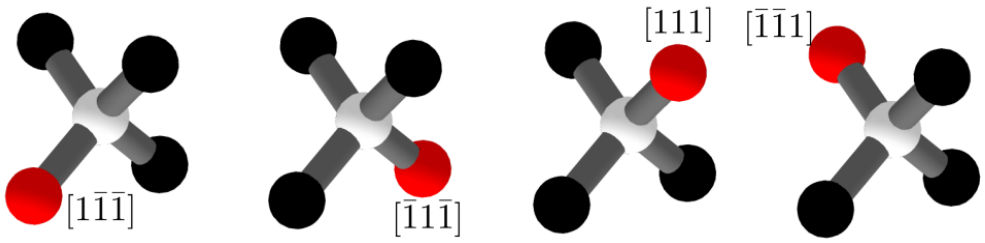

Figure 2.4: Nitrogen (red ball) and vacancy (white ball) pair in diamond crystal can be oriented to four possible direction, [111], [$\bar{1}\bar{1}$1], [1$\bar{1}\bar{1}$], and [$\bar{1}$1$\bar{1}$].

2.2.1 Optically Detected Magnetic Resonance

Among all spectroscopy techniques used in diamond NV center spectroscopy, the optically detected magnetic resonance (ODMR) is the simplest yet fundamental technique. ODMR reveals the resonance frequency of the $m_s = \pm 1$ state of the NV electron spins through the contrasting fluorescence drop as microwave frequency matched the resonance frequency of the $m_s = \pm 1$. ODMR is performed by continuous green laser (532 nm) excitation while sweeping microwave frequency through the resonance frequency of the $m_s = \pm 1$. Fluorescence is monitored during the laser excitation. The resulting spectra are fluorescence counts with Lorentzian dips at the exact resonance transition of the $m_s = \pm 1$ (Fig.2.5).

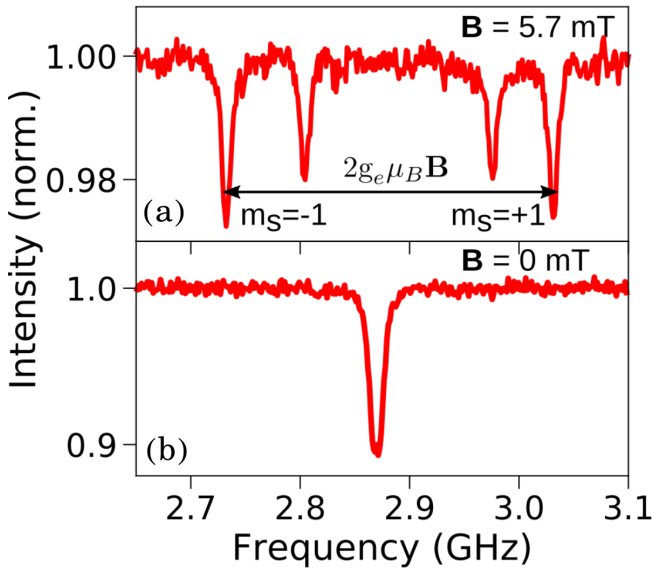

Figure 2.5: Optically detected magnetic resonance spectra is presented as fluorescence intensity as a function of microwave frequency. The Lorentzian drop in fluorescence intensity at specific frequency indicates the resonance frequency of the $m_s = \pm 1$. (b) At zero magnetic field the drop in fluorescence intensity is at 2.87 GHz (the ground state zero field splitting D_{gs}). (a) Under 5.7 mT the $m_s = \pm 1$ are splitted revealing four Lorentzian dips representing NV center that co-linear with magnetic field vector and NV center that make an angle of 109.5° with the magnetic field vector.

When an external magnetic field is applied to the NV spin, the degeneracy of the $m_s = \pm 1$ will be lifted by the Zeeman effect and the resonance transition of each $m_s = +1$ and $m_s = -1$ are revealed as multiple Lorentzian dips at the lower and higher frequencies, respectively, relative to the zero-field splitting $D_{gs} = 2.87$GHz (Fig.2.5). Figure 2.5b shows ODMR spectrum of diamond with ensemble of NV centers under a bias field of 5.7 mT. In diamond with NV centers, pairs of NV can be oriented in one of four possible direction of tetrahedral structure ([111], $[\bar{1}\bar{1}1]$, $[1\bar{1}\bar{1}]$, and $[\bar{1}1\bar{1}]$) that determine NV spin quantization axis (Fig. 2.4). Four dips in ODMR spectrum showed in Fig. 2.5 indicates that the bias field is co-linear to one of the NV axis, two outermost dips correspond to NV that co-linear with the bias field, while two dips in between correspond to three remaining NVs that make angle of 109.5° to the bias field.

Since the amount of splitting depends on the magnitude and direction of external magnetic field, one is able to get information about the vector external magnetic field through the ODMR spectra. This technique is the basis for DC vector magnetometry using NV center in diamond. (See Appendix F for demonstration of DC field magnetometry)

ODMR can also reveal the spectra of nuclear spin if it is performed with low laser power and low microwave power to avoid the broadening of ODMR spectra [30]. For example if the host nitrogen atom of the NV center is ^{14}N with $I = 1$, each of the $m_s = \pm 1$ sublevels will be splitted further into three spectra separated by 2.2 MHz.

2.2.2 Spin Dynamics Representation in a Bloch Sphere

Spin dynamics in NV center system under a resonant microwave manipulation is more easily understood by visualizing it in a so called Bloch sphere in a rotating frame of reference. A rotating frame of reference can be seen as a static coordinate system relative to a frame of reference rotating about $\hat{\boldsymbol{z}}$-axis with frequency ω [35].

The sphere has two poles that represent the two levels of the NV spin states, $|0\rangle$ at the north pole and $|1\rangle$ at the south pole. The spin state is represented by a vector pointing somewhere inside the sphere. $|0\rangle$ state is represented by a vector pointing north and $|1\rangle$ state is represented by a vector pointing south. Any state in between is represented by

$$|\psi\rangle = \cos\left(\frac{\theta}{2}\right)|0\rangle + e^{i\varphi}\sin\left(\frac{\theta}{2}\right)|1\rangle. \tag{2.2}$$

θ represents the angle of rotation, while φ represents the phase. A Resonant microwave field with frequency ω and strength B is represented by a vector field pointing at $\hat{\boldsymbol{x}}$-axis. An NV spin state under this resonant microwave field will undergo a Larmor precession with frequency $\gamma_e B$ about $\hat{\boldsymbol{x}}$-axis [35].

2.2.3 Rabi Oscillation

Under a microwave field at its resonance frequency, NV spin can undergo back and forth transition between $m_s = 0$ to $m_s = \pm 1$ states. If the $m_s = \pm 1$

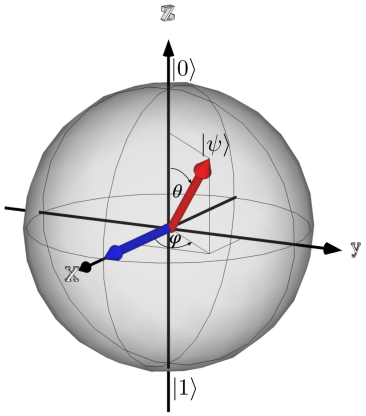

Figure 2.6: Dynamics of spin under an oscillating magnetic field is represented by rotation of vector inside a Bloch sphere sitting in a rotating frame of reference. Oscillating magnetic field in a rotating frame is drawn as a vector pointing on $\hat{\boldsymbol{x}}$-axis (blue arrow). State of spin is represented by a vector (red arrow) rotating about the vector of magnetic field.

are well separated we can consider the $m_s = 0$ and $m_s = -1$ or $m_s = +1$ as a two level system and we can drive oscillation between the two levels through continuous excitation of microwave. This oscillation is well known as Rabi oscillation. Transition probability between two level system under the influence of magnetic field $\mathbf{B} = B_0\hat{\boldsymbol{z}} + B_x \cos\omega t\hat{\boldsymbol{x}}$ is give by

$$P_{|0\rangle\to|1\rangle}(t) = \left(\frac{\omega_x}{\Omega_R}\right)^2 \sin^2\left(\frac{\Omega_R t}{2}\right). \tag{2.3}$$

Ω_R is Rabi oscillation frequency given by

$$\Omega_R = \sqrt{(\omega - \omega_0)^2 + \omega_x^2}, \tag{2.4}$$

with $\omega_0 = \gamma_e B_0$ and $\omega_x = \gamma_e B_x$.

The oscillation between this two level system can be stroboscopically observed by optical means using pulsed laser. In general to observe the spin dynamics of NV center we need three steps of operation; initialization/polarization, manipulation, and read-out (Fig. 2.7a). At the initialization step the NV spin is polarized at its $m_s = 0$ through laser excitation in a specific duration. After the NV spin is polarized at $m_s = 0$, the NV spin can be manipulated by pulsed microwave at the resonance frequency of the $m_s = -1$ or $m_s = +1$. In the end the state of the spin can be read by monitoring the population at $m_s = 0$ by again exciting laser to polarize the remaining population at $m_s = 0$ after microwave manipulation (Fig. 2.7a).

To observe the oscillation between the two levels, the NV spin has to be first initialized to $m_s = 0$ by laser pulse of specific duration to fully populate the state. After initialization, MW is applied to drive the population from the $m_s = 0$ ($|0\rangle$) to $m_s = -1$ ($|1\rangle$). A delay time of about several to hundreds of μs is put in between laser initialization pulse and MW pulse to make sure that $m_s = 0$ state is fully populated before flipping it to $m_s = \pm 1$. This is due to the

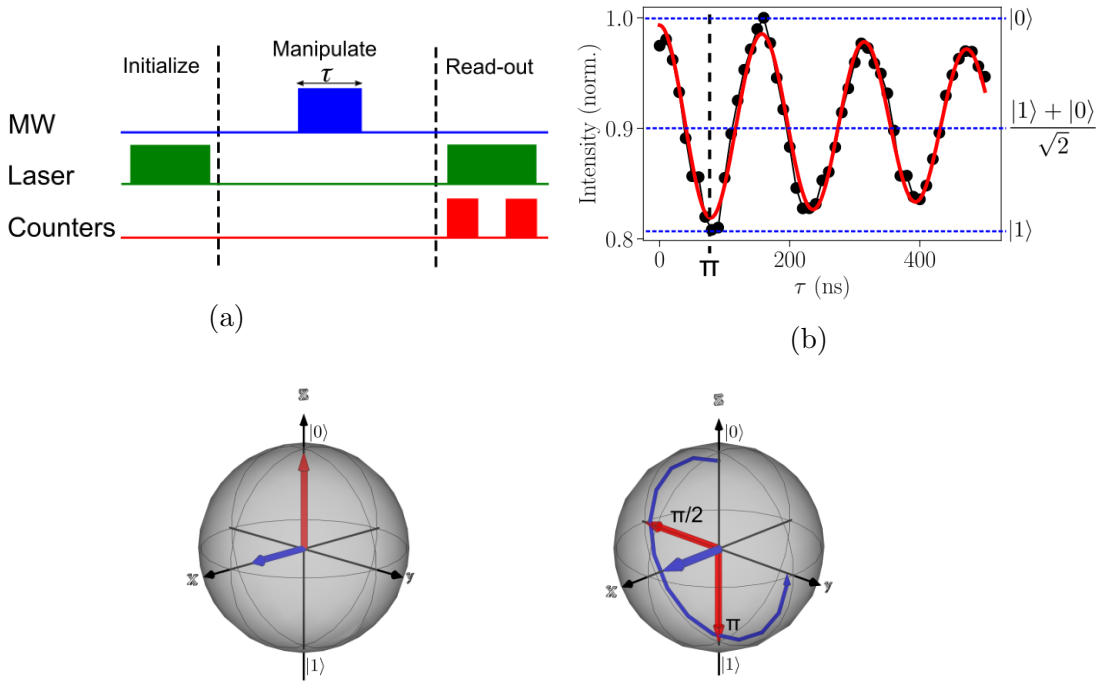

Figure 2.7: (a) Rabi oscillation measurement protocol consist of laser pulse initialization, varied resonant MW duration, and laser pulse read-out. (b) Oscillation of NV spin between two-level system of $|0\rangle$ and $|1\rangle$ with frequency (Rabi frequency) of $\Omega_R/2\pi = 6.353$ MHz. (c) (left) NV spin state in a Bloch sphere under initialization by laser. (right) NV spin revolution about $\hat{\boldsymbol{x}}$-axis, $\pi/2$-pulse rotates NV spin 90° and π-pulse rotates NV spin 180° from its initial state $|0\rangle$.

fact that after laser initialization some population undergoes an inter system crossing and trapped at the singlet state (Fig. 2.1b) which take longer time (about 1 μs) to decay back to the ground state $m_s = 0$ [29,31]. The remaining population at $m_s = 0$ after MW spin manipulation is then read by applying another laser pulse. The population is read by monitoring the fluorescence count integrated over a duration of time. Two counter pulses are generally employed; the first counter pulse, positioned at the very beginning of read-out laser, counts the $m_s = 0$ population right after MW spin manipulation to get the best contrast between $m_s = \pm 1$ and $m_s = 0$ (see Fig. 2.2). While the second counter, positioned at the tail of the read-out laser, counts the population after steady state population of $m_s = 0$ reached.

By varying the MW duration as the sequence repeated, the evolution of population at $m_s = 0$ can be traced, resulting in oscillation known as Rabi oscillation (Fig. 2.7b). Rabi Oscillation can be seen as a rotation of vector in Bloch sphere about the resonant MW field ($\hat{\boldsymbol{x}}$-axis) with frequency defined by Rabi frequency Ω_R. If the microwave is not resonant, detuned by Δ from the resonance frequency, the Rabi frequency will be the resultant of the MW field

and detuning field [32]

$$\Omega_{\text{eff}} = \sqrt{\Omega_R^2 + \Delta^2}. \tag{2.5}$$

Rabi oscillation measurement is a standard protocol to determine the duration needed for a resonant MW to flip the state of spin from $|0\rangle$ to $|1\rangle$, known as π pulse (180° rotation in Bloch sphere). Applying half of π pulse ($\pi/2$), a 90° rotation in Bloch sphere, will bring the spin state to a superposition state of the two state $(|0\rangle + |1\rangle)/\sqrt{2}$. The frequency of Rabi oscillation, which also define the duration of π-pulse, is proportional to square root of microwave power ($\Omega_R \propto \sqrt{I_{MW}}$). Hence, the Rabi frequency can be tuned by adjusting microwave power.

2.2.4 Pulsed Optically Detected Magnetic Resonance

The continuous wave ODMR has some limitation in terms of DC magnetic sensitivity and spectral resolution due to the broadening of spectral linewidth. This power broadening problem can be eliminated by lowering the laser and microwave power with consequences of losing contrast and decreasing number of detected fluorescence [30]. Pulsed-ODMR can eliminate this limitation by flipping the NV spin at dark condition (no laser excitation). The absence of light during microwave spin flip eliminates the spectral broadening due to laser power [30].

Pulsed-ODMR protocol is basically similar to the Rabi oscillation measurement protocol, unless that the microwave duration is fixed at π-pulse. The sequence is repeated while sweeping microwave frequency, resulting in fluorescence drop when the microwave π-pulse is in resonance with the $m_s = \pm 1$. Since there is no light when resonant microwave π-pulse is applied spectral broadening due to laser power is dismissed and the contrast and spectral resolution can be controlled merely by adjusting microwave power (Rabi frequency) (Fig.2.8).

2.2.5 Ramsey Interferometry

Ramsey interferometry use free (not driven by microwave) oscillation of NV spin dynamics to obtain spectral information about DC-magnetic field. To make the spin oscillates freely, the spin needs to be put in a superposition state $(|0\rangle + |1\rangle)/\sqrt{2}$ that can be done by applying $\pi/2$-pulse (Fig. 2.9a). Under a static magnetic field perturbation, the spin precesses about $\hat{\boldsymbol{z}}$-axis along equator and pick up a phase during free evolution time (Fig. 2.9c)

$$\varphi = 2\pi\gamma_e \int_0^\tau B(t)dt. \tag{2.6}$$

A $\pi/2$-pulse after evolution time τ converts back the state of the spin to readable population at $|0\rangle$. The $|0\rangle$ population oscillates with frequency corresponding to detuning frequency δ of the actual resonant transition frequency of $m_s = -1$. With neighboring host ^{14}N ($S = 1$) hyperfinely coupled to the NV spin, the observed signal is no longer single-frequency oscillation but a

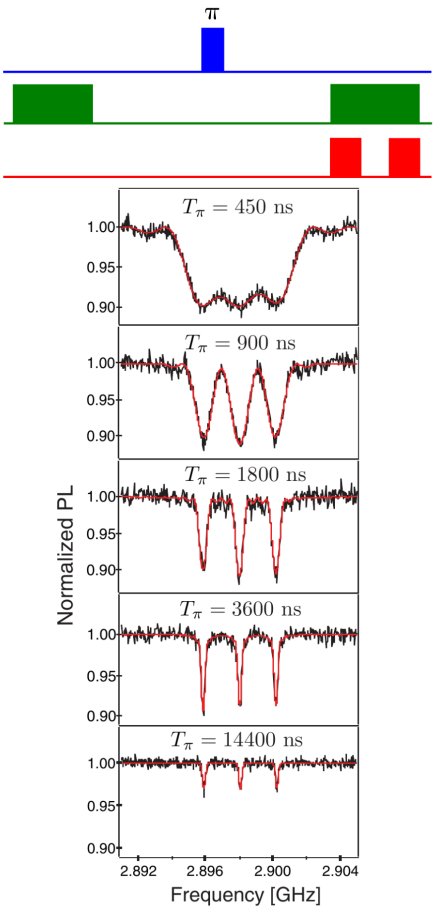

Figure 2.8: (top) Pulsed-ODMR sequence with π-pulse and microwave frequency sweep over repeated sequence. (bottom) Pulsed-ODMR spectra with different π-pulse duration T_π from reference [30]. Spectral resolution becomes better with longer π-pulse duration with trade-off of decreasing contrast.

sum of three frequencies (δ, $\delta + 2.2$ MHz, and $\delta - 2.2$ MHz) corresponding the triplet state of the ^{14}N.

Due to the existance of environmental paramagnetic spin bath like ^{13}C, which precess under external field with kHz frequency, the free oscillation of the NV spin will not undergo a coherent oscillation within measurement time. The precessing spin bath creates inhomogeneous field that change over time, inducing NV spin and contribute to the dephasing of the NV spin oscillation [33,34]. Consequently the free oscillation of NV spin will decay over a period of time defined as T_2^*, also known as dephasing time, depending on how abundant the paramagnetic spin bath around the NV spin.

Ramsey interferometry is a sensitive protocol for measuring static or slowly fluctuating magnetic field up to a frequency $\approx \tau^{-1}$ [13]. This is because if we have an oscillating magnetic field $B(t) = A\cos(\omega t + \alpha)$, with period equal to the free evolution time τ, the positive phase picked during the first half of evolution time will be cancelled by the negative phase picked during the second free evolution time as described in equation 2.6 [13]. As a result phase accumulated during the free evolution time τ is zero.

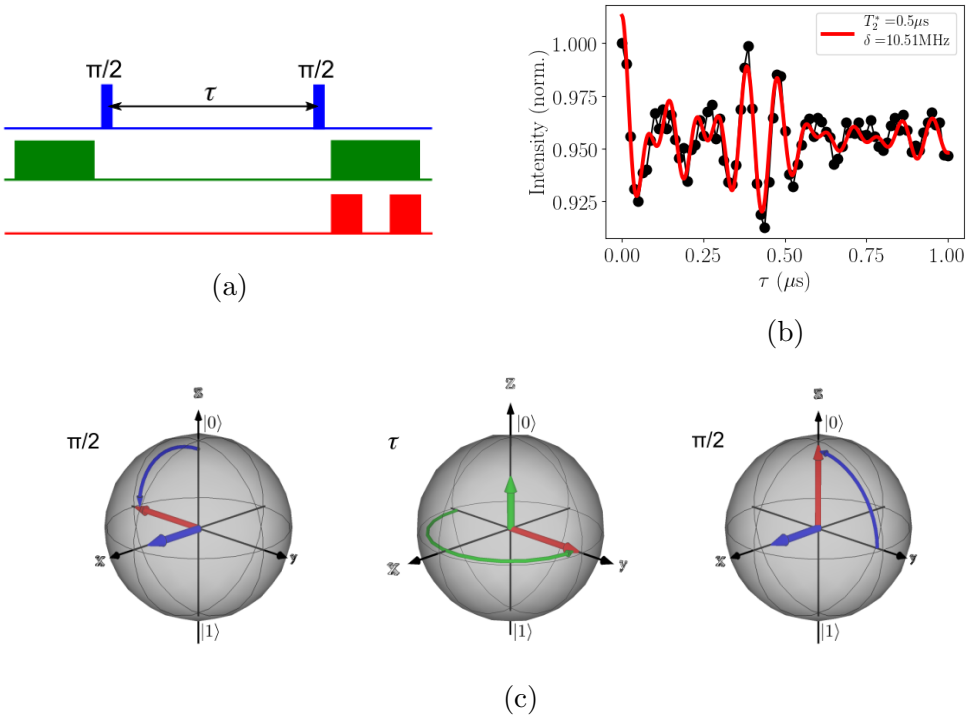

Figure 2.9: (a) Ramsey interferometry sequence consisting of $\pi/2$-pulse to make superposition state followed by free evolution time and another $\pi/2$-pulse to translate phase change into readable population. (b) Ramsey interferometry signal fitted by damped cosine of three frequency ($A[\Sigma_{n=0}^{3}\cos(\omega_n t+\varphi)]e^{-t/T_2^*}$) corresponding to resonance frequency of three hyperfine splitted resonance transition due to ^{14}N. (c) (left to right) Evolution of NV spin in Bloch sphere representation. $\pi/2$-pulse brings NV spin into its superposition state. During free evolution time τ the spin revolves along equator with frequency defined by detuned field (green arrow), picking phase φ. Another $\pi/2$-pulse brings back the NV spin to an optically readable state of $|0\rangle$.

2.2.6 Hahn Echo Spectroscopy

Dephasing effect that contributes to decoherence of free induction decay signal in Ramsey interferometry can be eliminated by flipping the NV spin 180° in the middle of its free evolution time (Fig. 2.10a). Applying π-pulse in the middle of free evolution time τ rotates NV spin by 180°, reversing its time evolution and refocusing the spin [13] (Fig. 2.10c). The phase accumulated during full free evolution time is given by

$$\varphi = 2\pi\gamma_e\left(\int_0^{\tau/2} B(t)dt - \int_{\tau/2}^{\tau} B(t)dt\right). \tag{2.7}$$

With Hahn echo protocol the dephasing effect from environmental spin bath can be eliminated and the time needed for the signal to decay becomes longer than T_2^*. This time constant is known as coherence time and denoted as T_2. The coherence time of spin in diamond NV center can be as long as ≈ 1.8 ms in ^{12}C (spinless) enriched diamond [27].

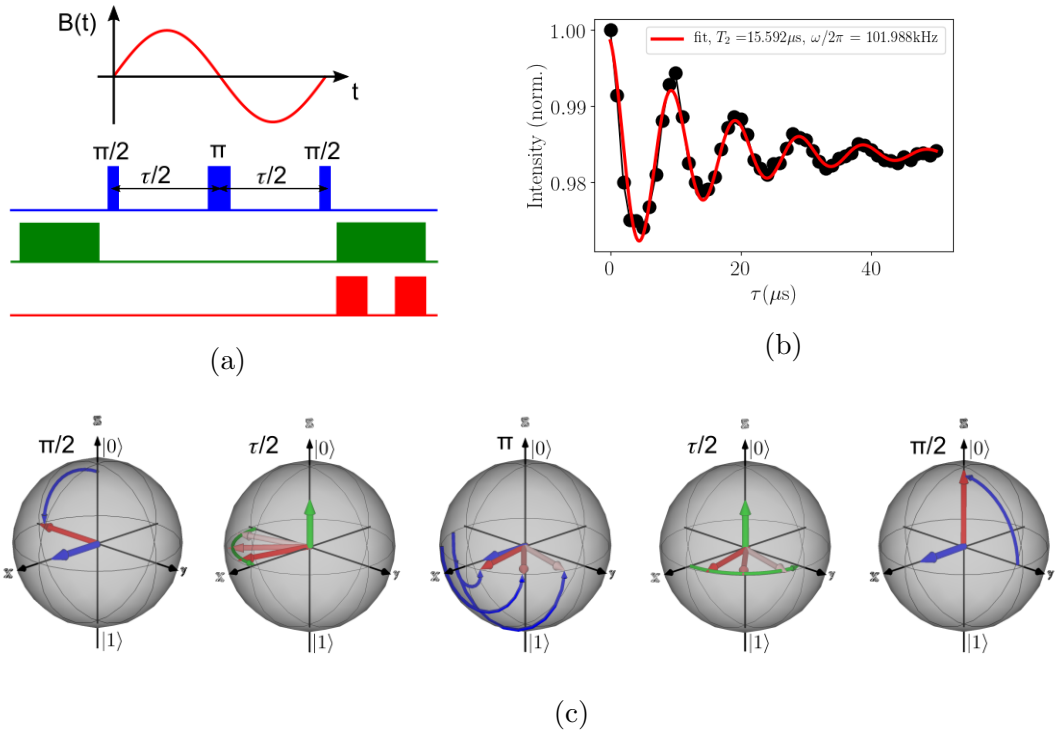

Figure 2.10: (a) With Hahn echo protocol the second half of oscillating magnetic field is reversed. resulting non-zero pahes accumulation within full free evolution time τ. (b) Hahn echo signal ($B_0 = 180$ G) showing periodic peaks corresponding to Larmor frequency of ^{13}C nuclear spin. (c) Bloch sphere representation of Hahn echo protocol. π-pulse in the middle of free evolution time τ rotates NV spin 180° around $\hat{\boldsymbol{x}}$-axis, reversing its time evolution and refocusing back the NV spin.

2.3 Noise Spectroscopy

Noise emanating from a condensed matter system can reveal information about the transport properties of its carriers [36]. Noise spectroscopy is a means to acquire frequency spectrum of stochastic signals from noise in order to understand the properties of condensed matter system. Electron spin in diamond with NV center is known to be a good noise sensor for a broad range of spectral noises from several kHz to several GHz [13, 14]. By analyzing decoherence and relaxation process of the NV spin under external perturbation produced by dynamical process in condensed matter system, spectral information about the perturbation can be reconstructed and dynamical properties of the system under investigation can be understood. A good understanding on the spectrum of noise under investigation will help in deciding proper sensing protocol to be deployed and maximizing sensitivity of measurement with NV centers [13].

2.3.1 Decoherence

Decoherence is a time range within which a quantum system can retain its quantum state evolution before its quantum wave function collapsed. For a

quantum sensor like NV spin in diamond decoherence determines how long it can be used to sense a physical unit. A quantum system can lost its coherence under different kind of noise processes. Decoherence leads to a decay in transition probability p of a quantum sensor during measurement time τ and can be defined as

$$p(t) = \frac{1}{2}(1 - e^{-\chi(\tau)}), \tag{2.8}$$

with $\chi(\tau)$ is decoherence function.

Environmental noise in close proximity to the NV spin can be examined with proper application of pulse sequence. In general decoherence function is defined as

$$\chi(\tau) = \frac{2}{\pi}\int_0^\infty \gamma^2 S(\omega)|Y(\omega)|^2 d\omega. \tag{2.9}$$

$|Y(\omega)|^2$ is the filter function of the pulse sequence in use, in frequency domain, which defined in Fourier transform as

$$Y(\omega) = \int_0^t y(\tau')e^{i\omega\tau} d\tau', \tag{2.10}$$

where $y(\tau')$ is modulation function of the pulse sequence. For Ramsey and spin echo sequence, filter functions are defined respectively by

$$|Y_R(\omega)|^2 = \left|\frac{\sin(\omega\tau/2)}{\omega/2}\right|^2 \tag{2.11}$$

$$|Y_{SE}(\omega)|^2 = \left|\frac{\sin^2(\omega\tau/4)}{\omega/4}\right|^2. \tag{2.12}$$

Figure 2.11 shows filter function $Y(\omega)$ of Ramsey, Hahn echo, and T_1 measurement protocol as a function of frequency. Spectral noise function $S(\omega)$, which define the interaction between the NV spin and environment, can be analyzed by spectral decomposition technique by deconvolving equation 2.9 [37].

2.3.2 Relaxometry

Relaxometry is a technique to relate environmental noise spectral power function $S(\omega)$ to the rate of decoherence decay rate Γ. In general Decoherence can be written in relation to decay rate as

$$\chi(\tau) = (\Gamma t)^a, \tag{2.13}$$

with $a = 1, \ldots, 3$ depending on different noise process. Decay rate is associated to decoherence or relaxation time $T_\chi = \Gamma^{-1}$. In principal relaxometry assumes the noise process is a Markovian process, a in equation 2.13 is equal to one, and weak noise strength.

Relaxometry is based on two-level system perturbation theory which calculate transition probability between two energy level $|\psi_0\rangle$ and $|\psi_1\rangle$ during measurement time τ [13]

$$\begin{aligned}|c_1(\tau))|^2 &= |\langle\psi_1|\hat{H}_v(\omega)|\psi_0\rangle|^2 \left(\frac{\sin[(\omega_{01}-\omega)\tau/2]}{(\omega_{01}-\omega)/2}\right)^2 \\ &\approx 2\pi|\langle\psi_1|\hat{H}_v(\omega)|\psi_0\rangle|^2\tau\delta(\omega_{01}-\omega),\end{aligned}$$

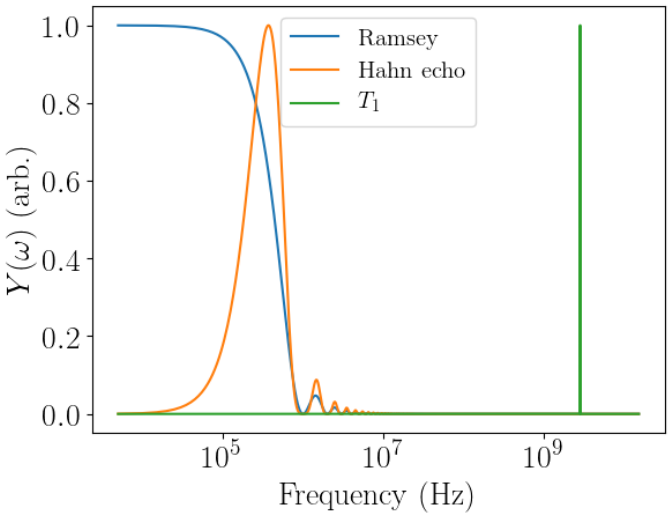

Figure 2.11: Filter function of Ramsey, Hahn echo and T_1 measurement sequence. Each measurement sequence has different sensitivity in specific frequency window, with Ramsey 0 - 1 MHz, Hahn echo 0.1 - 1MHz, and $T_1 \sim 3$ GHz. Parameters adopted from [38].

where $\hat{H}v(\omega)$ is signal Hamiltonian which define the coupling between NV spin to environmental noise signal. The second line equation define transition probability over a large τ. The rate of transition is then can be written as

$$\frac{\delta|c_1(\tau)|^2}{\delta\tau} \approx 2\pi|\langle\psi_1|\hat{H}_v(\omega)|\psi_0\rangle|^2\delta(\omega_{01}-\omega), \tag{2.14}$$

and transition probability rate over all frequency is

$$\begin{aligned}\Gamma &= \frac{1}{\pi}\int_0^\infty 2\pi|\langle\psi_1|\hat{H}_v(\omega)|\psi_0\rangle|^2\delta(\omega_{01}-\omega) \\ &= 2|\langle\psi_1|\hat{H}_v(\omega_{01})|\psi_0\rangle|^2 \\ &= 2\gamma_e^2 S_{v01}(\omega_{01})|\langle\psi_1|\sigma_v/2|\psi_0\rangle|^2.\end{aligned} \tag{2.15}$$

$S_{v01}(\omega_{01})$ is spectral power density of the noise that drives transition between the two level and σ_v is vector of pauli matrix. Equation 2.15 relates transition (decoherence or relaxation) rate and spectral power density of the noise at certain frequency. This transition rate can be between any state in quantum sensor, in the case of NV spin it can be between $|0\rangle$ and $|1\rangle$ (for T_1 relaxometry)or between superposition state $|\pm 1\rangle = (|0\rangle \pm e^{-i\omega_0\tau}|1\rangle)/\sqrt{2}$ (for T_2^* or T_2 relaxometry).

T_1 Relaxometry

The spin-lattice relaxation rate $\Gamma_1 = T_1^{-1}$ defines transition rate between $|0\rangle$ and $|1\rangle$ due to the exchange of energy between NV spin and environment. Therefore, relaxometry with T_1 is sensitive to noise with frequency about the transition frequency of the NV spin $\omega_{NV} = D_{gs} \pm \gamma_e B_0$.

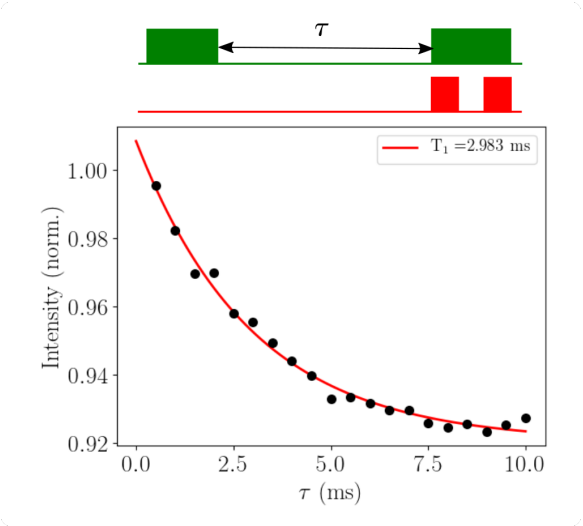

Figure 2.12: T_1 relaxometry sequence consist of laser initialization and read out pulse. By varying dark time τ relaxation of NV spin between $|0\rangle$ and $|1\rangle$ over a period of time can be observed. Typical relaxation time for ensemble of NV spins in bulk diamond is $1 \sim 5$ ms.

T_1 relaxometry measurement can be done by initializing NV spin to $|0\rangle$ at time $\tau' = 0$ and reads the transition probability after $\tau' = \tau$ without further manipulation of the quantum state (Fig. 2.12). In general the spin-lattice relaxation rate can be defined as [17, 38, 40]

$$\frac{1}{T_1} = \left(\frac{1}{T_1}\right)_{\text{int}} + \int \gamma_e^2 \langle B_\perp \rangle^2 S(\omega) Y_{T_1}(\omega) d\omega, \tag{2.16}$$

with $(1/T_1)_{\text{int}}$ is intrinsic relaxation rate of the NV spin in the absence of external noise and $\langle B_\perp \rangle^2 = \langle B_x^2 \rangle + \langle B_y^2 \rangle$ is the variance of transverse magnetic field of environment noise. The filter function of T_1 relaxometry can be written as [38]

$$Y_{T_1}(\omega) = \frac{1}{\pi} \frac{\Gamma}{\Gamma^2 + (\omega - \omega_{NV})^2}, \tag{2.17}$$

with $\Gamma = 1/T_2^*$.

T_1 relaxometry with NV spin has been demonstrated to be an effective measurement technique for detecting high frequency (in GHz range) environmental noise including Gd^{3+} ions [17, 40], ferritin proteins [38], surface paramagnetic defect on diamond [41], and spin-phonon interactions within diamond NV [39].

Chapter 3

Magnetization Dynamics in Magnetically Ordered Media

In a many-body spin system, coupling between neighboring spins resulted in engrossing phenomena that can be harnessed in various useful technological applications. One particular phenomena involving propagation of elementary excitation of coupled spins in a magnetically ordered structure, known as spin wave, has attracted great interest due to its potential as a low-loss information carrier and processor [5]. Basic theoretical treatment of spin waves in a medium composed small number of atoms and ions with angular momenta (microscopic) and a medium with large number of momenta (macroscopic) will be given in this chapter, followed by a brief discussion on thermally excited spin waves where the interplay between heat and spins resulted in magnetic fluctuation.

3.1 Quantum Theory of Spin Wave

Condensed matter system involves many individual atoms and ions that interact one to another, with each individual atom and ion posses angular momentum. Interaction between individual atom with spin determines magnetic ordering of a system (Fig. 3.1). In microscopic scale, interaction between N spins is governed by exchange interaction which given by Heisenberg Hamiltonian

$$H = -2\frac{J}{\hbar^2}\sum_n \mathbf{S}_n \cdot \mathbf{S}_{n+1}. \tag{3.1}$$

$\mathbf{S}_n$ is spin operator at n-th site and $J = \frac{1}{2}(E_S - E_T)$ is the so-called exchange constant with E_S and E_T respectively is eigen energy of singlet state and triplet state. For $J > 0$ the system will be in ferromagnetic ordering, all spins aligned in parallel fashion. Whereas, for $J < 0$ the system will be in antiferromagnetic ordering, spins aligned in anti-parallel fashion.

Spin waves can be examined by considering three dimensional ferromagnet under external magnetic bias B_0. The Hamiltonian of the system is expressed

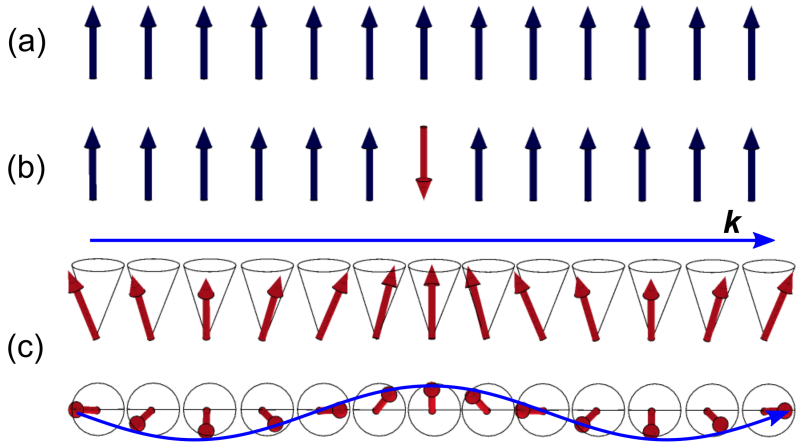

Figure 3.1: (a) Illustration of ground state ferromagnetic ordering where all spins are aligned up. (b) First excitation condition happened when one of the spin in the system is flipped. However, lower excitation energy can be formed when the excitation is shared among the spins, leading to the redistribution of spin flip to the nearest neighboring spins in the form of wave (c). This wave of spins can be seen as precessing spins relative to its spin orientation in lattice in which the phase of successive neighboring precession linearly vary.

as Heisenberg Hamiltonian with addition of Zeeman energy

$$H = -2\frac{J}{\hbar^2}\sum_{j,\boldsymbol{\delta}} \mathbf{S}_J \cdot \mathbf{S}_{j+\boldsymbol{\delta}} - \frac{g\mu_B B_0}{\hbar}\sum_j S_{jz}. \tag{3.2}$$

$\boldsymbol{\delta}$ represents vector of nearest neighbor site to j, g is gyromegnatic ratio of electron, and μ_B is the Bohr magneton. With $B_0 > 0$ the ground state of the system is all spins in the system are aligned up.

Expressed with lowering and raising spin operators, the Hamiltonian can be expressed as

$$H = -2\frac{J}{\hbar^2}\sum_{j,\boldsymbol{\delta}}\left[\frac{1}{2}(S_j^- S_{j+\boldsymbol{\delta}}^+ + S_j^+ S_{j+\boldsymbol{\delta}}^-) + S_{jz}S_{j+\boldsymbol{\delta},z}\right] - \frac{g\mu_B B_0}{\hbar}\sum_j S_{jz}. \tag{3.3}$$

Examining the flipping of spin distributed over a group of spins s at j site, Holstein and Primakoff [45] introduced magnon (quasi-particle of spin wave) creation and annihilation operators that respectively symbolized as a_j^+ and a_j. These operators can be related to raising and lowering operators of spin respectively as

$$S_j^+ \approx \hbar\sqrt{2s}a_j, \tag{3.4}$$

$$S_j^- \approx \hbar\sqrt{2s}a_j^+, \tag{3.5}$$

with s is the total on certain site. Since the Hamiltonian involved a collective excitation of all the spins in the system, the magnon creation and annihilation

operators can be expressed as inverse of Fourier transform

$$a_j^+ = N^{-1/2} \sum_{\mathbf{k}} e^{-i\mathbf{k}\cdot\mathbf{r}_j} a_{\mathbf{k}}^+ \tag{3.6}$$

$$a_j = N^{-1/2} \sum_{\mathbf{k}} e^{i\mathbf{k}\cdot\mathbf{r}_j} a_{\mathbf{k}}. \tag{3.7}$$

$\mathbf{r}_j$ expresses a vector that locates the j-th site and $a_{\mathbf{k}}^+$ and $a_{\mathbf{k}}$ are respectively creation and annihilation operators of magnon with wave vector $\mathbf{k}$ which commute with relation $[a_{\mathbf{k}}, a_{\mathbf{k'}}^+] = \delta_{\mathbf{k},\mathbf{k'}}$.

With the Holstein-Primakoff transformation (Eqn. 3.4) in hand dispersion relation of magnon in crystal can be calculated by considering Hamiltonian with Z nearest neighbor

$$H = -2JNZs^2 - g\mu_B B_0 Ns + H_0, \tag{3.8}$$

where

$$\begin{aligned} H_0 = -\frac{2Js}{N} \sum_{j\boldsymbol{\delta}\mathbf{k}\mathbf{k'}} (& e^{-1(\mathbf{k}-\mathbf{k'})\cdot\mathbf{r}_j} e^{i\mathbf{k'}\cdot\boldsymbol{\delta}} a_{\mathbf{k}}^+ a_{\mathbf{k'}} + e^{i(\mathbf{k}-\mathbf{k'})\cdot\mathbf{r}_j} e^{-i\mathbf{k'}\cdot\boldsymbol{\delta}} a_{\mathbf{k}} a_{\mathbf{k'}}^+, \\ & - e^{-1(\mathbf{k}-\mathbf{k'})\cdot\mathbf{r}_j} a_{\mathbf{k}}^+ a_{\mathbf{k'}} - e^{-i(\mathbf{k}-\mathbf{k'})\cdot(\mathbf{r}_j+\boldsymbol{\delta})} a_{\mathbf{k}}^+ a_{\mathbf{k'}}) \\ & + \frac{g\mu_B B_0}{N} \sum_{j\mathbf{k}\mathbf{k'}} e^{-i(\mathbf{k}-\mathbf{k'})\cdot\mathbf{r}_j} a_{\mathbf{k}}^+ a_{\mathbf{k'}}. \end{aligned} \tag{3.9}$$

Summing over all j will cause all of the terms to vanish but $\mathbf{k} = \mathbf{k'}$. Hamiltonian becomes

$$H_0 = -2JsZ \sum \mathbf{k} (\gamma_{\mathbf{k}} a_{\mathbf{k}^+} a_{\mathbf{k}} + \gamma_{-\mathbf{k}} a_{\mathbf{k}} a_{\mathbf{k}}^+ - 2a_{\mathbf{k}}^+ a_{\mathbf{k}} + g\mu_B B_0 \sum_{\mathbf{k}} a_{\mathbf{k}}^+ a_{\mathbf{k}}, \tag{3.10}$$

with

$$\gamma_{\mathbf{k}} = \sum_{\boldsymbol{\delta}} e^{i\mathbf{k}\cdot\boldsymbol{\delta}}. \tag{3.11}$$

For crystal with center of symmetry $\gamma_{\mathbf{k}} = \gamma_{-\mathbf{k}}$ and considering commutation relation of creation and annihilation operator, Hamiltonian can be further simplified as

$$\begin{aligned} H_0 &= -sJsZ \sum_{\mathbf{k}} (\gamma_{\mathbf{k}} a_{\mathbf{k}}^+ a_{\mathbf{k}} + \gamma_{\mathbf{k}} (1 + a_{\mathbf{k}}^+ a_{\mathbf{k}}) - 2a_{\mathbf{k}}^+ a_{\mathbf{k}}) + g\mu_B B_0 \sum_{\mathbf{k}} a_{\mathbf{k}}^+ a_{\mathbf{k}} \\ &= -4JsZ \sum_{\mathbf{k}} (\gamma_{\mathbf{k}} - 1) a_{\mathbf{k}}^+ a_{\mathbf{k}} + g\mu_B B_0 \sum_{\mathbf{k}} a_{\mathbf{k}}^+ a_{\mathbf{k}} \\ &= \sum_{\mathbf{k}} (4JsZ(1 - \gamma_{\mathbf{k}}) + g\mu_B B_0) a_{\mathbf{k}}^+ a_{\mathbf{k}}. \end{aligned} \tag{3.12}$$

By taking $\hat{n}_{\mathbf{k}} = a_{\mathbf{k}}^k a_{\mathbf{k}}$ as the number of magnons with wave vector $\mathbf{k}$, Hamiltonian can be rewritten as

$$H_0 = \sum_{\mathbf{k}} \hat{n}_{\mathbf{k}} \hbar\omega_{\mathbf{k}}. \tag{3.13}$$

The last term of the Hamiltonian define dispersion relation of the magnons in a spin system;

$$\hbar\omega_{\mathbf{k}} = 4JsZ(1 - \gamma_{\mathbf{k}}) + g\mu_B B_0. \tag{3.14}$$

3.2 Magnetization Dynamics

In a media with a large number of angular momenta, magnetic properties are treated by examining magnetic dipole moment per unit volume of magnetization and its interaction with applied magnetic field. Magnetization in magnetically ordered media is defined as

$$\mathbf{M} = \mathbf{M}_0 + \overline{\boldsymbol{\chi}} \cdot \mathbf{H}, \tag{3.15}$$

with $\overline{\boldsymbol{\chi}}$ and $\mathbf{H}$ are magnetic susceptibility and applied magnetic field, respectively.

For ferromagnetic media, where spontaneous magnetic moment exist in the absence of applied magnetic field, total magnetic field is defined as the sum of applied field and additional component called exchange field $\mathbf{H}_{\text{ex}}$;

$$\mathbf{H}_{\text{tot}} = \mathbf{H} + \mathbf{H}_{\text{ex}}. \tag{3.16}$$

This exchange field is proportional to the thermally averaged magnetic field through relation

$$\mathbf{H}_{\text{ex}} = \lambda \mathbf{M}. \tag{3.17}$$

At high temperature and low field, magnetic ordering in ferromagnetic media is governed by Curie-Weiss law

$$\chi = \frac{M}{H} = \frac{C}{T - T_c}, \tag{3.18}$$

where T_c defines Curie temperature

$$T_c = \lambda C = \frac{\lambda \mu_0 N p^2 \mu_B^2}{3k_B}. \tag{3.19}$$

$k_B = 1.38{\times}10^{-23}$ J/K is Boltzman constant, while λ, N, and $p = g[(J(J{+}1)]^{1/2}$ are exchange field constant, number of moments per unit volume, and effective magneton number.

Furthermore, the exchange field is nothing but exchange interaction between Z nearest neighboring angular momenta in ferromagnet with additional contribution of applied magnetic field (Zeeman energy)

$$\mathbf{H}_{\text{ex}} = -\frac{2ZJ}{g\mu_0\mu_B}\mathbf{S}. \tag{3.20}$$

Using expression that relates magnetization $\mathbf{M}$ and magnetic moment $\boldsymbol{\mu}$: $\mathbf{M} = N\boldsymbol{\mu}$ and knowing that $\boldsymbol{\mu} = -g\mu_B\mathbf{S}$, exchange field can be rewritten in relation to exchange field coefficient λ as

$$\mathbf{H}_{\text{ex}} = \frac{2ZJ}{\mu_0 N g^2 \mu_B^2}\mathbf{M} = \lambda \mathbf{M} \tag{3.21}$$

with

$$\lambda = \frac{2ZJ}{\mu_0 N g^2 \mu_B^2}. \tag{3.22}$$

Here Exchange constant can be related to the Curie temperature through

$$J = \frac{3k_B T_c}{2ZS(S+1)}. \tag{3.23}$$

Equation of Motion of Magnetization

Under magnetic field, angular momentum **J** undergoes a precessional motion defined by

$$\frac{d\mathbf{J}}{dt} = \gamma\mu_0 \mathbf{J} \times \mathbf{H}_{\text{eff}}. \tag{3.24}$$

In the equation, effective magnetic field $\mathbf{H}_{\text{eff}}$ is given of the contribution from all torque-producing effective field

$$\mathbf{H}_{\text{eff}} = \mathbf{H} + \mathbf{H}_{\text{ex}} + \mathbf{H}_k, \tag{3.25}$$

with $\mathbf{H}$, $\mathbf{H}_{\text{ex}}$, and $\mathbf{H}_k$ are respectively applied external field, exchange field and anisotropy field. By multiplying both sides of the equation of motion with γN and knowing that $\mathbf{M} = \gamma N \mathbf{J}$, equation of motion of magnetization (Landau-Lifshitz equation) is expressed as

$$\frac{d\mathbf{M}}{dt} = \gamma\mu_0 \mathbf{M} \times \mathbf{H}_{\text{eff}}. \tag{3.26}$$

Solving the equation of motion of magnetization under additional small time-varying field $\mathbf{M} = \mathbf{M}_0 + \mathbf{m}(t)$ and $\mathbf{H} = \mathbf{H}_0 + \mathbf{h}(t)$ resulted in

$$\mathbf{m} = \overline{\boldsymbol{\chi}} \cdot \mathbf{h}, \tag{3.27}$$

with Polder susceptibility tensor

$$\overline{\boldsymbol{\chi}} = \begin{bmatrix} \chi & -i\kappa \\ i\kappa & \chi \end{bmatrix} \tag{3.28}$$

and

$$\chi = \frac{\omega_0 \omega_M}{\omega_0^2 - \omega^2} \tag{3.29}$$

$$\kappa = \frac{\omega \omega_M}{\omega_0^2 - \omega^2} \tag{3.30}$$

$\omega_0 \equiv -\gamma\mu_o H_0$ is referred as ferromagnetic resonance and $\omega_M \equiv -\gamma\mu_0 M_s$.

Equation 3.29 is mathemathically problematic since susceptibility will become infinity as $\omega = \omega_0$. The Landau-Lifshitz equation is an idealized equation of motion for magnetization in which magnetization precesses forever without losing energy. This non-intuitive picture of magnetization motion can be remodeled by introducing damping torque to the equation of motion which will also resolve infinite susceptibility. Physically, damping torque can be viewed as transfer of energy from the precessional motion of magnetization to the crystal lattice vibration [43]. Mediated by this lattice vibration motion, spins at different sites in crystal can be coupled dipolarly.

Landau-Lifshitz equation with additional damping term was introduced by Gilbert as [46, 47]

$$\frac{d\mathbf{M}}{dt} = \gamma\mu_0(\mathbf{M} \times \mathbf{H}_{\text{eff}}) + \frac{\alpha}{M_s}\left(\mathbf{M} \times \frac{d\mathbf{M}}{dt}\right). \tag{3.31}$$

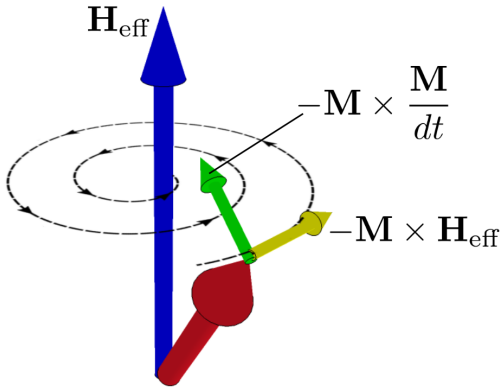

Figure 3.2: Landau-Lifshitz-Gilbert equation of magnetization motion illustrated as precession motion spiraling back to its equilibrium position coliniear with $\mathbf{H}_{\text{eff}}$ due to the damping torque.

This equation of motion is known as Landau-Lifshitz-Gilbert (LLG) equation. Solving LLG equation will introduce additional term to the Polder tensor by substituting ω_0 with $\omega_0 - i\omega\alpha$, and susceptibility will no longer infinite when $\omega_0 = \omega$. Time varying magnetization motion in x and y are given by damped sine and cosine function

$$m_x(t) \approx \omega_M e^{-\alpha\omega_0 t} \sin(\omega_0 t) u(t) \tag{3.32}$$
$$m_y(t) \approx -\omega_M e^{-\alpha\omega_0 t} \sin(\omega_0 t) u(t). \tag{3.33}$$

Above equation of motion can be interpreted as a motion of magnetization that tilted away from $\hat{\boldsymbol{z}}$-axis in the direction of $\mathbf{M} \times \mathbf{h}_{\text{eff}}$, spiraling and returned to its equilibrium position due to the transverse damping torque (Fig. 3.2).

3.3 Magnetostatic Spin Wave

When the wave number k of spin wave is much smaller than the spacing between spins ($k \ll \pi/a$), spin wave can be approximated by magnetostatic Maxwell equation

$$\nabla \times \mathbf{h} = 0 \tag{3.34}$$
$$\nabla \cdot \mathbf{b} = 0 \tag{3.35}$$
$$\nabla \times \mathbf{e} = i\omega\mathbf{b}. \tag{3.36}$$

Solving the magnetostatic Maxwell equation for an electromagnetic wave propagating in a magnetized magnetic medium in the absence of exchange and anisotropy, dispersion relation of the wave is given by

$$\omega = [\omega_0(\omega_0 + \omega_M \sin^2\theta)]^{1/2}, \tag{3.37}$$

with θ is the angle between DC bias field and propagation vector of the wave.

Treated in the presence of exchange interaction, dispersion relation of the spin wave can be rewritten by replacing ω_0 by $\omega_0 + \omega_M \lambda k^2$;

$$\omega = [(\omega_0 + \omega_M \lambda k^2)(\omega_0 + \omega_M(\lambda k^2 + \sin^2\theta))]^{1/2}. \tag{3.38}$$

We can see from Eqn. 3.38 that when k is very small, the exchange term λk^2 will become much smaller that unity and dispersion relation will approximates to the one given by Eqn. 3.37. From here we can conclude that when λk^2 is much smaller than unity dipolar interaction from magnetic moment will be dominant and the excitation is usually called dipolar spin wave. In contrast, when k is very large and exchange term λk^2 much larger than unity exchange interaction will be dominant over dipolar interaction and excitation is called exchange spin wave.

Modes of magnetostatic spin wave in thin film magnetic media is characterized by the orientation of DC bias field relative to the direction of propagation of the spin wave (Fig. 3.3). There are three distinct modes of magnetostatic spin wave which can be marked by their distinct dispersion relation. Forward volume magnetostatic spin waves (FVMSW) with bias field normal to its surface and spin waves that propagate perpendicular to the bias field have dispersion relation approximated by

$$\omega_{FVMSW} = \sqrt{\omega_0 \left[\omega_0 + \omega_M \left(1 - \frac{1 - e^{-kd}}{kd}\right)\right]}, \tag{3.39}$$

with d is the film thickness. Backward volume magnetostatic spin waves (BVMSW) are marked by propagation direction that parallel to in-plane bias magnetic field. Dispersion relation of BVMSW is approximately given by

$$\omega_{BVMSW} = \sqrt{\omega_0 \left[\omega_0 + \omega_M \left(\frac{1 - e^{-kd}}{kd}\right)\right]}. \tag{3.40}$$

Magnetostatic surface spin waves (MSSW) is characterized by spin wave that propagates perpendicular to in-plane bias field. Their dispersion relation is approximately given by

$$\omega_{MSSW} = \sqrt{\omega_0(\omega_0 + \omega_M) + \frac{\omega_M^2}{4}[1 - e^{-2kd}]}. \tag{3.41}$$

Propagation direction of MSSW can be easily defined by a vector that parallel to $\mathbf{H} \times \mathbf{n}$, with $\mathbf{n}$ is vector normal to the surface. MSSW's precession amplitude is distributed exponentially along the film thickness with highest amplitude located at one surface where MSSW are propagate.

3.4 Thermally Excited Spin Waves

Along with excitation by time-varying magnetic field, magnons can also be excited by thermal fluctuation. The distribution of magnons of wave number k in thermal equilibrium is given by Planck distribution

$$\langle n_k \rangle = \frac{1}{e^{\hbar\omega_k / k_B T} - 1}. \tag{3.42}$$

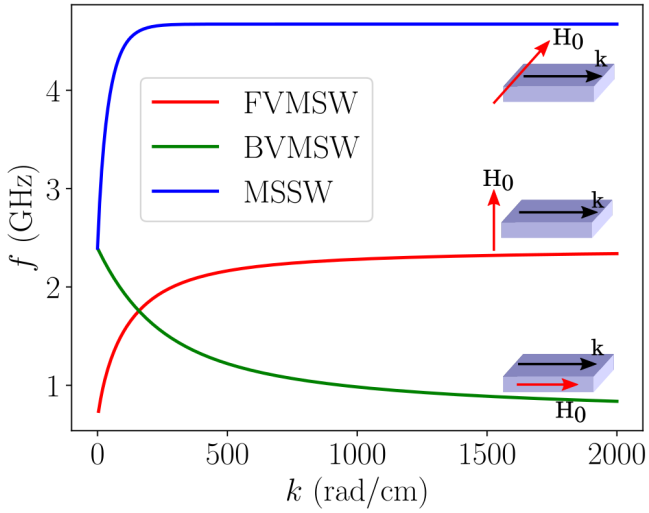

Figure 3.3: Dispersion relation of three modes of magnetostatic spin wave in yttrium iron garnet ($Y_5Fe_{12}O_3$) with thickness of 100 μm at bias field $H_0 = 150$ Oe and saturation magnetization $4\pi M_s = 1750$ G [48].

At temperature T, the total number of magnons is given by integrating number of magnons over the first Brillouin zone $\mathbf{k}$

$$\sum_{\mathbf{k}} n_{\mathbf{k}} = \int d\omega D(\omega)\langle n(\omega)\rangle, \tag{3.43}$$

with $D(\omega)$ is magnon density.

Approximating magnon dispersion relation at wavelength larger than lattice constant a, $ka \ll 1$, as $\hbar\omega = 2Jsa^2k^2$, the total number of magnons is given by

$$\sum_{\mathbf{k}} n_{\mathbf{k}} = \frac{1}{4\pi^2}\left(\frac{\hbar}{2Jsa^2}\right)^{3/2}\int_0^\infty d\omega \frac{\omega^{1/2}}{e^{\hbar\omega/k_BT}-1}. \tag{3.44}$$

Fractional change in magnetization can be calculated as the total number of magnons per number of of atoms N_a in a unit volume

$$\frac{\Delta M}{M(0)} = \frac{\sum n_{\mathbf{k}}}{N_a s} = \frac{0.0587}{sQ}\left(\frac{k_BT}{2Js}\right)^{3/2}. \tag{3.45}$$

The equation is known as Bloch $T^{3/2}$ law.

Thermal magnon can propagate diffusively when subjected to non-equilibrium condition through build-up of magnon chemical potential gradient $\nabla\mu_m$ and temperature gradient ∇T [50–54]. This propagation of thermal magnons is considered as current of spin which can be described by diffusion equation [53]

$$\frac{2e}{\hbar}\mathbf{j}_m = -\sigma_m\nabla\mu_m + \zeta\nabla T, \tag{3.46}$$

where σ_m is magnon conductivity, ζ is intrinsic spin Seebeck coefficient, and T is temperature of the material. Experimentally, thermal magnon is known to have diffusion length of over 9 μm at room temperature [51] and over 80 μm at 10 K [53] in ferrimagnetic insulator yttrium iron garnet (YIG).

Chapter 4

Materials Preparation and Experimental Setup

4.1 Diamond and Nitrogen-Vacancy Center Creation

Electronic grade CVD (chemical vapor deposition) diamond (EDP Corporation) with (110) crystal orientation is used in the experiment. The diamond were cut from $2.5 \times 2.5 \times 0.3$ mm^3 diamond chip into diamond beam with dimension of $2.5 \times 0.1 \times 0.1$ mm^3 (Fig. 4.1) by Syntek Co., Ltd. NV defects in diamond were created by implanting $^{14}N^+$ ions using ion source facility at JAIST Center for Nano Materials and Technology with implantation energy of 30 keV and implantation dose of 1×10^{12} ions/cm^2 with tilt angle of 7° for preventing ion channeling [42]. Nitrogen-vacancy pairs are formed after annealing process at 900° C for 2 hours (Fig. 4.2).

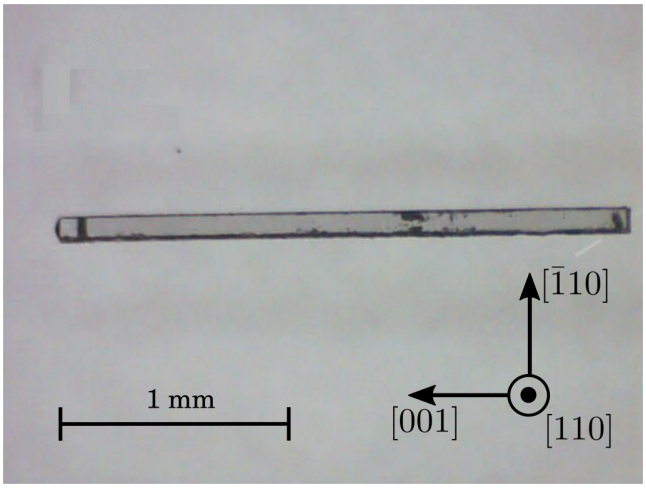

Figure 4.1: Diamond beam (110) with NV center used in the experiment.

NV defects layer is formed at the depth of about 33 nm from diamond surface according to stopping and range of ions in matter (SRIM) simulation (Fig. 4.3) [55]. For SRIM simulation diamond substrate density of 3.52 g/cm^3 and displacement energy of 37.5 eV are used [56, 57]. Assuming that laser

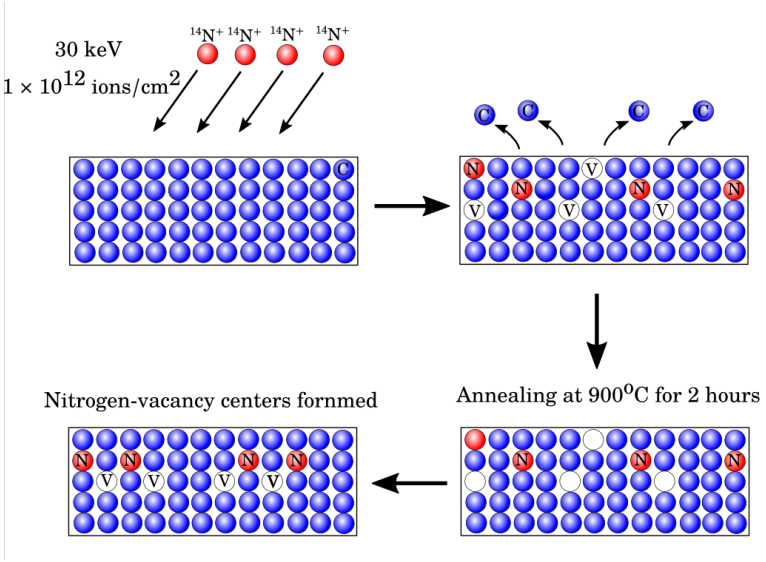

Figure 4.2: Illustration of NV creation process by ion implantation and annealing process.

reached Abbe's diffraction limit with the objective lens used in the confocal microscope (NA = 0.6) and about 6% of the nitrogen ions are converted to NV [58, 59], the number of NV per laser spot volume is about 6.24 $\times 10^5$.

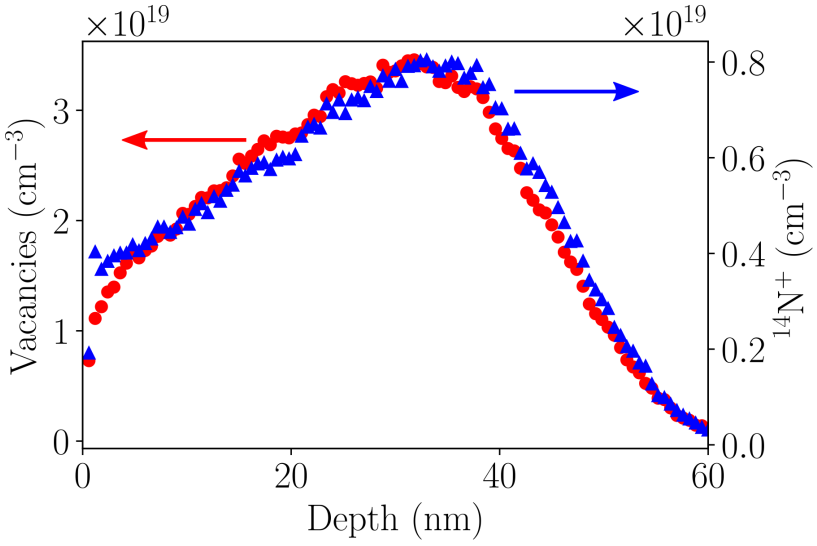

Figure 4.3: Distribution of $^{14}N^+$ ions and vacancy over certain range of depth.

4.2 Yttrium Iron Garnet

Yttrium iron garnet (YIG), $Y_5Fe_{12}O_3$, is a ferrimagnetic insulator with complex structure. Its ferrimagnetic characteristic comes from Fe^{3+} ions that occupy two different sub-lattices of octahedral and tetrahedral structure. In this experiment we use trilayer structure of YIG/GGG(gadolinium galium

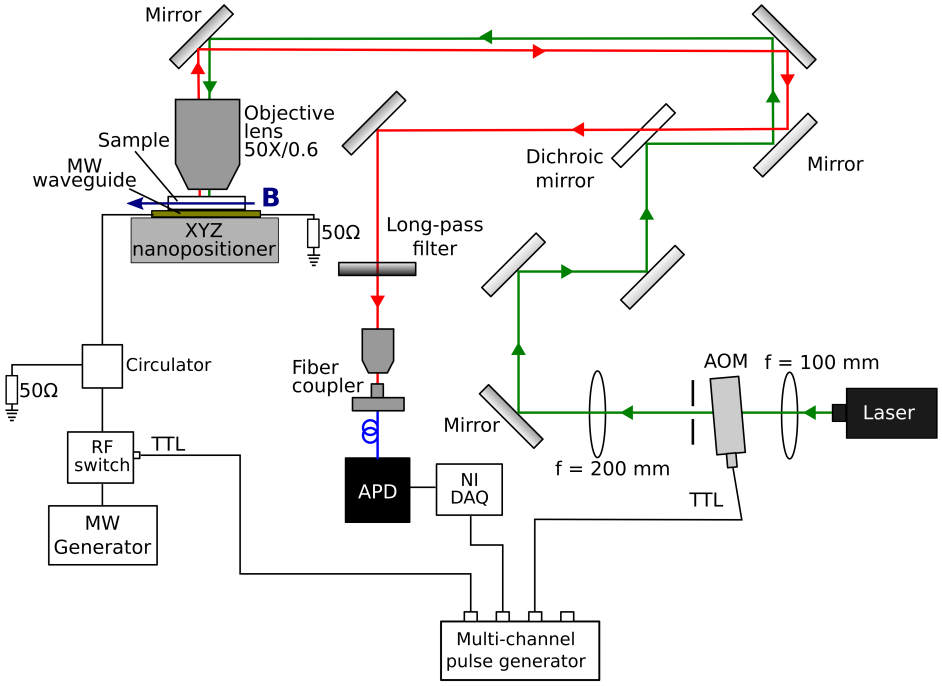

(a)

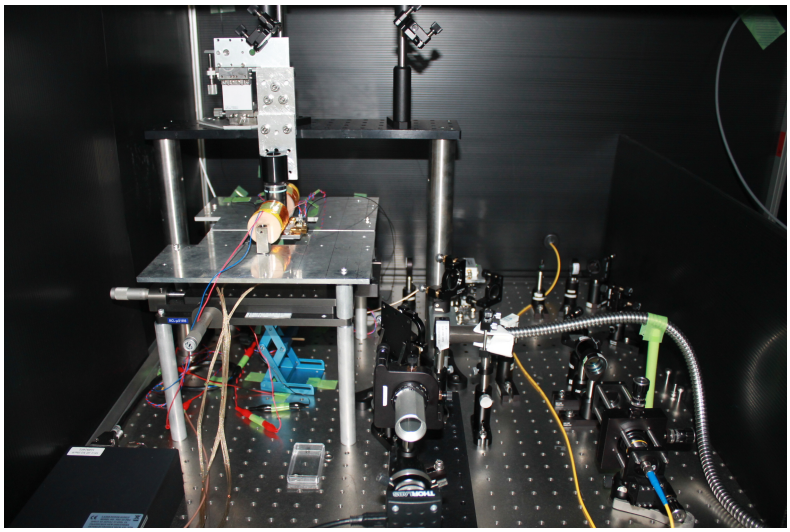

(b)

Figure 4.4: (a) Confocal microscope system used in the experiment to manipulate and read out the quantum state of NV spin. Microwave generator provide microwave for two-level energy manipulation. Pulsed measurement system is done by the aid of high speed programmable pulse generator. (b) Photograph of the scanning confocal microscope

garnet)/YIG with thickness of 0.75 mm provide by Shin Etsu Lot Number SEW-3707. The thickness of YIG on each side in this structure is 0.1 mm.

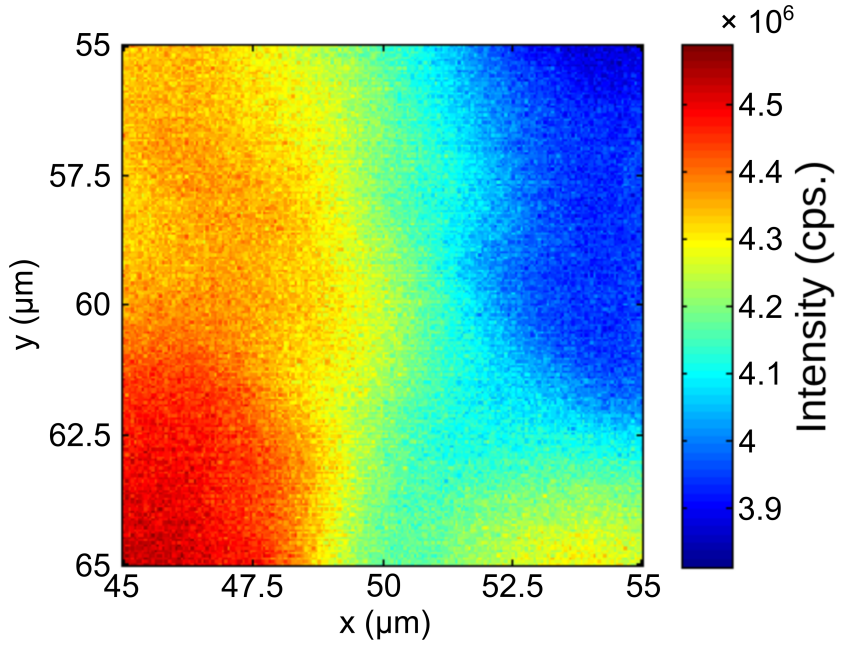

Figure 4.5: 10 μm $\times$ 10 μm scanning fluorescence image at an area around the middle of the long dimension of the diamond beam with ensemble of NV centers.

4.3 Scanning Confocal Microscope

The experiment is conducted under ambient conditions with a home-build scanning confocal microscope (Fig. 4.4a and b). Optical excitation of NV spin is provided by 532 nm laser (MGL-III-532-20mW Changchun New Industries Optoelectronics Technology Co., Ltd.) with 1 mW of power focused on acousto-optical modulator (AOM) (Isomet 1250C) to provide controlled pulse excitation. The laser is delivered through optical lines consisting of a series of plano-convex lenses (Thorlabs PF10-03-P01), mirrors (Thorlabs LA1509-YAG), and a dichroic mirror (Semrock LPD01-532RS-25) and focused to the sample through 50×, NA = 0.6 objective lens (Nikon TU Plan ELWD).

The fluorescence emitted by NV spin is filtered by a high-pass filter (Semrock BLP01-635R-25) before focused and coupled to a single mode fiber optic and conveyed to an avalanche photodiode (APD) (Perkin Elmer SCPM-ARQH-14FC). To provide fluorescence image of the diammond NV sample and control over position on sample a 3-axis piezo nanopositioning (MCL nano-LP 100) is employed. Fig. 4.5 shows a scanning fluorescence image of an area around the middle of the diamond beam (110), the image shows a nearly homogeneous fluorescence counts within 10 $\times$ 10 μm^2 as a results of ensemble of NVs distributed almost homogeneously in the diamond beam.

A microwave generator (Rohde & Schwartz SMB 100A) provide high frequency microwaves for quantum state manipulation. The microwaves delivered to diamond by a gold wire antenna (50 μm in diameter) through a microwave waveguide circuit. For pulsed measurement sequence a high speed multichan-

nel pulse generator (SpinCore Pulse Blaster PBESR-PRO-500) is deployed to provide transitor-transitor logic (TTL) signals to AOM, RF switch (Minicircuit ZYSWA-2-50DR), and APD counter gate. A pair of electromagnet is used to provide in plane external magnetic field to split NV spin degreneracy $|\pm 1\rangle$ into their sublevel manifold and to magnetize magnetic insulator YIG.

4.4 Ferromagnetic Resonance Measurement

Electrical measurement of spin dynamics is performed by using vector network analyzer (VNA) (Rohde & Schwartz ZVB8) through reflection measurement (S_{11}). Under static external magnetic field applied in-plane to the YIG sample, microwave is swept over a frequency range of interest and reflected microwave signal is measured to obtain resonance spectrum of spin waves (Fig. 4.6a). Microwaves are delivered to the sample through one of two gold wire antenna (Fig. 4.6c)depending on the propagation direction of spin wave under investigation.

4.5 Temperature Measurement and Control

To create temperature gradient in YIG two Peltier modules (European Thermodynamics Limited ET-007-05-15) are employed in the experiment. Each Peltier module is sandwiched to two aluminum plates, where bottom side of Peltier modules is thermally connected to a large plate which acts as a room temperature heat bath and the upper side of the Peltier modules each thermally connected to a hot/cold plate. Temperature of both plates are measured by T-type thermocouples connected to a dual-channel nanovoltmeter (Keithley 2182A) which provide feedback signals to control two source-meter instruments (ADCMT 6240A) that feed Peltier modules (Fig. 4.6b). Proportional-integral-derivative (PID) control algorithm is applied to control temperature difference between both ends of YIG.

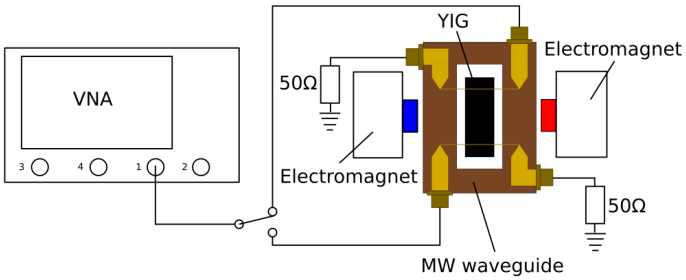

(a)

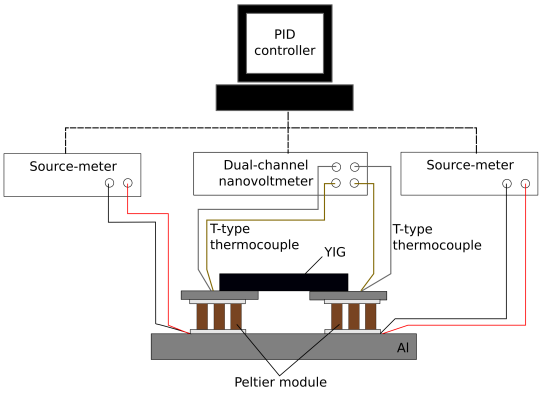

(b)

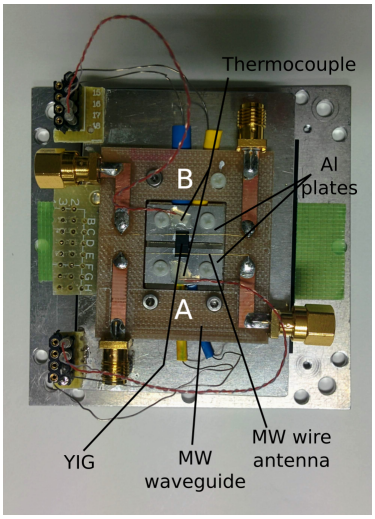

(c)

Figure 4.6: (a) Experimental configuration for ferromagnetic resonance measurement. (b) Experimental configuration of temperature difference measurement and control. (c) Top view photograph of sample stage. A microwave waveguide sends microwave through one of the two gold wire antenna (side A and B). Two Peltier modules sit underneath two aluminum plates and temperature of both plates are measured through two thermocouples attached on them.

Chapter 5

Detection of Thermal Magnon via Nitrogen-Vacancy Electron Spins in Diamond

The utilization of magnon, a quantum state of collective excitation of spins in magnetically ordered media, as a means of transmitting and processing information has been flourished in recent decade and emerged as a new field known as magnon spintronics [5]. Current of thermally induced magnon, thermal magnon current for short, has been experimentally proved to be able to transmit information as far as 40 μm in magnetic insulator media at room temperature [51] and more than 100 μm at 23 K [52]. The experiments were proof-of-principle studies for potential application of 'green' device powered by wasted heat source.

Quantum sensor based on electron spins in diamond (NV centers) has been demonstrated as a high resolution and high sensitivity sensor for various condensed matter phenomena [14]. NV center in diamond is recently known to strongly couple to magnetostatic (long-wavelength) spin waves since their energy exists within a band of frequency of magnetostatic spin waves (several to tens of GHz). It has been demonstrated that NV center is capable of detecting spin wave through resonant and off-resonant excitations [61–63]. Moreover, spin waves can mediate long-range (more than 3 mm) excitation and manipulation of NV center spin state, opening a possibility to develop a hybrid system combining magnon spintronics and quatum system [64, 65].

Thermal magnon, on the other side, sits on a far higher energy region ($\hbar\omega = k_B T$; about 6 THz at room temperature) that does not match to NV spin energy, making it difficult to study using the same technique. Nevertheless, this high energy magnon is known to interact with lesser energy magnon (magnetostatic spin wave) which emanates as a torque that can modify damping torque of the lesser energy magnon [67, 69, 77]. Here we demonstrate indirect detection of thermal magnon via its interaction with magnetostatic spin waves using NV spins in diamond. Pure thermal magnon current is generated by creating temperature gradient in magnetic insulator yttrium iron garnet (YIG) while at the same time magnetostatic spin waves (MSW) is generated through microwave-emitting wire antenna. The thermal magnon current can

modify the dynamics of MSW and correspondingly change stray AC magnetic field around YIG that can be sensed by NV spins. The effect is observed as a change in electron spin resonance (ESR) signal of the NV spin states as well as change in its Rabi frequency.

5.1 Experiment

Experimental setup to detect thermal magnon is illustrated in Fig. 5.1a where YIG/GGG/YIG with dimension of $6 \times 3 \times 0.75$ mm^3 (YIG thickness is 0.1 mm on both sides) is subjected to temperature gradient generated by two Peltier modules placed under both ends of YIG. Temperature at both ends of YIG are measured by T-type thermocouple and controlled by PID (proportional-integral-derivative) controller that regulates the electrical current supply to the two Peltier modules. The two Peltier modules are separated by 1 mm (Fig. 5.1c).

Two gold-wire-antennas that placed at both ends of YIG generate a time-varying magnetic field perpendicular to YIG magnetization, sending magnetostatic spin waves (MSW) to one of two opposite directions on laboratory $\hat{\boldsymbol{z}}$-axis. A pair of electromagnet induces an in-plane bias magnetic field to YIG; parallel to the laboratory $\hat{\boldsymbol{y}}$-axis and co-linear with the gold wires. The geometry resulted in MSW that propagates to $\mathbf{k} \| \mathbf{H} \times \hat{\boldsymbol{n}}$ direction ($\hat{\boldsymbol{n}}$ is vector normal to YIG surface), commonly known as magnetostatic surface spin wave (MSSW) mode [78].

A (110) oriented diamond beam ($2.5 \times 0.1 \times 0.1$ mm^3) with ensemble of NV spins located about 30 nm beneath diamond surface sits on YIG right in the middle of YIG's long dimension. The diamond is placed up-side down so that the surface with shallowly-located NV spins is facing the top surface of YIG. In this configuration two of the four possible NV-axes, $[1\bar{1}\bar{1}]$ (NV1) and $[\bar{1}1\bar{1}]$ (NV2), lay on (110) crystal plane, while two other NV-axes, [111] (NV3) and $[\bar{1}\bar{1}1]$ (NV4) lay on a plane perpendicular to (110) plane (Fig. 5.1b). Bias field is directed in plane to (110) plane and making an angle of about 31.75° to $[00\bar{1}]$ direction (23° to NV1 ($[1\bar{1}\bar{1}]$)) (Fig. 5.1b).

Temperature gradient is created along YIG's long dimension (effective length 1 mm (Fig. 5.1c)) by increasing temperature T_A and decreasing T_B for positive temperature difference ΔT and decreasing T_A and increasing T_B for negative ΔT. With such temperature control the middle of YIG's long dimension where diamond sits can be kept at a constant temperature. Temperature difference ΔT is defined as the difference between temperature at T_A and temperature at T_B ($\Delta T = T_A - T_B$). We calculated the temperature profile of the system under the application of temperature gradient using the finite element method (see Appendix C) and found that due to the high thermal conductivity of the diamond effective temperature gradient that affect the observed phenomenon is only 25 % of the total effective temperature gradient worked in the system.

NV spin states are manipulated and read out via a home-build scanning confocal microscope as described in detail in the previous chapter. The diamond is separated from microwave antenna by about 2 mm (Fig. 5.1c)and

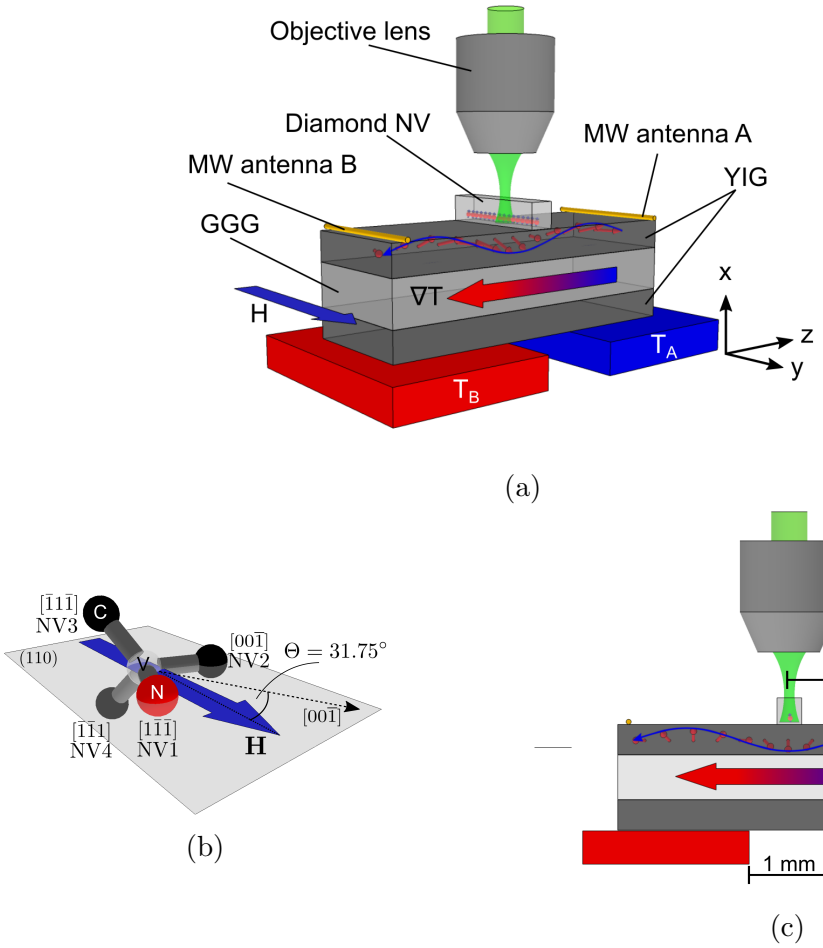

Figure 5.1: (a) YIG is subjected to temperature gradient ∇T by placing its both ends on two Peltier modules separated by 1 mm. Magnetostatic surface spin waves are excited by microwaves through two gold wires (50 μm in diameter). In plane bias magnetic field is subjected to YIG co-linear with gold wire. Diamond with NV centers is placed on top YIG right in the middle of the long dimension of YIG. (b) Two of the four possible NV-axes ($[1\bar{1}\bar{1}]$ (NV1) and $[\bar{1}1\bar{1}]$ (NV2)) lay on (110) plane, while two other NV-axes ([111] (NV3) and $[\bar{1}\bar{1}1]$ (NV4)) lay on a plane perpendicular to (110) plane. Bias magnetic field is applied in plane to (110) plane making an angle of $\Theta = 31.75°$ to $[00\bar{1}]$ direction. (c) Side view of the experimental setup; NV spin states are manipulated by MSSW generated by microwave emitted from gold wire antennas separated 2 mm away from the diamond.

consequently the NV spins are excited dominantly by long-range excitation mediated by MSSW as previously demonstrated by Kikuchi *et al.* [65].

5.2 Results and Discussion

5.2.1 Spin Waves and NV Spins Characterization

We first characterize YIG's global spin wave resonance spectra by performing measurement of microwave reflection (S_{11} parameter) using vector network analyzer at $\Delta T = 0$ K. From the measurement we can map out various spin wave modes that may overlap with resonance frequency of NV spins. As demonstrated by Kikuchi *et al.* [65] and Andrich *et al.* [64], at matched resonance frequency between spin wave f_{SW} and NV spins f_{NV}, NV spins can be excited by a specific spin wave mode from a distant position and get amplified by about 100-fold from direct microwave excitation. From Fig. 5.2 we can see that the spin waves frequency band of interest at room temperature, where overlap between resonant transition of NV spins and spin waves potentially occurred, is within the red and yellow lines that represent the highest ($m_s = +1$) and lowest ($m_s = -1$) Zeeman energy of NV spins and at frequencies above the ferromagnetic resonance (FMR) transition frequency (white dashed line).

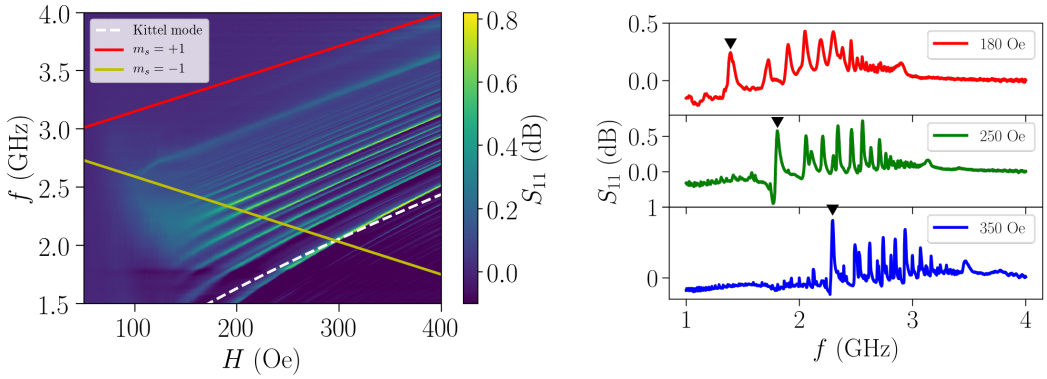

(a) (b)

Figure 5.2: (a) Microwave reflection (S_{11}) spectrum of YIG as a function of applied magnetic field H under microwave power of 1 mW at room temperature. The white dashed line indicates ferromagnetic resonance (Kittel mode) spectrum calculated by Kittel's formula $\gamma_e\sqrt{H(H+4\pi M_s)}$ (with $4\pi M_s = 1488.5$ G extracted from experimental data) and red (yellow) continuous line indicates highest, $m_s = 0 \leftrightarrow +1$, (lowest, $m_s = 0 \leftrightarrow -1$) possible resonant transition of NV spins calculated by $D_{gs} \pm \gamma_e \mathbf{B}\cdot\mathbf{S}$. γ_e and M_s are respectively gyromagnetic ratio of electron and saturation of magnetization of YIG. (b) Spin waves resonance spectrum at 180 Oe, 250 Oe, and 350 Oe. Marked by inverted triangles are the Kittel mode.

To get to know in what frequencies NV spins are effectively excited by specific spin wave mode, optically detected magnetic resonance (ODMR) is performed under varied applied magnetic field at $\Delta T = 0$ K. ODMR is performed by continuously illuminating diamond with laser of 532 nm while sweeping microwaves within the frequency range of NV electron spin resonance. Fig. 5.3a shows a map of resonance transitions of NV spins that overlap with spin wave resonance frequencies (Fig. 5.2a); indicated by the broad and enhanced con-

trast of Lorentzian dips (Fig. 5.3b). Compared to the simulation of NV spins resonance transition frequency as a function of external applied magnetic field (Fig. 5.4), obtained by diagonalizing NV spin Hamiltonian (Eqn. 2.1), only the $m_s = 0 \rightarrow -1$ transition that crossed by spin wave resonance frequencies; resulting in vanishing resonant lines for $m_s = 0 \rightarrow +1$ transition. Moreover, if we zoom in to the NV1 spectral line in Fig. 5.3a as can be seen in Fig. 5.5a and b, we can see a discretized line as a result of resonance matching between NV spin's resonance transition and different spin wave modes (Fig. 5.5e and f). With this we can address a specific spin wave mode.

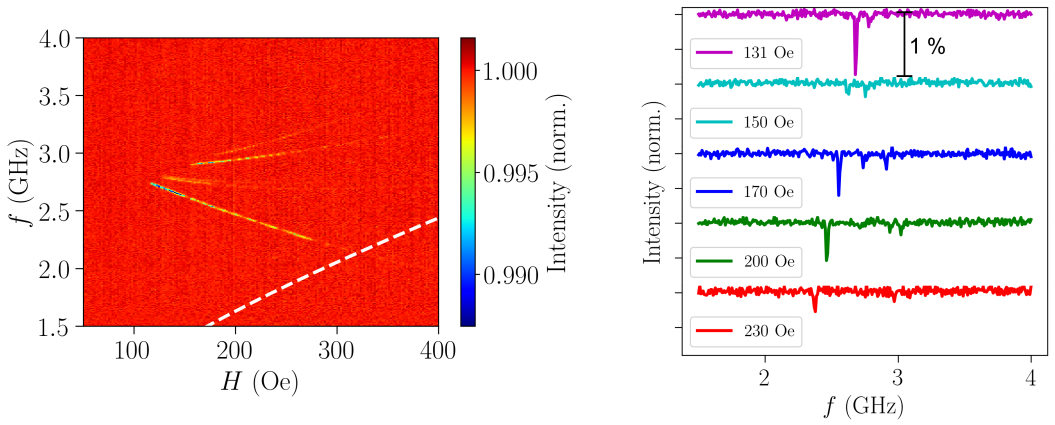

Figure 5.3: (a) Optically detected magnetic resonance spectrum of diamond with NV centers on YIG under 1 mW of microwave power. The contrasting lines shows resonance transitions of NV spins that matched with spin waves resonance, indicating excitation of NV spins by MSSW. The resonant lines clearly appeared within the frequency band of ferromagnetic resonance and spin waves, see Fig. 5.2. (b) Line cuts of ODMR spectrum in (a) at different applied field.

5.2.2 Optically Detected Magnetic Resonance under Temperature Gradient

We detect thermal magnon by how it affects the magnetization dynamics of MSSW, which can be detected by NV spins. We generate thermal magnon current by applying temperature gradient to YIG and examine it using NV-based optical spectroscopy techniques. First, we examine how ODMR spectrum evolves with variation of temperature gradient. We excite spin wave from antenna A and tuned the applied field to $H = 194$ Oe so that resonance dip is observed at matched frequency of $f_{NV} = f_{SW} = 2.580$ GHz. We performed ODMR with varied temperature gradient and examine the contrast of the resonance dip.

Figure 5.6 shows how ODMR spectral dip contrast evolved as temperature difference altered. We observe increasing ODMR contrast as temperature difference moved from 0 K to negative temperature difference regime and decreas-

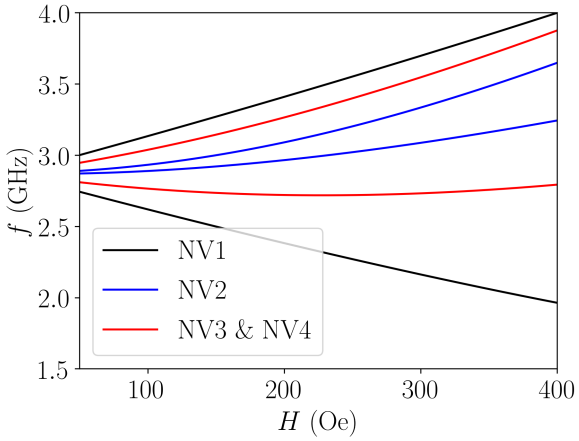

Figure 5.4: Simulation of NV spins resonance transition with external field applied in plane on (110) crystal plane and making angle of about 23° with respect to NV 1 axis ($[1\bar{1}\bar{1}]$). Three upper lines are $m_s = 0 \rightarrow +1$ transition while three bottom lines are $m_s = 0 \rightarrow -1$ transition. After [66]

ing as we switch the temperature difference to positive regime. The observed behavior indicates the influence of applied temperature gradient, which creates thermal magnon current, on the dynamics of spin waves in YIG.

The same behavior is also observed by optically detected spin wave resonance (ODSWR) technique. This technique based on the examination of ODMR contrast (PL constrast) while sweeping external magnetic field. A peak is observed as matching condition between NV spin resonance transition and spin wave resonance is fulfilled. From Fig. 5.7 we can see that the peak grows as temperature difference moved from 0 K to negative temperature difference and shrinks as it moved to positive temperature difference for spin wave excited from antenna A. When we excite spin wave from antenna B opposite behavior is observed; the peak grows as temperature difference moved positively and shrinks as temperature difference moved negatively.

5.2.3 Rabi Nutation under Temperature Gradient

To get better insight on the influence of thermal magnon current on MSSW we drive Rabi nutation between two energy levels of the NV spin ($m_s = 0 \leftrightarrow -1$) with MSSW. This back and forth population transition is known to be sensitive to a change in driving field strength; Rabi oscillation frequency Ω_R is proportional to the square root of driving field power. Since NV spin Rabi oscillation in this case is driven by MSSW, a change in Rabi oscillation frequency Ω_R is an indication of a change in the strength of precessional motion of the MSSW.

We first drive Rabi oscillation through MSSW excited from antenna A and apply temperature gradient to YIG (Fig. 5.8a). In this case, applied field is assigned as $+\mathbf{H}$. We observed that Rabi frequency enhanced or diminished as the direction of temperature gradient is changed. As temperature difference increased from 0 K to positive regime of temperature difference Rabi frequency diminished linearly. Reversing temperature difference to negative regime re-

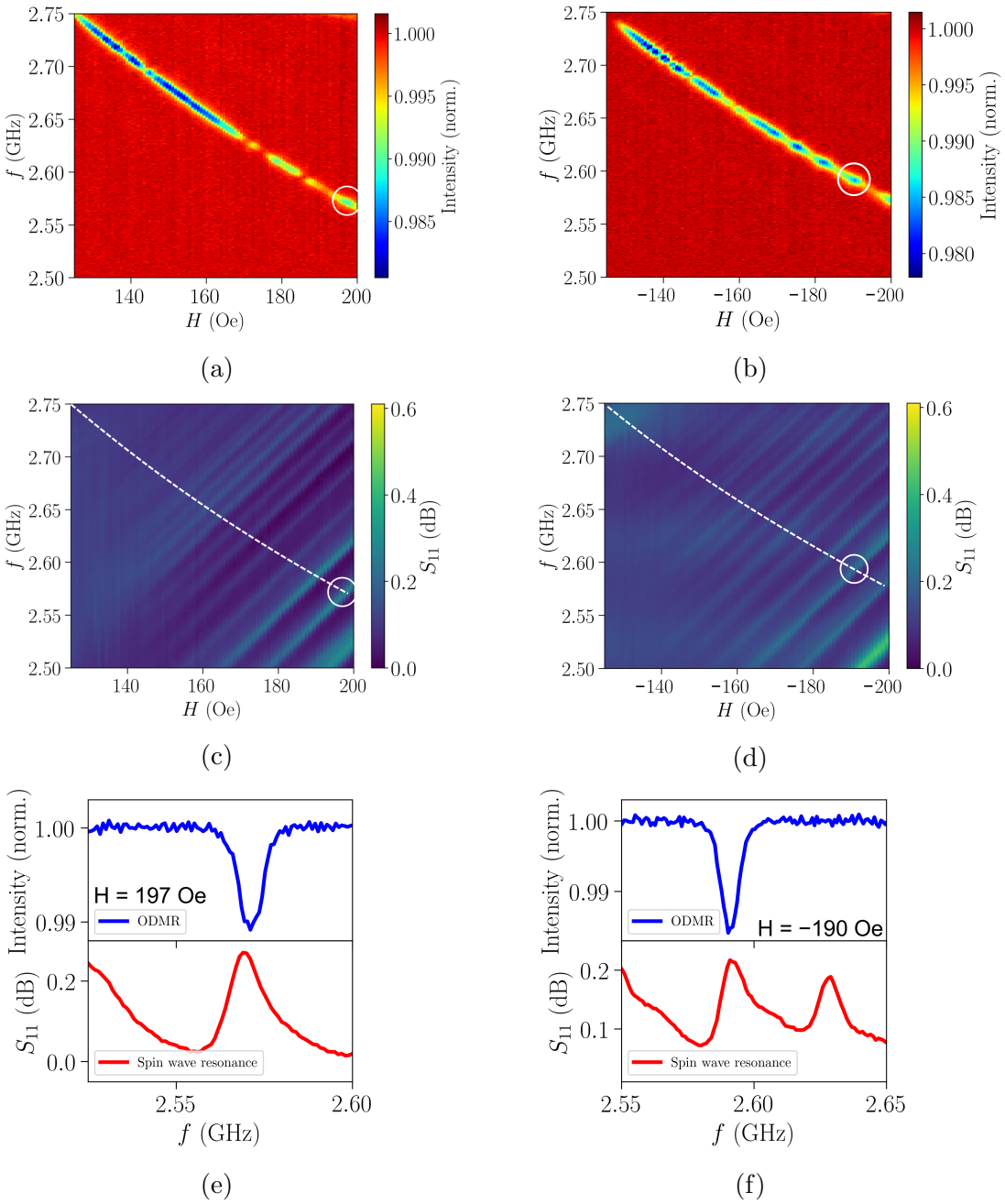

Figure 5.5: Zoomed ODMR spectrum of NV 1 in Fig. 5.3a excited from antenna A (a) and antenna B (b) with microwave power of 1 mW. The spectral line is discretized due to the crossing with different spin wave modes. (c) and (d) are zoomed spin wave spectra of Fig. 5.2a with same frequency band and external field as (a) and (b) respectively. Dashed line indicates ODMR transition frequency line of (a). Circles in (a)-(c) and (b)-(d) indicate correlated spin wave mode. (e) Line cut of (a) (blue line) and (c) (red line) at 197 Oe. (f) Line cut of (b) (blue line) and (d) (red line) at −190 Oe.

sulted in increasing Rabi frequency (Fig. 5.8). AC field strength that drives

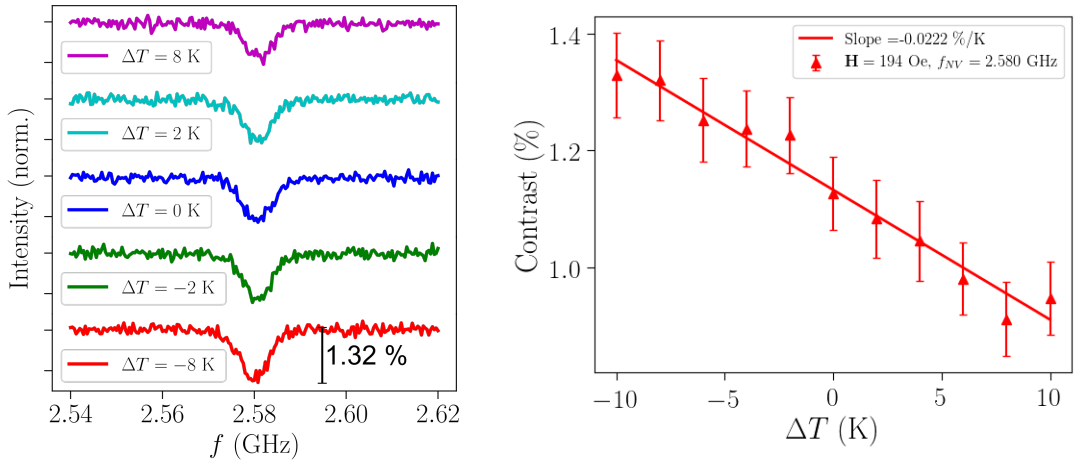

(a) (b)

Figure 5.6: (a) ODMR spectra under various temperature difference at $\mathbf{H} = 194$ Oe. The ODMR contrast dips shrinks as temperature difference ΔT increased. (b) Contrast of ODMR spectra increased as temperature difference moved to negative temperature difference from 0 K and increased as temperature difference moved to negative.

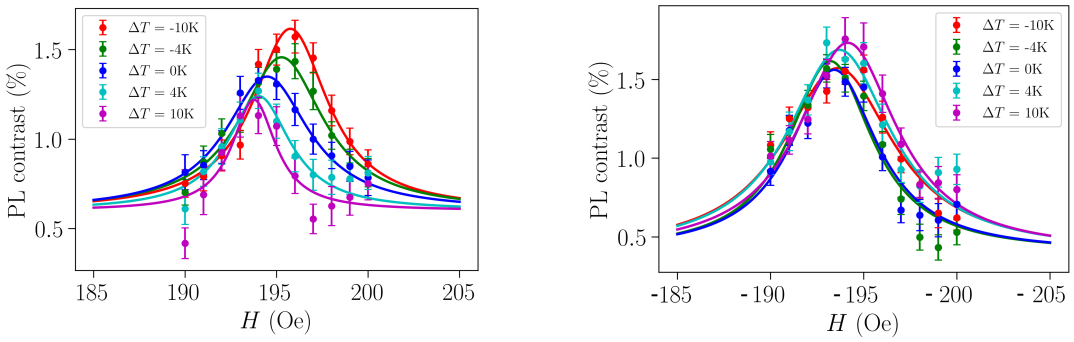

(a) (b)

Figure 5.7: Optically detected spin wave resonance excited from antenna A (a) and B (b) with various applied temperature difference.

the NV spins (Rabi field) can be calculated from Rabi frequency as

$$\mathbf{h}_R = \frac{\Omega_R}{2\pi\gamma_e}. \tag{5.1}$$

Plotted as a function of temperature difference, the Rabi field strength is found to evolves from about 18 μT to 26 μT as temperature difference evolves from 10 K to -10 K (Fig. 5.8d).

MSSW is known to propagate uni-directionally [78], we can expect opposite effect to be observed as we switch the direction of applied field to $-\mathbf{H}$ and drive MSSW from antenna B (Fig. 5.9a). In this configuration we observed opposite effect as compared to $+\mathbf{H}$ configuration. Rabi frequency enhanced as temperature difference increased to positive regime and diminished as temperature difference increased to negative regime. Rabi field in this configuration

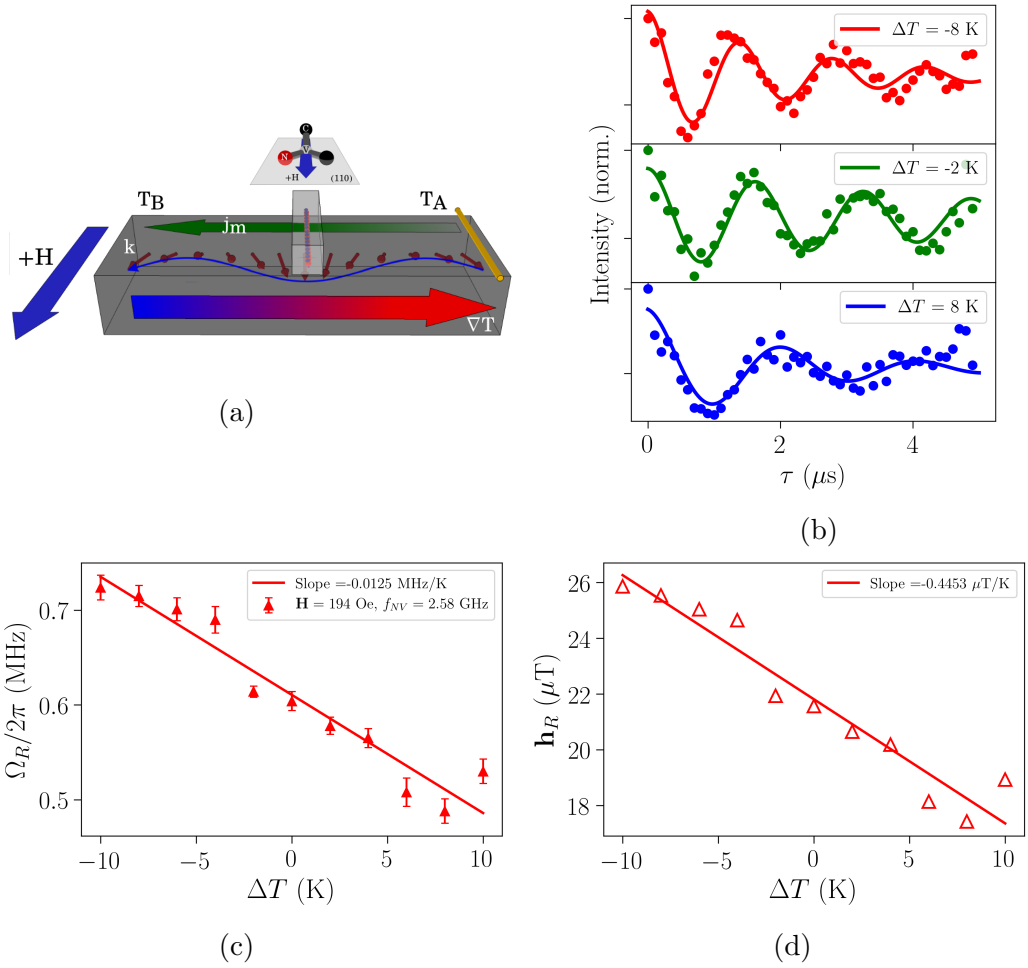

Figure 5.8: (a) Configuration with +**H**; MSSW is excited from antenna A and propagates away from antenna A perpendicular to **H**. (b) Evolution of Rabi oscillation as temperature difference changed. In this configuration Rabi frequency enhances as temperature difference grows negatively while diminishes as temperature difference increased to positively(c). Microwave power of 2 mW is used to excite spin wave. (d) Calculated Rabi field strength $\mathbf{h}_R$ as a function of temperature difference.

is found to evolve from about 18 μT at -10 K to about 22 μT at 10 K (Fig. 5.9d).

We can interpret the observed effects in terms of thermal magnon current induced by temperature gradient as recently demonstrated by Giles *et al.* and Shan *et al.* [52–54]. This thermal magnon current interacts with MSSW and emanated as an additional torque that changes the precessional motion of MSSW [68–70] (see Fig. 5.10). We observed that when thermal magnon current $\mathbf{j}_m$, which flows from higher temperature to lower temperature [54], flows in the opposite direction as MSSW's **k** wave vector, additional magnetic torque grows and coping damping torque that tends to relax precessional motion back to its equilibrium co-linear with effective field. As a result, angle of precessional motion increased and sensed by NV spins as a stronger Rabi driving field (Fig. 5.11 (top)). On the contrary, when $\mathbf{j}_m$ is directing the same

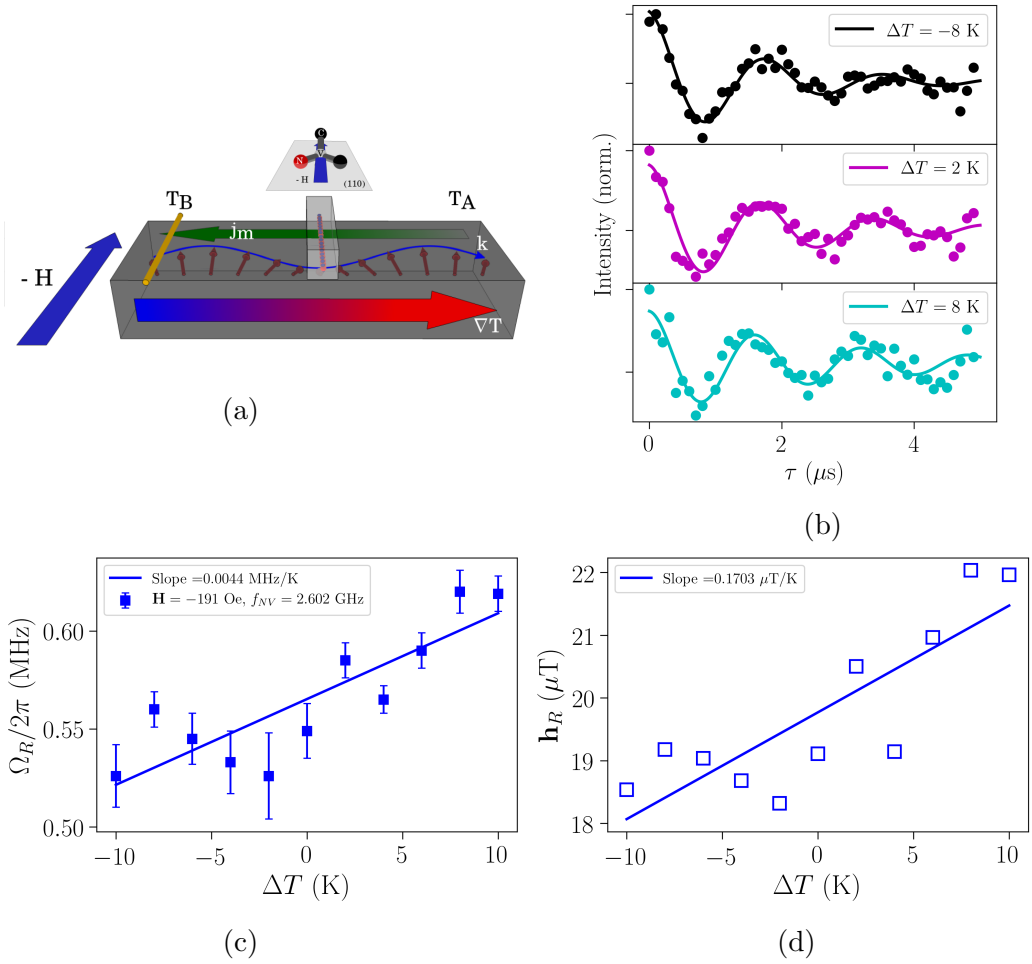

Figure 5.9: (a) Configuration with $-\mathbf{H}$; MSSW is excited from antenna B and propagates away perpendicular to $\mathbf{H}$. (b) As MSSW excitation is switched, Rabi oscillation frequency evolves oppositely; enhancing as temperature difference increased positively and diminishing as temperature difference increased negatively. (d) Calculated Rabi field strength $\mathbf{h}_R$ as a function of temperature difference.

direction as $\mathbf{k}$, additional torque shrinks and angle of precessional motion decreased (Fig. 5.11 (bottom)). It is sensed by NV spins as a weaker Rabi driving field. The same effect holds as we switch the MSSW excitation either from antenna A or antenna B.

5.2.4 Electrical Measurement

As demonstrated recently by Yu *et al.* [69], the same effect can be observed by electrical measurement through the examination of spin wave resonance linewidth of transmitted microwave signal. We confirm the results obtained from the optical measurement by electrical measurement done by examining spin wave resonance linewidth of microwave signal reflected by YIG (S_{11} parameter). This resonance linewidth is known to be proportional to damping parameter α in the phenomenological Landau-Lifshitz-Gilbert equation of

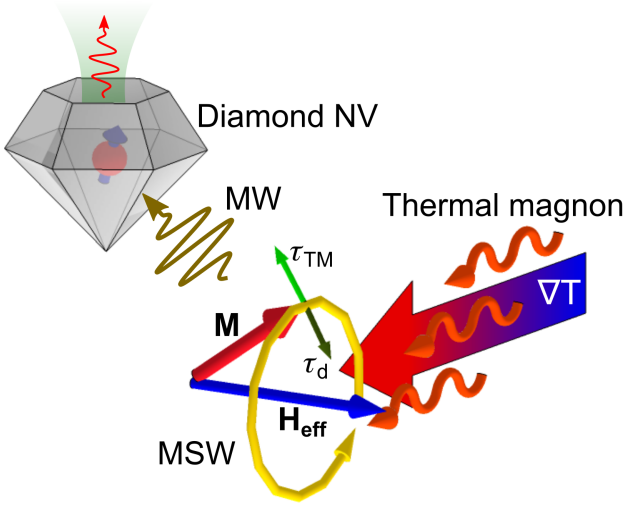

Figure 5.10: Illustration of the mechanism of thermal magnon detection by NV center in diamond. Thermal magnon current, generated by temperature gradient, interacts with magnetostatic spin wave (MSW), affecting the precessional motion of MSW and change microwave (MW) field sensed by NV spin.

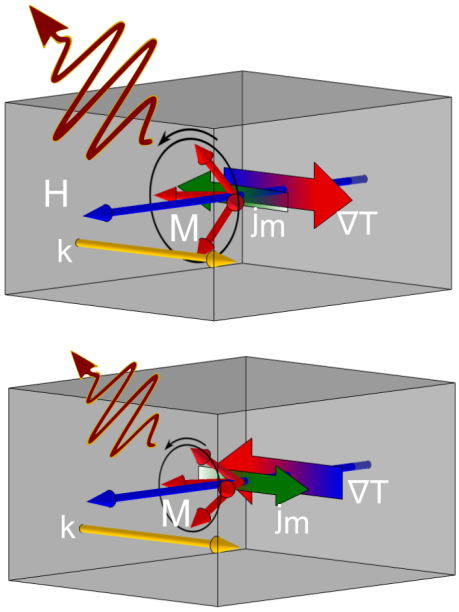

Figure 5.11: Magnetization precessional cone angle changed with the reversal of temperature gradient; getting large when thermal magnon current $\mathbf{j}_m$ and MSSW $\mathbf{k}$ directing the opposite direction (top) and getting small with $\mathbf{j}_m$ and $\mathbf{k}$ directing same direction (bottom).

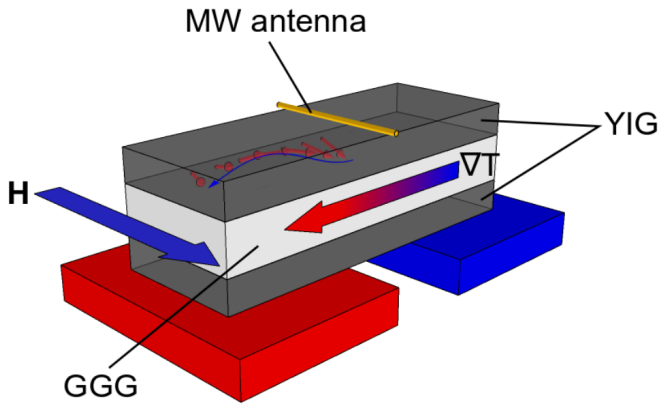

Figure 5.12: Experiment configuration for electrical measurement. Microwave antenna is palced at the center of YIG's long dimension.

magnetization motion (Eqn. 3.31) [43];

$$\Delta f = \Delta f_0 + \frac{2}{\sqrt{3}}\alpha\frac{\omega}{2\pi}, \tag{5.2}$$

with Δf_0 is inhomogenous linewidth and ω is microwave frequency.

To make sure that the electrical measurement represents as close as the condition of optical measurement, we move the antenna to the center of YIG long dimension (Fig. 5.12). We found a good correlation between electrical measurements and optical measurements. For $+\mathbf{H}$ configuration, resonance linewidth Δf broadens as temperature difference increased from 0 K to positive regime and become narrow as temperature difference increased to negative regime from 0 K (Fig. 5.13). Oppositely, for $-\mathbf{H}$ configuration the resonance linewidth broadens as temperature difference moved from 0 K to negative temperature difference regime and narrowing as temperature difference moves to higher value in positive regime (Fig. 5.14). Broader resonance linewidth indicates higher damping parameter, which means a smaller angle of magnetization precessional motion. Oppositely, more narrow resonance linewidth indicates higher angle of precessional motion.

5.2.5 Phenomenological Explanation and Estimation of Damping Parameter

The observed phenomena can be explained by phenomenological Landau-Lifshitz-Gilbert (LLG) equation of magnetization motion plus additional term that corresponds to the torque induced by thermal magnon current [69]

$$\frac{d\mathbf{M}}{dt} = \gamma_e\mu_0(\mathbf{M}\times\mathbf{H}_{\text{eff}}) + \frac{\alpha}{M_s}\left(\mathbf{M}\times\frac{d\mathbf{M}}{dt}\right) + \gamma_e\boldsymbol{\tau}_{\text{tm}}, \tag{5.3}$$

where $\boldsymbol{\tau}_{\text{tm}}$ is torque induced by thermal magnon current. Following the treatment of LLG under thermal magnon torque by Yu *et al.* [69] and adapted to our system, thermal magnon torque is given by

$$\boldsymbol{\tau}_{\text{tm}} = \alpha_{\text{tm}}\frac{\omega}{|\gamma_e|M_s^2}\mathbf{M}\times(\mathbf{M}\times\mathbf{m}_k), \tag{5.4}$$

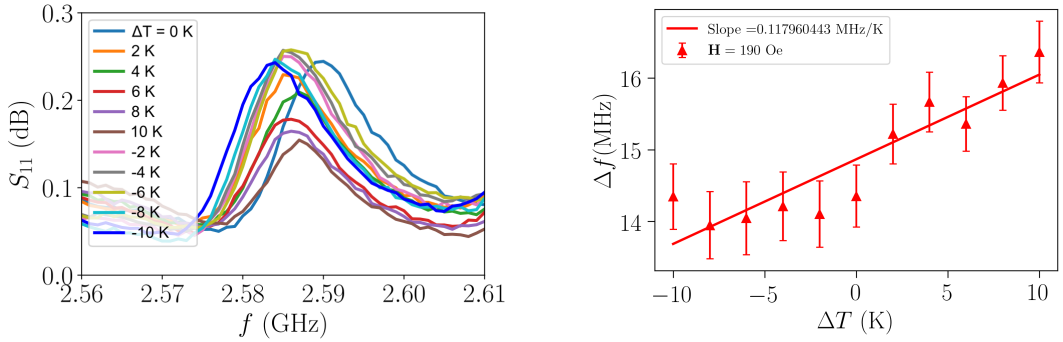

(a) (b)

Figure 5.13: (a) A set of spin wave resonance spectrum under various temperature difference in $+\mathbf{H}$ configuration. (b) Resonance linewidth Δf as a fucntion of temperature difference for $+\mathbf{H}$.

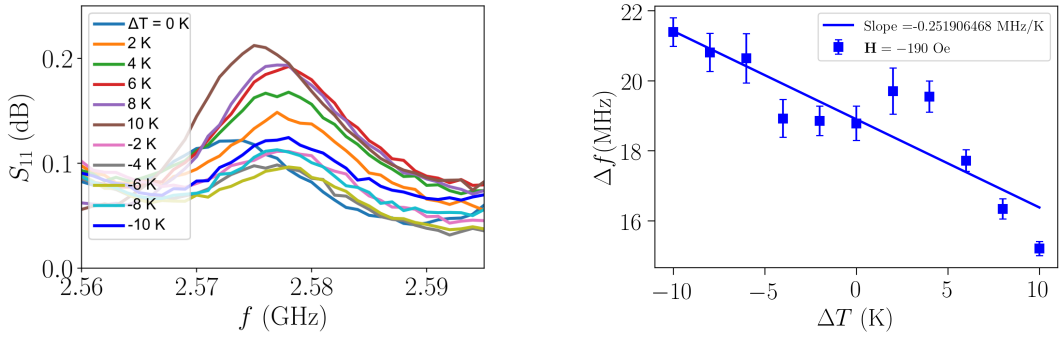

(a) (b)

Figure 5.14: (a) A set of spin wave resonance spectrum under various temperature difference in $-\mathbf{H}$ configuration. (b) Resonance linewidth Δf as a fucntion of temperature difference for $-\mathbf{H}$.

where α_{tm}, ω, and $\mathbf{m}_k$ are thermal magnon torque damping parameter, resonance frequency, and non-equilibrium component of magnetization for mode k, respectively. The damping parameter of thermal magnon torque is given by

$$\alpha_{\text{tm}} = \frac{\omega_M}{\omega}\frac{k_T}{k}, \tag{5.5}$$

where $\omega_M = -\gamma_e \mu_0 M_s$ and k_T is thermal wave vector which given by

$$\mathbf{k}_T = -\left(\frac{\omega + \omega_0}{\omega_M}\right)\left|\frac{1}{M_s}\frac{dM_s}{dT}\right|\nabla T. \tag{5.6}$$

Here, $\omega_0 = -\gamma_e H_0$. Equation 5.5 can explain data in Fig. 5.13 and 5.14 in which when thermal wave vector directing the same direction as MSSW wave vector k, thermal magnon torque damping parameter decreased and increased as they directing oppositely.

The change in resonance linewidth under the application of temperature gradient as observed in electrical measurement (Fig. 5.13b and 5.14b) can be used to estimate damping parameter of thermal magnon torque. Considering

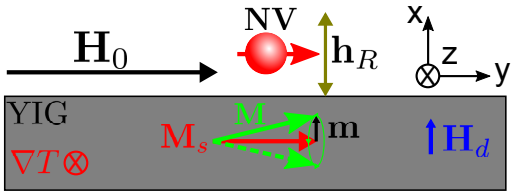

Figure 5.15: Toy model of a system with NV spin (red spin) and magnetization precession in YIG (green arrow). Magnetization precession produces AC magnetic field ($\mathbf{h}_R$) that drives the NV spin into its Rabi oscillation.

that the effective damping parameter of the system is the sum of intrinsic damping parameter of YIG and damping parameter of the thermal magnon torque ($\alpha_{\text{eff}} = \alpha + \alpha_{\text{tm}}$), resonance linewidth given by Eqn. 5.2 can be rewritten as

$$\Delta f = \Delta f_0 + \frac{2}{\sqrt{3}}\alpha\left|\frac{\omega_K}{2\pi}\right| - \frac{2}{\sqrt{3}}\left|\frac{\omega_K + \omega_0}{2\pi}\right|\left|\frac{1}{M_s}\frac{dM_s}{dT}\right|\frac{1}{k}\nabla T, \tag{5.7}$$

where $\omega_K = \pm\sqrt{\omega_0(\omega_0 + \omega_M)}$ is Kittel resonance frequency. From data fit using Eqn. 5.7, damping parameter of thermal magnon torque is estimated to be 3.9456×10^{-4} at $\Delta T = 2.5$ K for positive applied external magnetic field and 4.23×10^{-4} at $\Delta T = 2.5$ K for negative applied external magnetic field. This value is in the same order as other reported data on the same phenomenon [69–73].

Table 5.1: Comparison of damping parameter of thermal magnon torque

No.		$\alpha_{\text{tm}}(\times 10^{-4})$	ΔT (K)
1.	This work	3.94	2.5
2.	H. Yu *et al.* PRB (2017) [69]	~ 3.15	28
3.	Y. Kajiwara *et al.* APL (2013) [70]	7.5	14.5
4.	L. Liu *et al.* PRL (2012) [71]	0.83	20
5.	J. Holanda *et al.* PRB (2017) [72]	0.374	10
6.	M. B. Jungfleisch *et al.* APL (2013) [73]	0.0446	10

Equation 5.4 can be expressed in terms of thermal magnon current as

$$\boldsymbol{\tau}_{\text{tm}} = \frac{k_T}{M_s^2}\mathbf{M} \times (\mathbf{M} \times \mathbf{j}_m) \tag{5.8}$$

with thermal magnon current

$$\mathbf{j}_m = \frac{\mu_0 M_s}{k}\mathbf{m}_k. \tag{5.9}$$

This equation is consistent with our previous interpretation that when thermal magnon current $\mathbf{j}_m$ flows in the same direction as $\mathbf{k}$ wave vector torque is built and as consequences enhances Rabi driving field.

Damping parameter of thermal magnon torque can also be estimated from the Rabi field as a function of temperature gradient (Fig. 5.8d and Fig. 5.9d)

through micro magnetic approach where oscillating magnetization generates oscillating magnetic field that drives NV spin into its Rabi oscillation (Fig. 5.15). From the toy model in Fig. 5.15, effective field of the system is given by

$$\mathbf{H}_{\text{eff}} = \mathbf{H}_0 + \mathbf{h}_R + \mathbf{H}_d, \tag{5.10}$$

where $\mathbf{H}_0$, and $\mathbf{h}_R$ are respectively external field, Rabi field, and $\mathbf{H}_d$ is demagnetization field which equal to $-\mu_0\mathbf{M}_{\text{eff}}$. This effective field produces effective magnetization in YIG which is given by

$$\mathbf{M}_{\text{eff}} = \mathbf{M}_s + \mathbf{m}, \tag{5.11}$$

where $\mathbf{M}$ is saturation magnetization and $\mathbf{m}$ is transverse component of magnetization precession. Given that the precession cone angle of magnetostatic spin wave is small ($< 1°$) [74], Eqn. 5.11 can be truncated into $\mathbf{M}_{\text{eff}} = \mathbf{M}_s$.

Magnetic damping parameter is related to the imaginary part of dynamic susceptibility [75]

$$\chi'' = \frac{\alpha_{\text{eff}}\omega_r\omega_M[\omega_0^2 + \omega_r^2(1+\alpha_{\text{eff}}^2)]}{[\omega_0^2 - \omega_r^2(1+\alpha_{\text{eff}}^2)]^2 + 4\omega_0^2\omega_r^2\alpha_{\text{eff}}^2}, \tag{5.12}$$

where ω_r is spin wave resonance angular frequency $\omega_0 = -\gamma_e H_0$, $\omega_M = -\gamma_e\mu_0 M_s$, and α_{eff} is effective damping parameter. Under a resonance condition ($\omega_r = \omega_0$) and considering that damping parameter α_{eff} is a small value so that $1 + \alpha_{\text{eff}} \simeq 1$, the imaginary part of dynamic susceptibility is reduced to

$$\chi_r'' = \frac{\omega_M}{2\alpha_{\text{eff}}\omega_r}. \tag{5.13}$$

Since our measurement of Rabi frequency as a function of temperature difference is done with the NV spin frequency matched to the spin wave resonance frequency ($f_{NV} = f_{SW}$) (Fig. 5.5e and 5.5f), we can use Eqn. 5.13 to find the relation between Rabi field $\mathbf{h}_R$ and damping parameter α_{eff} by substituting Eqn. 5.10 and 5.11 into Eqn. 5.13

$$\mathbf{h}_R = -\alpha_{\text{eff}}\frac{\omega_r}{2\pi\gamma_e} - \mathbf{H}_0 + \mu_0\mathbf{M}_s. \tag{5.14}$$

With α_{eff} is composed of intrinsic damping parameter α_i and damping parameter from the thermal magnon torque α_{tm} which is a function of temperature gradient ($\alpha_{\text{tm}} = a\nabla T$), Eqn. 5.14 can be rewritten as

$$\mathbf{h}_R = -\alpha_i\frac{\omega_r}{2\pi\gamma_e} - a\frac{\omega_r}{2\pi\gamma_e}\nabla T - \mathbf{H}_0 + \mu_0\mathbf{M}_s. \tag{5.15}$$

From the slope of Rabi field as a function of temperature difference (Fig. 5.8d and 5.9d), we can obtain proportionality constant a and estimate the damping parameter from the thermal magnon torque α_{tm} as 5.158×10^{-4} for $+\mathbf{H}$ and 0.576×10^{-4} for $-\mathbf{H}$ at effective temperature difference of $\Delta T = 2.5$ K. These values of damping parameter from thermal magnon torque are in a good agreement with those obtained from the electrical measurement which supports our interpretation that the modulation of Rabi frequency by temperature gradient is due to the thermal magnon current that induces additional torque to MSSW.

5.3 Conclusion

In conclusion, we demonstrated detection of thermal magnon current through its interaction with MSSW that can be sensed by quantum sensor based on electron spins in diamond with nitrogen-vacancy defect. Thermal magnon current generated under the application of temperature gradient in magnetic insulator YIG emanates as a torque that modifies MSSW's dynamics. This modification in magnetization dynamics is sensed by the NV spins as an oscillating field that drives NV spins to their Rabi transition. The Rabi frequency of the NV spins enhances or diminishes as we switch the direction of the thermal magnon. The observed effect also demonstrates control over magnetostatic spin wave by thermal means. The use of quantum sensor based on electron spin in diamond with NV defect to investigate thermal magnon current opens new possibilities to study the interplay between thermal magnon and magnetostatic spin wave, which is still rarely explored [67, 69, 76, 77], in an unprecedented way; leaving a room for new understanding and practical applications.

Chapter 6

Summary and Outlook

6.1 Summary

This dissertation is focused on the development of a measurement technique for investigating thermally induced magnon using quantum sensor based on electron spins ($S = 1$) in diamond with nitrogen-vacancy defect. For this we create nitrogen-vacancy defects in diamond (oriented in [110] direction) by implanting $^{14}N^{+}$ ions to the diamond. By simulation, we found that the nitrogen-vacancy centers are formed at the depth of about 30 nm from the surface of diamond. The electron spin in diamond NV center can be manipulated with microwave and detected optically through its spin-selective fluorescence. To manipulate and detect the electron spin in diamond NV center we build a scanning confocal microscope equipped with microwave generator.

We use yttrium iron garnet (YIG) as a sample material to investigate thermally induced magnon. YIG is an ideal system to study pure magnon due to its insulating characteristic. It was recently demonstrated that thermally induced magnon can flow as magnon current under non-equilibrium condition such as gradient of magnon chemical potential $\nabla\mu_m$ and temperature gradient ∇T. Furthermore, this current of thermal magnon is known to interact with magnetostatic spin wave. Since the energy of thermally induced magnon is far away from the energy of NV spins we can not expect a direct interaction between them. We exploit magnetostatic spin wave which can resonantly interact with NV spin as a mediator to detect thermally induced magnon.

We excite magnetostatic surface spin wave (MSSW) in YIG and put it under temperature gradient. Diamond with NV centers is placed on top of YIG and used as a magnetometer to detect the dynamics of magnetization in YIG. By examining the magnetization dynamics of magnetostatic surface spin wave (MSSW) in YIG under temperature gradient, we can indirectly detect the existence of thermal magnon. We observed a change in optically detected magnetic resonance (ODMR) signal of the NV spins as we vary temperature gradient in YIG. The ODMR signals intensify or diminish as we vary and reverse temperature gradient in YIG. A sign that temperature gradient affected the magnetization dynamics in YIG. Moreover, Rabi nutation of the NV spin, which is a back and forth population transition between two level energies of the NV spin ($m_s = 0 \leftrightarrow 1$), is also found to be changed under the application of

temperature gradient in YIG. The Rabi oscillation frequency, which indicates the strength of the oscillation's driving field, is found to be enhanced or diminished with the application of temperature difference in YIG. We interpret this effect as thermal magnon current that acts on the magnetization dynamics as an additional torque that induces modification of magnetostatic surface spin wave's dynamics. We found an intensification of MSSW's dynamical motion when thermal magnon current flow in the opposite direction as MSSW's wave vector and a lessening as thermal magnon current flow in the same direction as MSSW's wave vector.

6.2 Outlook

The effect observed with our measurement technique is a first step towards a better understanding of thermally excited magnon in magnetically ordered system. The understanding of the dynamics of thermally excited magnon is still in its infancy, researchers are begining to aware its physics and how they can harness it for useful application several years back [7, 50–54]. With the technique described in this dissertation we expect a better insight on the understanding of the thermally excited magnon and how it interacts with environment will spawn in the near future. For instance, researchers recently began to explore how thermal magnon and coherent magnetostatic spin wave interact each other [68, 69, 76, 77]. With our technique we can study how various modes of magnetostatic spin wave will interact with the current of thermal magnon.

One of the advantage of using electron spin in diamond with NV defect as a sensor is that it can be miniaturize down to nanometer. By performing the same technique with nanometer-sized diamond we can explore the dynamics of thermal magnon in nanoscale. We can expect a study on how magnetic domain wall interact with thermal magnon current as proposed recently by Flebus *et al.* [68] or how anisotropy in magnetic material affected thermal magnon. Rooms for exploration are widely open with this technique and we anticipate unprecedented useful technological application will emerge from better understanding of the phenomena related to thermal magnon, in particular technology for better management of energy.

Appendix A

Derivation of Phenomenological Equation

To obtain equation for thermal magnon torque given in Eqn. 5.4 we follow derivation of Landau-Lifshitz-Gilbert (LLG) equation under an applied temperature gradient ∇T given by Yu *et al.* [69] which contains additional term related to thermal magnon torque [79]

$$\dot{\boldsymbol{M}} = \gamma_e \mathbf{M} \times \mathbf{H}_{\text{eff}} + \frac{\alpha}{M_s} \mathbf{M} \times \dot{\boldsymbol{M}} + \gamma_e \mathbf{M} \times \mathbf{H}_{\text{TMT}} \tag{A.1}$$

where $\mathbf{H}_{\text{eff}}$, $\mathbf{H}_{\text{TMT}}$, α, and M_s are respectively effective magnetic field, magnetic field induced by temperature gradient, damping parameter and saturation magnetic field. The effective magnetic field $\mathbf{H}_{\text{eff}}$ is composed of external field $\mathbf{H}_0$, demagnetization field $\mathbf{H}_{\text{dem}}$, anisotropy field $\mathbf{H}_{\text{ani}}$, and microwave excitation field $\mathbf{h}$. For the analysis of thermal magnon torque we neglect anisotropy and demagnetization field is given by

$$\mathbf{H}_{\text{dem}} = -\mu_0 (\mathbf{M} \cdot \hat{\boldsymbol{x}}) \hat{\boldsymbol{x}}. \tag{A.2}$$

Magnetization $\mathbf{M}$ is the sum of saturation magnetization $\mathbf{M}_s$ and magnetic response field $\mathbf{m}$ oscillating in $\hat{\boldsymbol{x}}$-$\hat{\boldsymbol{z}}$ plane (Fig. A.1)

Linearizing Eqn. A.1 gives

$$\dot{\boldsymbol{m}} = \gamma_e (\mathbf{M}_s \times \mathbf{h} + \mathbf{m} \times \mathbf{H}_0) - \gamma_e \mu_0 (\mathbf{m} \cdot \hat{\boldsymbol{x}})(\mathbf{M}_s \times \hat{\boldsymbol{x}}) + \frac{\alpha}{M_s} \mathbf{M}_s \times \dot{\boldsymbol{m}} + \gamma_e \mathbf{M}_s \times \mathbf{H}_{TMT}. \tag{A.3}$$

With magnetic field induced by temperature gradient given by Brechet *et al.* [79]

$$\mathbf{H}_{\text{TMT}} = \mu_0 (\mathbf{k}_T \cdot \nabla^{-1}) \mathbf{m}, \tag{A.4}$$

with $\mathbf{k}_T = -\frac{1}{\chi^2} \frac{\partial \chi}{\partial T} \nabla T$ is thermal wave vector which propagates along $\hat{\boldsymbol{z}}$-axis (Fig. A.1), LLG equation can be rewritten as

$$\dot{\boldsymbol{m}} = \gamma_e (\mathbf{M}_s \times \mathbf{h} + \mathbf{m} \times \mathbf{H}_0) - \gamma_e \mu_0 M_s (\mathbf{m} \cdot \hat{\boldsymbol{x}}) \hat{\boldsymbol{z}} + \frac{\alpha}{M_s} \mathbf{M}_s \times \dot{\boldsymbol{m}} + \gamma_e \mu_0 \mathbf{M}_s \times (\mathbf{k}_T \cdot \nabla^{-1}) \mathbf{m}. \tag{A.5}$$

External field $\mathbf{H}_0$ and saturation magnetization $\mathbf{M}_s$ are oriented in $\hat{\boldsymbol{y}}$-axis

$$\mathbf{H}_0 = -H_0 \hat{\boldsymbol{y}}, \;\; \mathbf{M}_s = -M_s \hat{\boldsymbol{y}}. \tag{A.6}$$

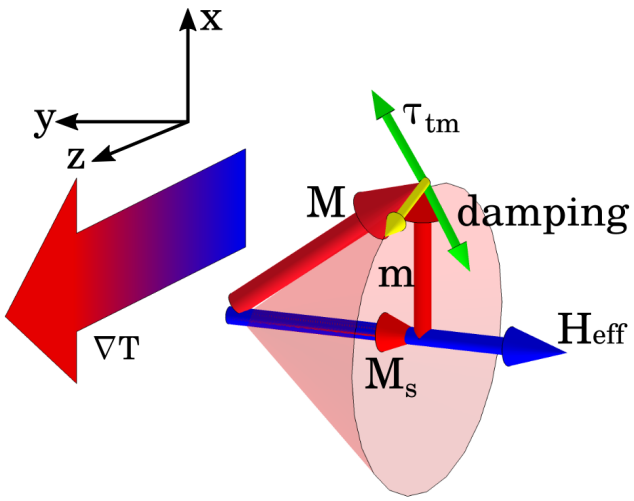

Figure A.1: Illustration of Landau-Lifshitz-Gilbert phenomenological magnetization precessional motion under temperature gradient.

thermal wave vector $\mathbf{k}_T$ is directing along $\hat{\boldsymbol{z}}$

$$\mathbf{k}_T = k_T \hat{\boldsymbol{z}}. \tag{A.7}$$

Magnetic field excitation field $\mathbf{h}$ and magnetic response field $\mathbf{m}$ are precessing in a plane orthogonal to $\mathbf{H}_0$

$$\mathbf{h} = h_x \hat{\boldsymbol{x}} + h_z \hat{\boldsymbol{z}}, \quad \mathbf{m} = m_x \hat{\boldsymbol{x}} + m_z \hat{\boldsymbol{z}}. \tag{A.8}$$

Angular frequencies ω_0 and ω_M are respectively given by

$$\omega_0 = -\gamma_e H_0 > 0 \ \text{ and } \ \omega_M = -\gamma_e \mu_0 M_s > 0. \tag{A.9}$$

With $\gamma_e < 0$, LLG is rewritten as

$$\dot{\boldsymbol{m}} = \omega_0(\hat{\boldsymbol{y}} \times \mathbf{m}) - \frac{\omega_M}{\mu_0}(\hat{\boldsymbol{y}} \times \mathbf{h}) - \omega_M(\mathbf{m} \cdot \hat{\boldsymbol{x}})\hat{\boldsymbol{z}} - \alpha(\hat{\boldsymbol{y}} \times \dot{\boldsymbol{m}}) - \omega_M \hat{\boldsymbol{y}} \times (\mathbf{k}_T \cdot \nabla^{-1})\mathbf{m}. \tag{A.10}$$

With spin waves propagates along $\hat{\boldsymbol{z}}$-axis (Fig. A.1), time evolution of magnetic field response is given by

$$\dot{\boldsymbol{m}} = \omega(-\hat{\boldsymbol{y}} \times \mathbf{m}) \tag{A.11}$$

and magnetic response expanded in plane wave vector $\mathbf{k}$ is given by

$$\mathbf{m} = \sum_k \mathbf{m}_k = \sum_k [m_{kx} \cos(\omega t + kz + \phi)\hat{\boldsymbol{x}} + m_{kz} \sin(\omega t + kz + \phi)\hat{\boldsymbol{z}}]. \tag{A.12}$$

Following plane wave expansion, time evolution of the magnetic response field is given by

$$\dot{\boldsymbol{m}} = \sum_k \omega(-\hat{\boldsymbol{y}} \times \mathbf{m}_k). \tag{A.13}$$

In order to rewrite the last term in LLG equation in the form of Gilbert damping, operational identity $\nabla^{-1}\cdot\nabla = \mathbf{1}$ is applied along $\hat{\boldsymbol{z}}$-axis on the vector $\sum_k \frac{1}{k}(-\hat{\boldsymbol{y}}\times\mathbf{m}_k)$

$$\mathbf{k}_T\cdot\nabla^{-1}\left(-\hat{\boldsymbol{y}}\cdot\nabla\left(\sum_k\frac{1}{k}(-\hat{\boldsymbol{y}}\times\mathbf{m}_k)\right)\right) = \sum_k\frac{k_T}{k}(-\hat{\boldsymbol{y}}\times\mathbf{m}_k). \tag{A.14}$$

Recalling Eqn. A.12 we get

$$-\hat{\boldsymbol{y}}\cdot\nabla\left(\frac{1}{k}(-\hat{\boldsymbol{y}}\times\mathbf{m}_k)\right) = -\hat{\boldsymbol{y}}\cdot\nabla\left(-m_{kz}\frac{\sin(\omega t+kz+\phi)}{k}\hat{\boldsymbol{x}} + m_{kx}\frac{\cos(\omega t+kz+\phi)}{k}\hat{\boldsymbol{z}}\right) \tag{A.15}$$

$$= m_{kx}\cos(\omega t+kz+\phi)\hat{\boldsymbol{x}} + m_{kz}\sin(\omega t+kz+\phi)\hat{\boldsymbol{z}} \tag{A.16}$$

$$= \mathbf{m}_k. \tag{A.17}$$

Hence, the last term of LLG is expressed as

$$(\mathbf{k}_T\cdot\nabla^{-1})\mathbf{m} = \sum_k\frac{k_T}{k}(-\hat{\boldsymbol{y}}\times\mathbf{m}_k). \tag{A.18}$$

From the last form of the LLG equation (Eqn. A.10) we can rewrite it as

$$\dot{\boldsymbol{m}} = \omega_0(\hat{\boldsymbol{y}}\times\mathbf{m}) - \frac{\omega_M}{\mu_0}(\hat{\boldsymbol{y}}\times\mathbf{h}) - \omega_M(\mathbf{m}\cdot\hat{\boldsymbol{x}})\hat{\boldsymbol{z}} - \left[\alpha + \frac{\omega_M}{\omega}\frac{k_T}{k}\right](\hat{\boldsymbol{y}}\times\dot{\boldsymbol{m}}). \tag{A.19}$$

Effective damping term is given by the sum of Gilbert damping term α and damping from thermal magnon torque α_{tm},

$$\alpha_{\mathrm{eff}} = \alpha + \alpha_{\mathrm{tm}}, \tag{A.20}$$

which from Eqn. A.19 is given by

$$\alpha_{\mathrm{tm}} = \frac{\omega_M}{\omega}\frac{k_T}{k}. \tag{A.21}$$

To express thermal magnon damping torque as a function of temperature gradient we recall thermal wave vector that is given by

$$\mathbf{k}_T = -\frac{1}{\chi^2}\frac{\partial\chi}{\partial T}\nabla T. \tag{A.22}$$

Magnetic susceptibility χ is obtained by solving LLG equation A.10 using the relations A.13 and A.18 for a given k

$$(-\omega-\omega_0)(\hat{\boldsymbol{y}}\times\mathbf{m}_k)+\omega_M(\mathbf{m}_k\cdot\hat{\boldsymbol{x}})\hat{\boldsymbol{z}}-\alpha_{\mathrm{eff}}\omega\hat{\boldsymbol{y}}\times(\hat{\boldsymbol{y}}\times\mathbf{m}_k) = -\frac{\omega_M}{\mu_0}(\hat{\boldsymbol{y}}\times\mathbf{h}_k). \tag{A.23}$$

With excitation field $\mathbf{h}$ and magnetic response field $\mathbf{m}$ at a given k

$$\mathbf{h}_k = (\mathbf{h}_k\cdot\hat{\boldsymbol{x}})\hat{\boldsymbol{x}} + (\mathbf{h}_k\cdot\hat{\boldsymbol{z}})\hat{\boldsymbol{z}},\ \ \mathbf{m}_k = (\mathbf{m}_k\cdot\hat{\boldsymbol{x}})\hat{\boldsymbol{x}} + (\mathbf{m}_k\cdot\hat{\boldsymbol{z}})\hat{\boldsymbol{z}}, \tag{A.24}$$

LLG equation can be rewritten as

$$\begin{aligned} -(\omega+\omega_0+\omega_M)(\mathbf{m}_k\cdot\hat{\boldsymbol{x}})+\alpha_{\text{eff}}\omega(\mathbf{m}_k\cdot\hat{\boldsymbol{z}}) &= -\frac{\omega_M}{\mu_0}(\mathbf{h}_k\cdot\hat{\boldsymbol{x}}) \\ -(\omega+\omega_0)(\mathbf{m}_k\cdot\hat{\boldsymbol{z}})+\alpha_{\text{eff}}\omega(\mathbf{m}_k\cdot\hat{\boldsymbol{x}}) &= -\frac{\omega_M}{\mu_0}(\mathbf{h}_k\cdot\hat{\boldsymbol{z}}). \end{aligned} \tag{A.25}$$

Rewritten in the form of matrix gives

$$-\frac{\omega_M}{\mu_0}\begin{pmatrix}\mathbf{h}_k\cdot\hat{\boldsymbol{x}}\\ \mathbf{h}_k\cdot\hat{\boldsymbol{z}}\end{pmatrix}=\begin{pmatrix}-(\omega+\omega_0+\omega_M) & -\alpha_{\text{eff}}\omega\\ \alpha_{\text{eff}}\omega & -(\omega+\omega_0)\end{pmatrix}\begin{pmatrix}\mathbf{m}_k\cdot\hat{\boldsymbol{x}}\\ \mathbf{m}_k\cdot\hat{\boldsymbol{z}}\end{pmatrix}. \tag{A.26}$$

The matrix form can be expressed as a constitutive relation

$$\mathbf{h}_k=\mu_0\boldsymbol{\chi}^{-1}\cdot\mathbf{m}_k, \tag{A.27}$$

with inverse susceptibility tensor given by

$$\boldsymbol{\chi}^{-1}=\begin{pmatrix}-(\omega+\omega_0+\omega_M) & -\alpha_{\text{eff}}\omega\\ \alpha_{\text{eff}}\omega & -(\omega+\omega_0)\end{pmatrix}. \tag{A.28}$$

Magnetic susceptibility χ obtained from the susceptibility tensor is

$$\chi=\frac{\omega_M}{\omega+\omega_0}. \tag{A.29}$$

Temperature derivative of the magnetic susceptibility expressed as

$$\frac{d\chi}{dT}=\frac{\omega_M}{\omega+\omega_0}\left|\frac{1}{M_s}\frac{dM_s}{dT}\right|, \tag{A.30}$$

thermal wave vector A.22 can be rewritten as

$$\mathbf{k}_T=-\left(\frac{\omega+\omega_0}{\omega_M}\right)\left|\frac{1}{M_s}\frac{dM_s}{dT}\right|\nabla T. \tag{A.31}$$

Hence, thermal magnon damping torque A.21 can be expressed as a function of temperature gradient as

$$\alpha_{\text{tm}}=-\left(\frac{\omega+\omega_0}{\omega}\right)\left|\frac{1}{M_s}\frac{dM_s}{dT}\right|\frac{1}{k}\nabla T. \tag{A.32}$$

Given that resonance linewidth Δf in relation to effective damping parameter α_{eff} is expressed as

$$\Delta f=\Delta f_0+\frac{2}{\sqrt{3}}\alpha_{\text{eff}}\left|\frac{\omega}{2\pi}\right|, \tag{A.33}$$

and taking relations A.20 and A.32, the change in resonance linewidth (at resonance condition, i.e. $\omega=\omega_K$) under temperature gradient is given by

$$\Delta f=\Delta f_0+\frac{2}{\sqrt{3}}\alpha\left|\frac{\omega_K}{2\pi}\right|-\frac{2}{\sqrt{3}}\left|\frac{\omega_K+\omega_0}{2\pi}\right|\left|\frac{1}{M_s}\frac{dM_s}{dT}\right|\frac{1}{k}\nabla T, \tag{A.34}$$

where Δf_0 is inhomogeneous linewidth, $\omega_K=\pm\sqrt{\omega_0(\omega_0+\omega_M)}$ is Kittel resonance frequency and α is intrinsic damping parameter of material.

Appendix B

Estimation of the Thermal Magnon Torque Damping Parameter

As derived in Appendix A, spin wave resonance linewidth as a function of temperature gradient is expressed as

$$\Delta f = \Delta f_0 + \frac{2}{\sqrt{3}}\alpha \left|\frac{\omega_K}{2\pi}\right| - \frac{2}{\sqrt{3}} \left|\frac{\omega_K + \omega_0}{2\pi}\right| \left|\frac{1}{M_s}\frac{dM_s}{dT}\right| \frac{1}{k}\nabla T. \tag{B.1}$$

This equation can be seen as a linear equation relating Δf and ∇T

$$\Delta f = a + b\nabla T, \tag{B.2}$$

with

$$a = \Delta f_0 + \frac{2}{\sqrt{3}}\alpha \left|\frac{\omega}{2\pi}\right| \tag{B.3}$$

and

$$b = -\frac{2}{\sqrt{3}} \left|\frac{\omega + \omega_0}{2\pi}\right| \left|\frac{1}{M_s}\frac{dM_s}{dT}\right| \frac{1}{k}. \tag{B.4}$$

From experimental data of spin wave resonance linewidth Δf as a function of temperature difference ΔT one can get the value of b (Fig. 5.13b and 5.14b) as a slope of the data.

Recalling thermal magnon damping torque as a function of temperature gradient

$$\alpha_{\mathrm{tm}} = -\left(\frac{\omega + \omega_0}{\omega}\right) \left|\frac{1}{M_s}\frac{dM_s}{dT}\right| \frac{1}{k}\nabla T, \tag{B.5}$$

rewritten in the form of

$$\alpha_{\mathrm{tm}} = \frac{c}{\omega}\nabla T \tag{B.6}$$

with

$$c = -(\omega + \omega_0) \left|\frac{1}{M_s}\frac{dM_s}{dT}\right| \frac{1}{k} = b\sqrt{3}\pi, \tag{B.7}$$

thermal magnon damping parameter can be estimated by calculating c and substitute it to Eqn. B.6, with ω is resonance frequency of the spin wave.

Appendix C

Simulation of Temperature Gradient in YIG

Temperature gradient applied to the system (Diamond/YIG/GGG/YIG) is simulated by finite element method using Autodesk Fusion 360. In Fig. C.1a temperature difference of 10 K over 1 mm distance is applied to the system with temperature at A side equal to 310 K and at B side equal to 300 K. Thermal conductivity of each material in the system known to be 7.14 W/mK for YIG, 7.05 W/mK for GGG, and 2200 W/mK for diamond. The simulation is performed by considering convection heat transfer by ambient air with heat transfer coefficient on YIG top surface estimated to be 9.318 W/m^2K, on diamond top surface to 19.900 W/m^2K, and on diamond vertical surface to be 25.108 W/m^2K.

From the simulation it is calculated that horizontal temperature gradient is created along YIG/GGG/YIG sample except at the region just below diamond. At the depth of 10 μm from YIG top surface temperature gradient is calculated to be about 5 K/mm; about 50 % from intended temperature gradient applied to the system. Due to the high thermal conductivity of diamond, effective temperature gradient that contribute to the generation of thermal magnon and inducing magnetization torque is half of the total effective temperature gradient generated in the system.

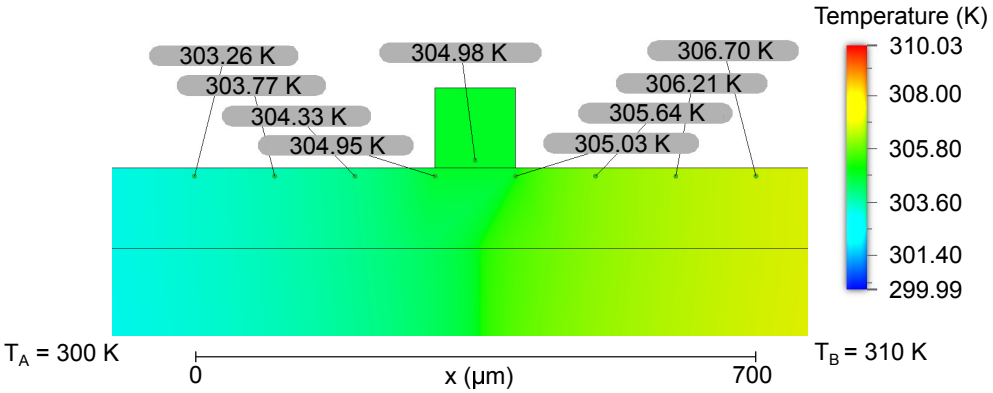

(a)

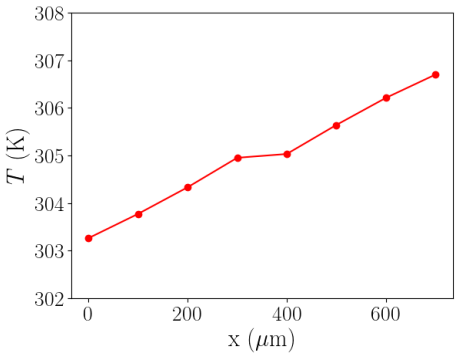

(b)

Figure C.1: (a) Simulated temperature profile of the system under temperature difference $\Delta T = 10$ K. (b) Line cut of temperature profile (dashed line at (a)) at the depth of 10 μm from YIG surface.

Appendix D

Temperature at the Center of YIG

Temperature at the center of long dimension of YIG can be monitored through diamond NV center. With high thermal conductivity of diamond (about 2200 W /m $\cdot$ K), temperature at the middle of YIG's long dimension can be well represented by the temperature of diamond. Diamond NV center can be used as temperature sensor by monitoring the shift of its zero field splitting (ZFS) (splitting between $m_s = 0$ and $m_s = \pm 1$). The shift of ZFS in diamond with ensemble of NVs is known to be at a rate of -74 kHz/K [18]. Observation of the shift of ZFS under the application of temperature gradient in YIG resulted in a relatively unchanged temperature at the center of YIG's long dimension (Fig. D.1a and b). The highest temperature change is observed at temperature difference of -10 K, with temperature change of about 1.7 K from 0 K temperature difference (Fig. D.1b).

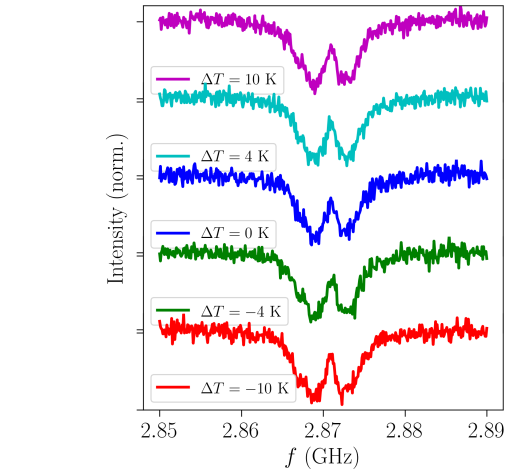

(a)

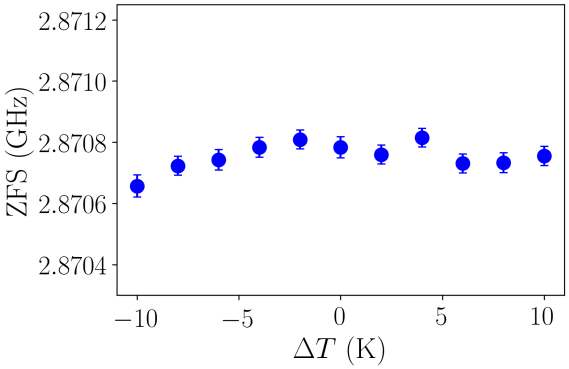

(b)

Figure D.1: (a) ODMR at zero external magnetic field under various temperature difference applied to YIG. The Splitting in the ODMR spectra is due to the strain in diamond crystal(b) Zero field splitting as a function of temperature difference. The value of ZFS is obtained from averaging the two resonance dips in ODMR spectrum in (a).

Appendix E

NV Spin Relaxometry (T_1) Measurement

As recently demonstrated by Du *et al.* [63], chemical potential of magnon can be probed through NV spin relaxation measurement. We performed relaxation measurement in order to probe magnon chemical potential change under the influence of temperature gradient. We obtained relaxation rate $\Gamma_1 = 1/T_1$, which according to Du *et al.* [63] is related to chemical potential of magnon μ_m

$$\Gamma_1(\mu) = n(\omega, \mu) \int D(\omega, \mathbf{k}) f(\mathbf{k}, d) d\mathbf{k} + \Gamma_1^0, \tag{E.1}$$

where $n(\omega, \mu)$ is magnon occupancy defined by Rayleigh-Jeans distribution $k_B T/(\hbar\omega - \mu)$, $D(\omega, \mathbf{k})$ is magnon spectral density of magnon with wavenumber $\mathbf{k}$ and frequency ω, $f(\mathbf{k}, d) \simeq k e^{-2dk}(1 - e^{-2t_{\mathrm{YIG}}k})$ is a function defining magnetic noise generated by magnon with wave number $\mathbf{k}$ that can be sensed by NV spin at a distance d from the surface of YIG with thickness t_{YIG}, and Γ_1^0 is the intrinsic relaxation rate of the NV spin.

We observed a trend that correlate with our measurement of Rabi oscillation under temperature gradient, a modulation of relaxation rate of the NV spins under the application of temperature gradient in YIG. Though the confidence level of the measurement is low considering the variation of the data that are within the error bar, the trend seems to support our detection of thermal magnon. On $H = 75$ Oe geometry we observe an increase in relaxation rate Γ_1, that may indicate the increase of magnon chemical potential μ_m, as we increase temperature difference positively and conversely we observe a decrease in relaxation rate as temperature difference move to negative regime of temperature difference (Fig. E.1). Accordingly if we reverse the direction of bias field to $H = -75$ Oe, reverse effect is observed (Fig. E.2).

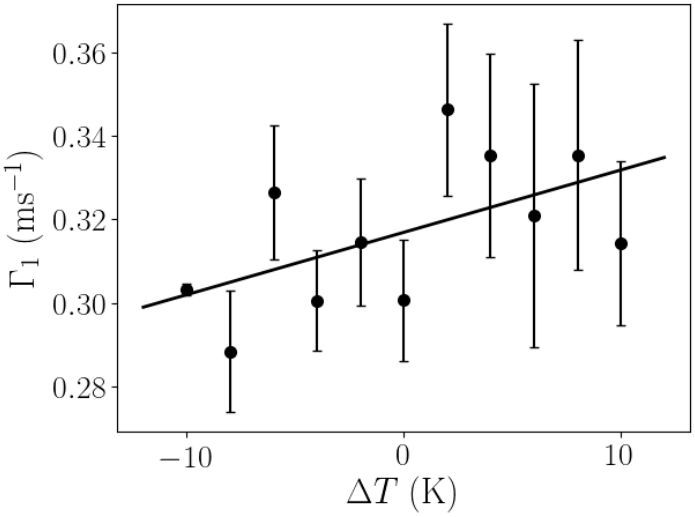

(a)

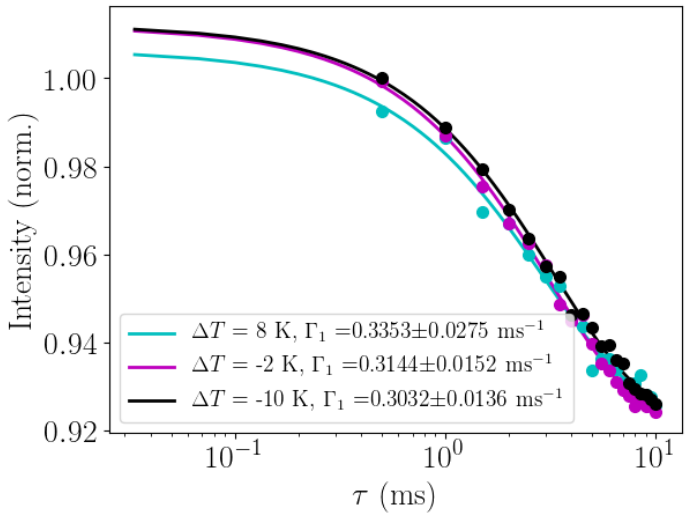

(b)

Figure E.1: (a) NV spin relaxation rate Γ_1 under varied temperature difference on $+\mathbf{H}$ geometry. (b) NV spin relaxation rate on $H = 75$ Oe at $\Delta T = 8$ K, -2 K, and -10.

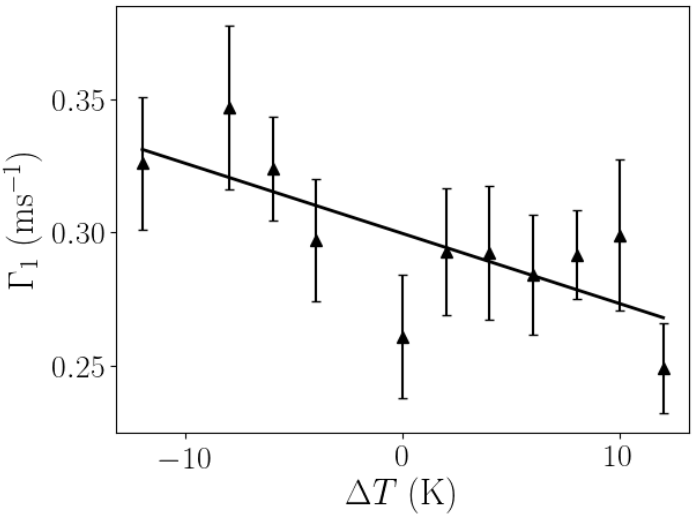

(a)

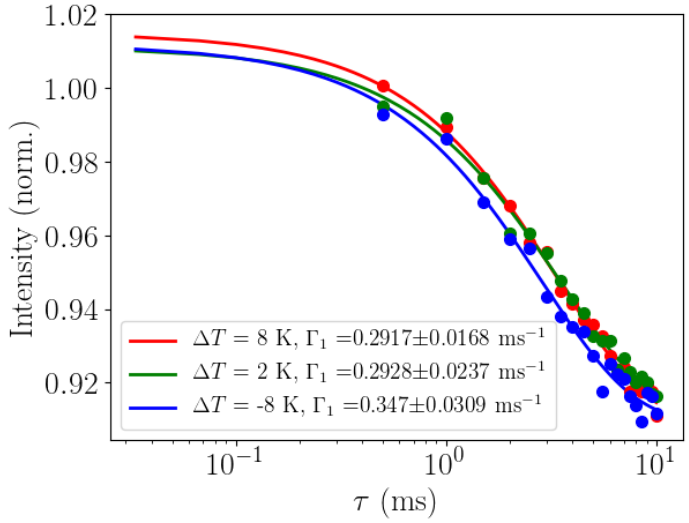

(b)

Figure E.2: (a) NV spin relaxation rate Γ_1 under varied temperature difference on $-\mathbf{H}$ geometry. (b) NV spin relaxation rate on $H = -75$ Oe at $\Delta T = 8$ K, 2 K, and -8 K.

Appendix F

Imaging of Stray Magnetic Field from Magnetic Particle with Ensemble of Spins in Diamond

F.1 Introduction

The advancement of magnetic-based technology such as magnetic recording devices goes hand in hand with the advancement of magnetometry techniques. With the growing advanced techniques in nanofabrication, understanding of magnetic dynamics in micro to nanoscale magnetic structures demands for magnetometry techniques which capable of measuring magnetic phenomena with high spatial resolution and sensitivity. Various techniques in magnetic imaging have been developed and proven to achieve high performance with some trade-off in either spatial resolution or sensitivity. Moreover, some magnetometry techniques have several issues regarding laborious fabrication and limitation of working environment. Among them are magnetic force microscopy (MFM) [81], magnetic resonance force microscopy (MRFM) [84], scanning superconducting quantum interference device (SQUID) [87], and scanning Hall probe microscopy [85].

In the recent years, color center in diamond, known as nitrogen-vacancy (NV) center, has become a major concern among scientific communities due to its potential as a sensor for multiple physical properties, i.e. magnetic field [15, 83, 86], electric charge [21], temperature [82], and pressure [20]. Negatively charged diamond with nitrogen-vacancy center (NV center) consists of substitutional nitrogen atoms and neighboring atomic defects which results in two active electrons forming spin triplet in its ground state energy levels. The spin triplet formed spin sublevels of $m_s = 0$ and $ms = \pm 1$ which splitted by 2.87 GHz due to spin-spin interaction [28] (Fig. 1(a)). These spin sublevels fluoresce with different intensity when optically excited with 532 nm laser.

With the aid of microwave field that resonate with the spin sublevels frequency, these spin states can be manipulated to flip from ms = 0 to $m_s = \pm 1$ state, resulting fluorescence quenching in the observed optically detected magnetic resonance (ODMR) spectrum (Fig. F.1 (c)). The drop in fluorescence in the form of Lorentzian dips is originated from the distinct nature of the spin

sublevels when optically excited, $m_s = 0$ has a higher rate of fluorescence due to spin conserving nature whereas $m_s = \pm 1$ has lower rate of fluorescence due to the rapid non-radiative transition through metastable singlet level [80].

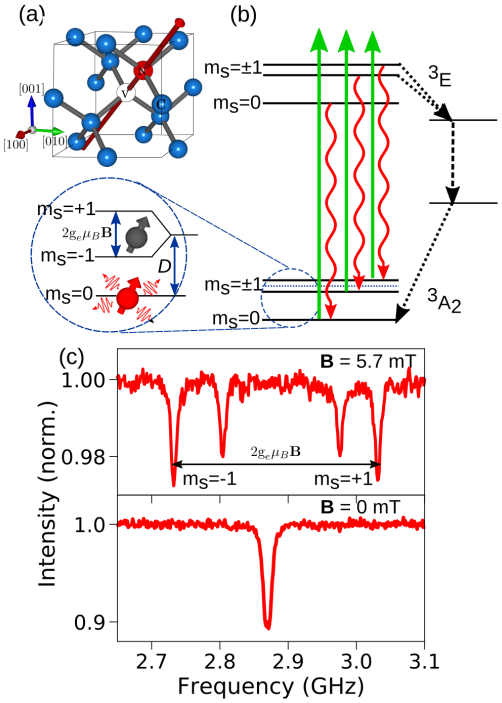

Figure F.1: (a) Diamond with NV center composed of carbon atoms (blue balls) with nitrogen atoms (red balls) impurity and neighboring carbon atom vacancy sites. (b) Electronic structure of diamond with NV center triplet ground state with zero field splitting of 2.87 GHz between $m_s = 0$ and $m_s = \pm 1$. Laser (532 nm) pumping from ground state ms = 0 to excited state resulted in fluorescence with 637 nm of wavelength (wiggly red lines) which drop with population lift to $m_s = \pm 1$. (c) Optically detected magnetic resonance spectra under zero field and applied external magnetic field of 5.7 mT aligned to one of the NV axis (red arrow in (a)).

Thanks to the Zeeman effect, the lifting of $m_s = \pm 1$ degeneracy under magnetic field influence can be harnessed to evaluate magnetic field and served as the basis for diamond NV center magnetometry. The lifting of the spin sublevels is observed as a resonance frequency shift in ODMR spectrum, which corresponds to a specific vector of magnetic field. Variation in magnetic field is translated into a variation of ODMR spectrum as can be seen in Fig. F.1(c) where single resonance dip at 2.87 GHz splited into 4 resonance dip when diamond subjected to 5.7 mT of magnetic field.

Several experiments on the use of diamond NV center as magnetic sensor for vector magnetometry have been reported [15, 86]. Nevertheless, vector magnetometry in the reported works were performed on magnetic structure with stray magnetic field which can easily be predicted prior to measurement, i.e. current-carrying conductor [86] and thin film ferromagnet [15] deposited on a diamond chip. The two previous works also require a bias field to resolve symmetry issue in ensemble NV centers. In this work, we report a technique in

recovering stray magnetic field around a spherically shaped magnetic structure in which magnetization direction is obscured prior to measurement. It is also demonstrated that vector magnetometry with diamond NV centers can be done without bias magnetic field.

F.2 Experiment

(001) oriented type Ib diamond (3 mm × 3 mm × 0.5 mm), grown by high pressure high temperature (HPHT) method, is employed in this work as a magnetic sensor. $^{15}N^{+}$ ions were implanted into the diamond at 35 keV energy with density of implantation 1.2×10^{11} ions/cm^2. The diamond chip was annealed for about 2 hours at 900 °C to create assemblage of NV centers which occupy at the depth of about 30 – 40 nm from surface.

The employment of diamond with ensemble of NV spins has some advantages over diamond with single NV spin considering the large number of NV spins that occupy a single laser spot. Collective response from NV spins will amplify the number of collected photons, which means an enhancement in signal-to-noise ratio [18]. Making it possible to perform shorter integration time to tens of milliseconds and increase the acquisition speed for single ODMR spectrum with clear contrast.

We employ a confocal microscopy system (Fig. F.2(a)) for optically measure magnetic field around a magnetic structure. The measurement process is initiated by continuously illuminate diamond with 532 nm wavelength (green) laser and collecting the resulting fluorescence through an avalanche photodiode (APD). While keeping the laser illumination, microwave is sweep with frequency range about the resonance frequency of the NV spins. The collected fluorescence is represented as an optically detected resonance spectrum that appeared as contrasting Lorentzian dips at the resonance frequency of NV spins.

A magnetic particle of NdFeB with diameter of about 20 μm is placed on the diamond chip. The green laser (0.1 mW) is focused by an objective lens of 50 × 0.6 NA, resulting laser spot area of about 1 μm^2. By using X-Y piezo scanning stage, the laser is scanned over an area around the magnetic particle. The NV spins which densely occupied the volume of laser spot and directing in four possible axes; [111], $[\bar{1}\bar{1}1]$, $[\bar{1}1\bar{1}]$, and $[1\bar{1}\bar{1}]$ (Fig. F.3(b)) were interrogated to extract information about the local vector magnetic field. Three orthogonal crystal axes ([100], [010], and [001]) are coincide with the laboratory axes x, y, and z.

At each point during spin interrogation process, microwave field is radiated through a gold wire antenna which drive the spin state from $m_s = 0$ to $m_s = \pm 1$. Low-power (63 mW) microwave is swept with frequency ranging about the resonance of the NV spins (2.8 – 2.94 GHz). Low-power microwave radiation is applied considering that higher microwave power have a tendency to broaden the linewidth of ODMR spectrum and diminish measurement sensitivity [30]. Linewidth broadening in ODMR spectrum will results in ambiguous ODMR dips and may disrupt the information about magnetic field vector extracted from measurement.

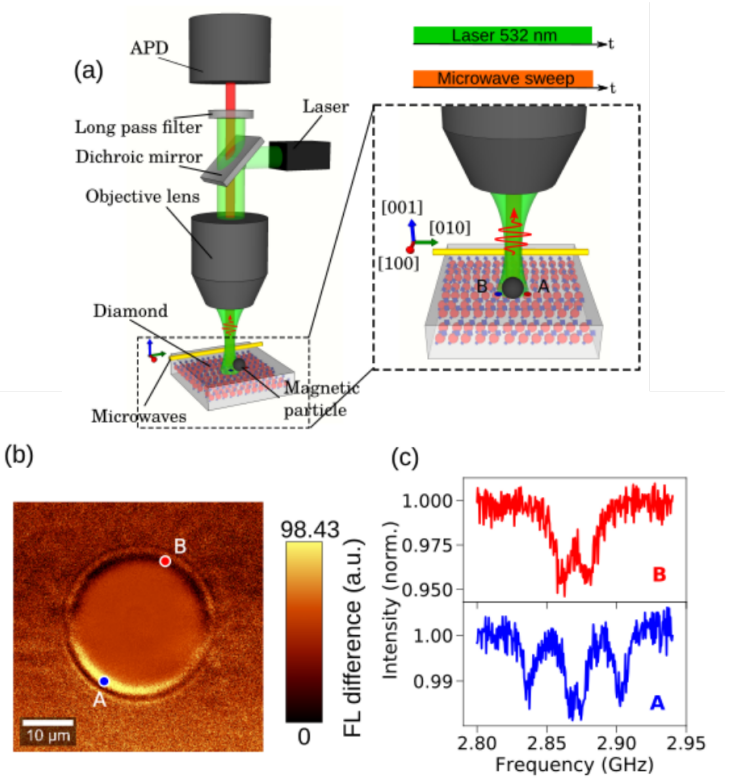

Figure F.2: (a) Schematic of confocal microscopy system used in stray magnetic field vector imaging. Magnetic particle is placed on (001) diamond chip and laser is scanned over an area surrounding the particle. Microwaves are swept at each scanning point to obtain ODMR spectrum which corresponds to a vector of stray magnetic field. (b) Subtracted fluorescence image of diamond scanned over an area around a magnetic particle (circle). (c) ODMR spectra at two different spot, blue and red in (b), on diamond with distinct spectrum due to the variation in vector field.

F.3 Results and Discussion

The recovery of vector stray magnetic field around the magnetic micro particle was done by analyzing ODMR spectra obtained from laser interrogations. The ODMR spectra are fitted by using a function that composed of a sum of eight Lorentzian functions, with each Lorentzian centered at the resonance frequency of $m_s = \pm 1$ NV spins. Each of the Lorentzian dip represents the resonance of the NV spins directing to four possible quantization axes as illustrated in Fig. F.3(b). The center frequency of the Lorentzian dips is determined by obtaining Eigen value of the ground-state spin Hamiltonian of diamond NV center

$$H = hD_{gs}S_z^2 + g\mu_B \mathbf{B} \cdot \mathbf{S}, \tag{F.1}$$

where h is Planck constant, D_{gs} is the gound state zero field splitting, $\mathbf{S}$ is spin projection, g is Landé g-factor, μ_B is Bohr magneton, and $\mathbf{B}$ is magnetic field vector.

Each of the ODMR spectra is analyzed by performing least square fit using

Levenberg–Marquardt algorithm (LMA) to extract information about vector stray magnetic field. The result of the LMA fitting is an information about direction (in polar coordinate system) and magnitude of magnetic flux associated to each point of interrogation during laser scanning process. The fitting enables us to discriminate each four contributing electron spin resonance from NV spins directing to four possible quantization axes (Fig. F.3(a)). These eight resonance dips, illustrated in Fig. F.3(a), corresponds to the projection of vector stray field to the four NV quantization axes.

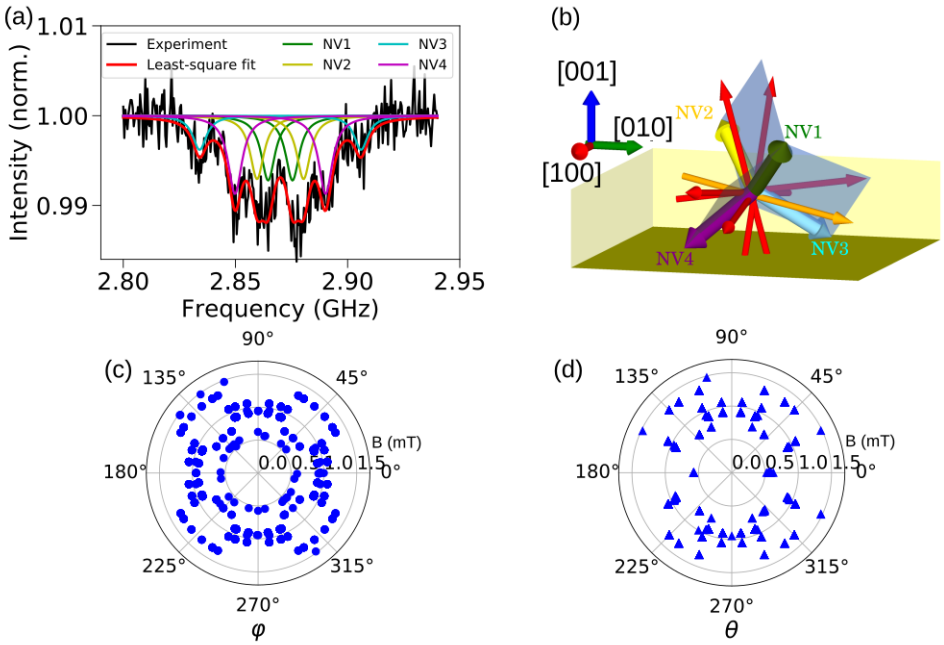

Figure F.3: (a) Least-square fit (red line) of ODMR spectrum at one scanning spot. Projection of magnetic field vector along the four possible NV axes can be clearly separated in the spectrum. (b) Due to C_{3v} symmetry, one magnetic field vector (orange arrow) will have more than one identical vector (red arrows) with indistinguishable ODMR spectrum. Polar plot of estimated magnetic field magnitude as a function of estimated azimuthal angle φ (c) and polar angle θ (d). Azimuthal angle exhibit four-fold rotational symmetry, while polar angle exhibit two-fold rotational symmetry.

In extracting information from ODMR spectrum, one needs to be aware of the C_{3v} symmetry in diamond tetrahedral structure that may cause misestimating of the corresponding vector stray magnetic field. Due to the C_{3v} symmetry, one vector stray magnetic field projected into an NV quantization axis may results in five identical vectors with indistinguishable ODMR spectrum (Fig. F.3(b)). The consequences of this can be seen in the polar plot representing the result of estimated vector magnetic field as calculated by the fitting algorithm for any possible azimuthal and polar angle. It can be seen from the polar plot that azimuthal angle θ exhibit four-fold rotational symmetry while the polar angle φ exhibit two-fold symmetry. Hence, it is not possible to determine the actual vector field without prior information about magnetization direction of the magnetic structure under investigation.

The issue can be solved by inspecting ODMR spectra at the edge of magnetic structure to infer the magnetization direction of the magnetic structure. ODMR spectrum with high resonant transition frequency at one side of magnetic structure and low resonant transition at the opposite side indicates that magnetization of the magnetic micro particle is pointing from the side with low resonant transition frequency to the side with high resonant transition frequency (fig. F.2(b)). This is confirmed by carrying fluorescence imaging to the diamond. By subtracting fluorescence images with and without applying microwave field of frequency 2.837GHz, fluorescence contrast was formed at one side of the magnetic structure but not found in the opposite side (Fig. F.2(c).

With the information of the magnetic micro particle magnetization direction, real vector stray magnetic field can be easily inferred from the results of the fitting algorithm calculation. The results of the recovery of vector stray magnetic field recovery is displayed on Fig. F.4 (b), where each arrow represents the vector field that inferred from the corresponding ODMR spectrum at local position. The tilt angle of magnetization to x-y plane can be estimated from the calculated vector field at the position where ODMR spectrum showed highest resonant transition frequency. It is estimated that the magnetization of the magnetic micro particle is tilted down of about 20° from the x-y plane (Fig. F.4(a)).

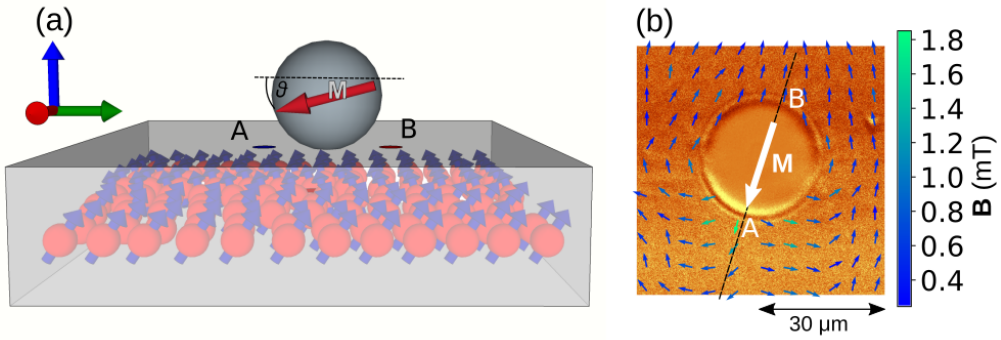

Figure F.4: (a) Estimated magnetization vector of the magnetic micro particle showing a tilted angle of about 20o from x-y plane. (b) Stray magnetic field vector recovery as seen as x-y plane, color variation of arrow represent the magnitude of magnetic field. The overlaid fluorescence image is a result of subtraction between fluorescence image with and without applied microwave of 2.837 GHz.

The sensitivity of the vector field magnetic field measurement can be estimated from ODMR spectrum at one local position by using photon shot-noise-limited dc magnetic field sensitivity η given by the relation [30, 88];

$$\eta = 0.77 \frac{h}{g\mu_B} \frac{\Delta f}{C\sqrt{I}} \tag{F.2}$$

with Δf is the linewidth of Lorentzian dip, C is the contrast of ODMR spectrum dip, and I is fluorescence intensity. Magnetic field sensitivity of about

2.5 μT/$\sqrt{\text{Hz}}$ was achieved from the magnetic field measurement. The spatial resolution that can be achieved from the experiment is $\sim$ 1 μm.

F.4 Conclusion

In conclusion, we have demonstrated a recovery of stray magnetic field vectors from three-dimensional magnetic structure using optically detected magnetic resonance of NV spins in diamond. The experiment has successfully demonstrated the ability of diamond-based magnetic sensor to detect stray magnetic field of magnetic structure with three-dimensional magnetization direction. The use of external magnetic field bias to determine directionality of magnetic field can be eliminated by inferring direction from ODMR spectrum with high resonant frequency shift at the edges of magnetic structure under investigation. DC magnetic field sensitivity of 2.5 μT/$\sqrt{\text{Hz}}$ can be achieved by this measurement with spatial resolution of $\sim$ 1 μm.

Bibliography

[1] G. E. Moore, IEDM Tech. Digest 11–13 (1975).

[2] M. M. Waldrop, Nature 530, 144 (2016).

[3] I. Žutić, J. Fabian, and S. Das Sarma, Rev. Mod. Phys. 76, 323 (2004).

[4] G. E. W. Bauer, E. Saitoh, and B. J. van Wees, Nat. Mater. 11, 391 (2012).

[5] A. V. Chumak, V. I. Vasyuchka, A. A. Serga, and B. Hillebrands, Nat. Phys. 11, 453 (2015).

[6] A. V. Chumak, A. A. Serga, and B. Hillebrands, Nat. Commun. 5, 4700 (2014).

[7] U. Ritzmann, D. Hinzke, and U. Nowak, Phys. Rev. B 89, 024409 (2014).

[9] H. Yu, S. Granville, D. P. Yu, and J.-Ph. Ansermet, Phys. Rev. Lett. 104, 146601 (2010).

[10] J. C. Slonczewski, J. Magn. Magn. Mater. 159, L1 (1996).

[11] L. Berger, Phys. Rev. B 54, 9353 (1996).

[12] J. C. Slonczewski, Phys. Rev. B 82, 054403 (2010).

[13] C. L. Degen, F. Reinhard, P. Capellaro, Rev. Mod. Phys. 89, 035002 (2017).

[14] F. Casola, T. van der Sar, and A. Yacoby, Nat. Rev. Mater. 3, 17088 (2018).

[15] B. J. Maertz, A. P. Wijnheijmer, G. D. Fuchs, M. E. Nowakowski, and D. D. Awschalom, Appl. Phys. Lett. 96, 092504 (2010).

[16] J. R. Maze, P. L. Stanwix, J. S. Hodges, S. Hong, J. M. Taylor, P. Cappellaro, L. Jiang, M. V. Gurudev Dutt, E. Togan, A. S. Zibrov, A. Yacoby, R. L. Walsworth, and M. D. Lukin, Nature 455, 644 (2008).

[17] M. Pelliccione, B. A. Myers, L. M. A. Pascal, A. Das, and A. C. Bleszynski Jayich, Phys. Rev. Appl. 2, 054014 (2014).

[18] V. M. Acosta, E. Bauch, M. P. Ledbetter, A. Waxman, L.-S. Bouchard, and D. Budker, Phys. Rev. Lett. 104, 070801 (2010).

[19] D. M. Toyli, C. F. de las Casas, D. J. Christle, V. V. Dobrovitski, and D. D. Awschalom, Proc. Natl. Acad. Sci. 110, 8417 (2013).

[20] M. W. Doherty, V. V. Struzhkin, D. A. Simpson, L. P. McGuinness, Y. Meng, A. Stacey, T. J. Karle, R. J. Hemley, N. B. Manson, L. C. L. Hollenberg, and S. Prawer, Phys. Rev. Lett. 112, 047601 (2014).

[21] F. Dolde, M. W. Doherty, J. Michl, I. Jakobi, B. Naydenov, S. Pezzagna, J. Meijer, P. Neumann, F. Jelezko, N. B. Manson, and J. Wrachtrup, Phys. Rev. Lett. 112, 097603 (2014).

[22] J. Harrison, M. J. Sellars, and N. B. Manson, J. Lumin. 107, 245 (2004).

[23] A. Gruber, A. Dräbenstedt, C. Tietz, L. Fleury, J. Wrachtrup, C. von Borczyskowski, Science 276, 2012 (1997).

[24] R. Schirhagl, K. Chang, M. Loretz, and C. L. Degen, Annu. Rev. Phys. Chem., 65, 83 (2014).

[25] E. Abe and K. Sasaki, J. Appl. Phys. 123, 161101 (2018).

[26] L. Rondin , J-P. Tetienne, T. Hingant, J-F. Roch, P. Maletinsky and V. Jacques, Rep. Prog. Phys., 77, 056503 (2014).

[27] G. Balasubramanian, P. Neumann, D. Twitchen, M. Markham, R. Kolesov, N. Mizuochi, J. Isoya, J. Achard, J. Beck, J. Tissler, V. Jacques, P. Hemmer, F. Jelezko and J. Wrachtrup, Nat. Mater., 8, 383 (2009).

[28] J. H. N. Loubser and J. A. van Wyk, Rep. Prog. Phys., 41, 1201 (1978).

[29] L. Robledo, H. Bernien, T. van der Sar and R. Hanson, New J. Phys. 13, 025013 (2011).

[30] A. Dréau, M. Lesik, L. Rondin, P. Spinicelli, O. Arcizet, J.-F. Roch, and V. Jacques, Phys. Rev. B 84, 195204 (2011).

[31] N. B. Manson, J. P. Harrison, and M. J. Sellars, Phys. Rev. B 74, 104303 (2006).

[32] P. Neumann, *Towards a room temperature solid state quantum processor — The nitrogen-vacancy center in diamond*, PhD Thesis, University of Stuttgart (2012)

[33] L. M. Pham, *Magnetic Field Sensing with Nitrogen-Vacancy Color Centers in Diamond*, PhD Thesis, Harvard University (2013).

[34] E. O. Schäfer-Nolte, *Development of a Diamond-based Scanning Probe Spin Sensor Operating at Low Temperature in Ultra High Vacuum*, PhD Thesis, University of Stuttgart (2014).

[35] C. Müller, *Sensing single spins with colour centres in diamond*, PhD Thesis, Ulm University (2016).

[36] R. Landauer, Nature 392, 658 (1998).

[37] N. Bar-Gill, L. M. Pham, C. Belthangady, D. Le Sage, P. Capellaro, J. R. Maze, M. D. Lukin, A. Yacoby, and R. Walsworth, Nat. Commun. 3, 858 (2012).

[38] E. Schäfer-Nolte, L. Schlipf, M. Ternes, F. Reinhard, K. Kern, and J. Wrachtrup, Phys. Rev. Lett. 113, 217204 (2014).

[39] A. Jarmola, V. M. Acosta, K. Jensen, S. Chemerisov, and, D. Budker, Phys. Rev. Lett. 108, 197601 (2012).

[40] J.-P. Tetienne, T. Hingant, L. Rondin, A. Cavaillés, L. Mayer, G. Dantelle, T. Gacoin, J. Wrachtrup, J.-F. Roch, and V. Jacques, Phys. Rev. B 87, 235436 (2013).

[41] T. Rosskopf, A. Dussaux, K. Ohashi, M. Loretz, R. Schirhagl, H. Watanabe, S. Shikata, K. M. Itoh, and C. L. Degen, Phys. Rev. Lett. 112, 147602 (2014).

[42] B. Naydenov, F. Reinhard, A. Lämmle, V. Richter, R. Kalish, U. F. S. D'Haenens-Johansson, M. Newton, F. Jelezko, and J. Wrachtrup, Appl. Phys. Lett. 97, 242511 (2010).

[43] D. D. Stancil and A. Prabhakar, *Spin Waves; Theory and Applications*, New York: Springer (2010).

[44] C. Kittel, *Quantum Theory of Solids*, New York: John Wiley & Sons (1987).

[45] T. Holstein and H. Primakoff, Phys. Rev. 58, 1098 (1940).

[46] L. Landau and L. Lifshitz, Phys. Zeit. Sowjetunion 8, 153 (1935).

[47] T. A. Gilbert, *Equation of motion of magnetization*, Armour Research Foundation Rep. 11 (1955).

[48] A. A. Serga, A. V. Chumak, and B. Hillebrands, J. Phys. D: Appl. Phys. 43, 264002 (2010).

[49] C. Kittel, *Introduction to Solid State Physics*, New York: John Wiley & Sons (2005).

[50] L. J. Cornelissen, K. J. H. Peters, G. E. W. Bauer, R. A. Duine, and B. J. van Wees, Phys. Rev. B 94, 014412 (2016).

[51] L. J. Cornelissen, J. Liu, J. Ben Youssef, and B. J. van Wees, Nat. Phys. 11, 1022 (2015).

[52] B. L. Giles, Z. Yang, J. S. Jamison, and R. C. Myers, Phys. Rev. B 92, 224415 (2015).

[53] B. L. Giles, Z. Yang, J. S. Jamison, J. M. Gomez-Perez, S. Vélez, L. E. Hueso, F. casanova, and R. C. Myers, Phys. Rev. B 96, 180412(R) (2017).

[54] J. Shan, L. J. Cornelissen, J. Liu, J. Ben Youssef, L. Liang, and B. J. van Wees, Phys. Rev. B 96, 184427 (2017).

[55] J. F. Ziegler, *The Stopping and Ranges of Ions in Matter* (www.srim.org).

[56] D. M. Toyli, C. D. Weis, G. D. Fuchs, T. Schenkel, and D. D. Awschalom, Nano. Lett. 10, 3168 (2010).

[57] J. Koike, D. M. Parkin, and T. E. Mitchell, Appl. Phys. Lett. 60, 1450 (1992).

[58] S. Sangtawesin, T. O. Brundage, Z. J. Atkins, and J. R. Petta, Appl. Phys. Lett. 105, 063107 (2014).

[59] S. Pezzagna, B. Naydenov, F. Jelezko, J. Wrachtrup, J. Meijer, New J. Phys. 12, 065017 (2010).

[60] L. I. Childress, *Coherent manipulation of single quantum systems in the solid state*, PhD Thesis, Harvard University (2007).

[61] C. S. Wolfe, V. P. Bhallamudi, H. L. Wang, C. H. Du, S. Manuilov, R. M. Teeling-Smith, A. J. Berger, R. Adur, F. Y. Yang, and P. C. Hammel, Phys. Rev. B 89, 180406(R) (2014).

[62] T. van der Sar, F. Casola, R. Walsworth, and A. Yacoby, Nat. Commun. 6, 7886 (2015).

[63] C. Du, T. van der Sar, T. X. Zhou, P. Upadhyaya, F. Casola, H. Zhang, M. C. Onbasli, C. A. Ross, R. L. Walsworth, Y. Tserkovnyak, and A. Yacoby, Science 357, 195 (2017).

[64] P. Andrich, C. F. delas Casas, X. Liu, H. L. Bretscher, J. R. Berman, F. J. Heremans, P. F. Nealey, and D. D. Awschalom, npj Quantum Inf. 3, 28 (2017).

[65] D. Kikuchi, D. Prananto, K. Hayashi, A. Laraoui, N. Mizuochi, M. Hatano, E. Saitoh, Y. Kim, C. A. Meriles, and T. An, Appl. Phys. Express 10, 103004 (2017).

[66] Y. Kainuma,ダイアモンドNV中心を用いたスピンツロ二クスによるスピン波変調の検出, MSc Thesis, Japan Advanced Institute of Science and Technology (2019).

[67] B. Obry, V. I. Vasyuchka, A. V. Chumak, A. A. Serga, and B. Hillebrands, Appl. Phys. Lett. 101, 192406 (2012).

[68] B. Flebus, P. Upadhyaya, R. A. Duine, and Y. Tserkovnyak, Phys. Rev. B 94, 214428 (2016).

[69] H. Yu, S. D. Brechet, P. Che, F. A. Vetro, M. Collet, S. Tu, Y. G. Zhang, Y. Zhang, T. Stueckler, L. Wang, H. Cui, D. Wang, C. Zhao, P. Bortolotti, A. Anane, J-P. Ansermet, and W. Zhao, Phys. Rev. B 95, 104432 (2017).

[70] Y. Kajiwara, K. Uchida, D. Kikuchi, T. An, Y. Fujikawa, and E. Saitoh, Appl. Phys. Lett. 103, 052404 (2013).

[71] L. Liu, Y. Sun, M. Jantz, and M. Wu, Phys. Rev. Lett. 108, 257202 (2012).

[72] J. Holanda, O. A. Santos, R. L. Rodríguez-Suaréz, A. Azevedo, and S. M. Rezende, Phys. Rev. B 95, 134432 (2017).

[73] M. B. Jungfleisch, T. An, K. Ando, Y. Kajiwara, K. Uchida, V. I. Vasyuchka, A. V. Chumak, A. A. Serga, E. Saitoh, and B. Hillebrands, Appl. Phys. Lett. 102, 062417 (2013).

[74] Y. Guan, W. E. Bailey, E. Vescovo, C. -C. Kao, D. A. Arena, J. Magn. Magn. Mater. 312, 374 (2007).

[75] D. M. Pozar, *Microwave Engineering*, New York: John Wiley and Sons (1998).

[76] N. Thiery, A. Draveny, V.V. Naletov, L. Vila, J. P. Atané, C. Beigné, G. de Loubens, M. Viret, N. Beaulieu, J. Ben Youssef, V. E. Demidov, S. O. Demokritov, A. N. Slavin, V. S. Tiberkevich, A. Anane, P. Bortolotti, V. Cros, and O. Klein, Phys. Rev. B 97, 060409(R) (2018).

[77] J. Liu, F. Feringa, B. Flebus, L. J. Cornelissen, J. C. Leutenantsmeyer, R. A. Duine, and B. J. van Wees, Phys. Rev. B 99, 054420 (2019).

[78] T. An, V. I. Vasyuchka, K. Uchida, A. V. Chumak, K. Yamaguchi, K. Harii, J. Ohe, M. B. Jungfleisch, Y. Kajiwara, H. Adachi, B. Hillebrands, S. Maekawa and E. Saitoh, Nat. Mater. 12, 549 (2013).

[79] S. D. Brechet and J-P. Ansermet, Eur. Phys. Lett. 112, 17006 (2015).

[80] V. M. Acosta, A. Jarmola, E. Bauch, and D. Budker, Phys. Rev. B 82, 201202(R) (2010).

[81] M. R. Freeman and B. C. Choi, Science 294, 1484 (2001).

[82] A. Laraoui, H. Aycock-Rizzo, Y. Gao, X. Lu, E. Ried, and C. A. Meriles, Nat. Commun. 6, 8954 (2015).

[83] P. Maletinsky, S. Hong, M. S. Grinolds, B. Hausmann, M. D. Lukin, E. L. Walshworth, M. Loncar, and A. Yacoby, Nat. Nanotech. 7, 320 (2012).

[84] D. Rugar, R. Budakian, H. J. Mamin and B. W. Chui, Nature 430, 329 (2004).

[85] A. Sandhu, H. Masuda, A. Oral, and S. J. Bending, Jpn. J. Appl. Phys. 40, 4321 (2001).

[86] S. Steinert, F. Dolde, P. Neumann, A. Aird, B. Naydenov, G. Balasubramanian, F. Jelezko, and J. Wrachtrup J, Rev. Sci. Instrum. 81, 043705 (2010).

[87] M. Tachiki, T. Hayashi, D. He, and H. Itozaki, IEEE Trans. Appl. Supercond. 19, 874 (2009).

[88] J. M. Taylor, P. Cappelaro, L. Childress, L. Jiang, D. Budker, P. R. Hemmer, A. Yacoby, R. Walsworth, and M. D. Lukin, Nat. Phys., 4, 810 (2008).

Publication List

Journals

1. **D. Prananto**, Y. Kainuma, K. Hayashi, and T. An, *Detection of Thermal Magnon via Nitrogen-Vacancy Centers in Diamond*, In preparation.

2. **D. Prananto**, D. Kikuchi, K. Hayashi, and T. An, *Imaging of stray magnetic field vectors from magnetic particle with an ensemble of nitrogen-vacancy centers in diamond*, to be published in Jpn. J. Appl. Phys. (2019).

3. D. Kikuchi, **D. Prananto**, K. Hayashi, A. Laraoui, N. Mizuochi, M. Hatano, E. Saitoh, Y. Kim, C. A. Meriles, and T. An, *Long-distance excitation of nitrogen-vacancy centers in diamond via surface spin waves*, Appl. Phys. Express **10**, 103004 (2017).

Presentations at conference

Oral presentation

1. D. Kikuchi, **D. Prananto**, K. Hayashi, A. Laraoui, N. Mizuochi, M. Hatano, E. Saitoh, Y. Kim, C. A. Meriles, and T. An. *Long-distance excitation of nitrogen-vacancy centers in diamond via surface spin waves.* Presented at The American Physical Society March Meeting 2018. Los Angeles, USA. March 5-9, 2018.

2. **D. Prananto**, D. Kikuchi, N. Mizuochi, and T. An. *Stray Magnetic Field Detection and Imaging from Magnetic Particle with an Ensemble of Nitrogen Vacancy Center in Diamond.* Presented at The 77^{th} Japan Society of Applied Physics Autumn Meeting 2016. Niigata, Japan. September 13-16, 2016.

Poster presentations

1. **D. Prananto**, K. Hayashi,and T. An, *Vector Magnetic Field Imaging of a Magnetic Particle with NV centers in Diamond.* Presented at 14th International Conference on Atomically Controlled Surfaces, Interfaces and Nanostructures (ACSIN-14), Sendai, Japan. October 21 - 25, 2018

2. **D. Prananto**, D. Kikuchi, K. Hayashi, and T. An, *Three-Dimensional Imaging of Stray Magnetic Field with Nitrogen-Vacancy Centers in Diamond Authors.* Presented at The American Physical Society March Meeting 2018. Los Angeles, USA. March 5-9, 2018.

3. **D. Prananto**, D. Kikuchi, K. Hayashi, and T. An, *Vector magnetic field imaging with nitrogen-vacancy centers in diamond*, Presented at JAIST Japan-India Symposium on Materials Science 2017. Nomi, Japan, March 6 -7, 2017.

4. **D. Prananto**, D. Kikuchi, K. Hayashi, and T. An, *Magnetic Field Imaging of Magnetic Particle with Nitrogen-Vacancy Centers in Diamond.* Presented at International School on Spintronics and Spin-Orbitronics. Fukuoka, Japan. December 16-17, 2016.

5. **D. Prananto**, D. Kikuchi, K.Hayashi, and T. An, *Vector Magnetic Field Imaging with Ensemble of Spins in Diamond.* Presented at International Symposium on Metal and Insulator Spintronics. Yokohama, Japan. November 26, 2016.

6. **D. Prananto**, D. Kikuchi, N. Mizuochi, and T. An, *Stray Magnetic Field Detection and Imaging from Magnetic Particle with an Ensemble of Nitrogen Vacancy Center in Diamond*, Presented at 物性研短期研究会「走査トンネル顕微鏡による物性研究の現状と展望」. Kashiwa, Japan, October 30 -November 1, 2016.